POLITECNICO DI TORINO

Collegio di Ingegneria Meccanica, Aerospaziale, del Veicolo e
della Produzione

Corso di Laurea Magistrale in Ingegneria Aerospaziale

Tesi di Laurea Magistrale

Experimental and Analytical Characterization of Injector Variation in Single Element Rocket Combustion Chambers

Relatore
prof. Dario Giuseppe Pastrone

Correlatore
M. Sc. Simona Silvestri

Candidato
Mattia Garulli

Marzo 2018

Declaration of Authorship

I hereby certify that this Master's thesis has been composed by me and is based on my own work, unless stated otherwise. No other person's work has been used without due acknowledgement in this thesis. All references and verbatim extracts have been quoted, and all sources of information, including graphs and data sets, have been specifically acknowledged.

Place and date: Signature:

I would like to dedicate to my loving Paolo, Liliane and Lalà

Acknowledgments

I would like to thank M.Sc. Simona Silvestri for driving me through a such challenging and amazing world, teaching me how will and self-sacrifice can everything. That’s worth more than anything else. My thanks to Professor Dario G. Pastrone, Professor Oskar J. Haidn and the Lehrstuhl für Flugantriebe of the Technische Universität München for giving me the opportunity to prove myself in a such stimulating field. A thank you to M.Sc. Fernanda Winter and M.Sc. Nikolaos Perakis for the formative threads and training tips. That has been much appreciated. My thanks to Sarath Devanand and Gianluca Vespero, too, for being good fellow travelers.

Finally, my family. *Lalà*. And *Liliane* and *Paolo*. All this because of you and it could not have been, otherwise. We made it, together. Thank you from the bottom of my heart. *Vôtre petit gamin, vôtre Ciccio.*

Ringraziamenti

I miei ringraziamenti a M.Sc. Simona Silvestri per avermi guidato alla scoperta di un mondo tanto incredibile quanto stimolante, per avermi insegnato quanto volontà e abnegazione possono tutto. Questo vale più di ogni altro. Un ringraziamento a Professor Dario G. Pastrone, Professor Oskar J. Haidn e al Dipartimento di Propulsione Aerospaziale presso l'Università Tecnica di Monaco per avermi dato l'opportunità di cimentarmi in un campo tanto affascinante. Un sentito grazie a M.Sc. Fernanda Winter e M.Sc. Nikolaos Perakis per le discussioni formanti e i consigli. Sono stati molto apprezzati. Grazie a Sarath Devanand e Gianluca Vespero per essere stati dei buoni compagni di viaggio.

Infine, la mia famiglia. *Lalà*. E *Liliane* e *Paolo*. Sono fiero di voi. Tutto questo è grazie a voi e non sarebbe potuto essere, altrimenti. L'abbiamo fatto, insieme. Grazie di cuore. *Vôtre petit gamin, vôtre Ciccio.*

Abstract

The influence of oxidizer post recess variation in a single-element gaseous oxygen/gaseous methane fed shear coaxial injector is experimentally investigated. A rectangular inner cross section combustion chamber with optical access is set up and tested at a pressure level of 20 bar and representative rocket engine conditions. Recess lengths of 2.25, 3 and 3.75 times the inner oxidizer post diameter are examined. Wall pressure, temperature and heat loads distributions as well as combustion performance are presented, an overall improvement of the mixing process and combustion effectiveness being detected, compared to the flush-mounted injector configuration. A comparison with a previous recess variation investigation on a round combustion chamber under similar operating conditions is also discussed, allowing an insight of inner architecture effects on combustion process. An imaging analysis of the jet dynamics in the rectangular hardware near-injector region is conducted, finally.

Estratto

L’influenza della variazione della lunghezza di recesso in un iniettore a singolo elemento coassiale tipo shear ossigeno gassoso/metano gassoso è sperimentalmente indagata. Una camera di combustione rettangolare con accesso ottico è allestita e testata per pressioni nominali di 20 bar e tipiche condizioni di funzionamento di endoreattori a propellente liquido. Lunghezze di recesso di 2.25, 3 e 3.75 volte il diametro interno del condotto di iniezione dell’ossidante sono analizzate. Le distribuzioni di pressione, temperatura e flusso di calore a parete, nonché delle prestazioni di combustione sono presentate, essendosi riscontrati un complessivo incremento nell’efficacia di combustione e processo di mixing dei reagenti, se comparati con le caratteristiche in assenza di recesso. Una comparazione con una precedente indagine sulla variazione della lunghezza di recesso su di una camera di combustione a sezione circolare sotto simili condizioni operative è discussa, al fine di analizzare gli effetti dell’architettura interna sul processo di combustione. Infine, un’analisi ottica della dinamica di fiamma all’iniettore per la camera di combustione rettangolare è illustrata.

Table of Contents

List of Figures

List of Tables

List of Symbols and Variables

A	: cross section area	m^2
$\boldsymbol{c}^*$	: characteristic exhaust velocity	m/s
C_d	: discharge coefficient	*[-]*
d	: diameter	$[m]$
G	: relative combustion chamber pressure coefficient gain	*[-]*
J	: fuel-to-oxidizer moment flux ratio	*[-]*
K	: injector pressure drop coefficient	*[-]*
K^{C_d}	: discharge coefficient factor	*[-]*
K_η	: efficiency factor	*[-]*
l	: post length	$[m]$
$\dot{m}$	: mass flow rate	$[kg/s]$
n	: number of test repetitions	*[-]*
O/F	: oxidizer-to-fuel ratio	*[-]*
P	: static pressure	$[bar]$
$\dot{\boldsymbol{q}}$	: heat flux	$[W/m^2]$
S	: sample standard deviation	-
SE	: sample standard error of the mean	-
R	: recess length	$[mm]$
T	: static temperature	$[K]$

t : post wall thickness $[m]$

u : flow stream axial velocity $[m/s]$

VR : fuel-to-oxidizer velocity ratio $[-]$

z : axial coordinate along the combustion chamber $[mm]$

ρ : static density $[kg/m^3]$

η_{c^*} : combustion efficiency $[-]$

Subscripts and Superscripts

C : combustion chamber

$dome$: injector head

end : shut-down testing phase

ER : energy release

$eval$: evaluation time

F : film cooling

HOT : without film cooling

i : internal

M : methane

max : maximum

nom : nominal

O : oxygen

o : external

ref : reference

$start$: start-up testing phase

TC : thrust chamber

$test$: measured

$theo$: theoretical

List of Abbreviations

CEA : Chemical Equilibrium with Applications

CH_4 : liquid methane

GCH_4 : gaseous methane

GH_2 : gaseous hydrogen

GN_2 : gaseous nitrogen

GO_X : gaseous oxygen

H_2 : liquid hydrogen

LO_X : liquid oxygen

LRE : liquid rocket engine

MoRaP : Mobile Rocket Combustion Chamber Test Bench

OH : hydroxyl radical

PDE : partial differential equation

TUM : Technische Universität München

Chapter 1

Introduction

Nowadays liquid propellant rocket engines based on cryogenic propellant combinations, such as liquid oxygen/liquid hydrogen (LO_X/H_2), or storable propellant combinations, such as monomethyl-hydrazine/nitrogen tetroxide (MMH/NTO), represent the principal and most employed means for transfer into orbit and space exploration missions, due to their high performances in term of specific impulse and hypergolic nature, respectively. The perspective of using hydrocarbons as propellant, in particular methane (CH_4), is strongly considered as a solution for the next generation of space transport systems, due to relative low costs, low emissions and high performance.

If compared with other hydrocarbon fuels, methane presents better overall performances from a launch-vehicle system point of view [1], due to its high thermal conductivity, specific heat, low viscosity and higher specific impulse [2]. A easier extraction process from natural gases is also granted, because of its abundancy in many parts of the solar system, so potentially being harvested providing fuel, so reducing landed mass requirement by means of *in situ* propellant production [3]. Methane is reported to grant the advantage over kerosene of depositing less carbon as well as soot deposition on the internal walls of the rocket engine, so easing its potential reuse, even though the use of kerosene potentially leads to a lower booster dry mass, due to its higher density [1]. If one consider the use of propellant in the context of cooling system, methane provides the best cooling features among hydrocarbons, as well as less coking attitude [4]. In addition, methane shows a density six times higher than hydrogen when stored at typical tank conditions in liquid state, thus enhancing higher thrust-to-weight ratio as well as easier handling because of its higher critical temperature.

The design and realization of a liquid rocket engine (LRE) featuring methane/oxygen combination require a deep knowledge of the fundamental physical process underneath propellant/oxidizer injection interaction, combustion dynamics, flame stability and heat release. To this end, a large amount of experimental data, led at typical combustion chamber conditions, is necessary to characterize both injector-injector and injector-wall behaviour as well as to provide benchmarks for the developing of reliable computational methods and test cases for numerical simulations validation. From the late ‘70s, oxygen/methane combination has been explored with a view to being employed in high pressure booster engine applications [5] as well as efforts have been carried out in order to produce a solid experimental background in this respect. Liquid oxygen/gaseous methane propellant combination has been considered for rocket applications over the years and at various times in the US [6], as well as in Russia [7] and Europe [8] research programs. Recent interest in Low Methane Liquid Rocket Engine for reusable launch vehicle and/or large liquid booster application has arisen, involving cooperation between European and Russian industries in the frame of VOLGA program [9] to conceive a LO_X/CH_4 engine for booster applications, with major emphasis on reusability. Thrust class expander cycle liquid oxygen/methane engine for Crew Exploration Vehicle applications is explored by means of a fully integrated engine analysis methodology at *Purdue University* [10], by modelling all major components for the engine including combustion thermal chemistry processes, regenerative cooling jackets, injectors and turbo-pumps assembly.

Among the various aspects concerning the design and the optimization of an oxygen/methane based rocket engine, propellants injection represents one of the most significant item affecting functioning and performance parameters, controlling atomization, vaporization and propellants mixing [11-12]. A wide variety of injector types has been investigated and employed in operational space vehicles, differing in the method for mixing and atomizing the reagents inside the combustion chamber. Among them, shear coaxial injectors offer high performance and stability in a wide operating range of functioning due to good atomization, efficient mixing, uniform distribution of propellants and significant wall compatibility [13], ensuring simple architectures and relatively low costs, so being used in liquid propellant rocket engines such as the *Space Shuttle Main Engine* (*SSME*) and the *Ariane 5 Vulcain II* main engine. Shear coaxial injectors, used extensively both in liquid/liquid and gas/liquid propellant applications, principally experience mixing and atomization by means of the shearing of the liquid by the gas, either combustion chamber gases or injected gaseous propellant. Because of the low rate of mass transfer across the injector orifices, the uniformity of mixing is mainly due to the spacing between oxidizer and fuel jets, requiring rather long combustion chamber length in order to achieve complete mixing [13]. Investigations on sub- and supercritical LO_X/methane injection [8] showed how injector regime conditions exert a wide influence on shear coaxial injector mixing and atomization mechanism. Indeed, above critical conditions with respect to the critical pressure of the oxidizer, propellant injection varies from a problem of atomization of a liquid and mixing of two reactant gases to a one of mixing two gases experiencing a large difference in density. In a typical coaxial injector, below the critical pressure, the liquid oxidizer jet core is atomized due to shear stress induced by the surrounding high-speed gaseous fuel stream. Surface tension induces droplets and ligaments around the central jet that vaporize coming closer to the reaction zone allowing combustion. Above critical conditions, the vanishing of surface tension and latent heat of vaporization lead to the onset of ‘comb-like’ structures while the said change in density arises, in absence of a liquid/gas interface [14-16]. Turbulent diffusion dictates mass transfer from the oxidizer stream towards the reaction zone [17], oxygen no longer experiencing liquid atomization but diffusing directly through turbulent mixing similar to turbulent jets.

Key parameters affecting performance and stability in a shear coaxial injector are, among others, oxidizer post recess length, taper angle and wall thickness at oxidizer post exit. A recessed inner tube with respect to the injection plane is reported to improve atomization and mixing of propellants [13]. Kendrick et al. [18] showed that a recessed oxidizer post of one inner tube diameter, in subcritical conditions LO_X/H_2, enhances flame stabilization inside the injector, inducing expansion angle to spread and size of the volume where reaction takes place to broaden. Under similar operating conditions, Tripathi et al. [19] reported no particular improvement increasing recess further to 1.5 inner post diameter, particularly on high momentum ratio operative points. However, a recess length of about 1.3 d_i in a supercritical LO_X/CH_4 concentric axial injector still leads to combustion efficiency increase [20]. Lux et al. [21] observed an increase of the flame expansion in the near injector element region for a liquid oxygen/methane shear coaxial injector. Locke et al. [22] verified how recessing the inner post in a LO_X/CH_4 shear coaxial injector was shown to increase wall heat flux levels nearby the injector face region due to better oxidizer atomization and mixing.

Silvestri et al. [23-24] reported that an oxidizer post recess enhances the mixing between GO_X and GCH_4 when its length was longer than one inner post exit diameter, even though only a recess of 3x d_i showed a substantial improvement in combustion performance. The longer the recess the higher was the effect on injector pressure drop and heat loads in the near injector region. An increase of combustion stability was shown by Wanhainen et al. [25] and Hannum et al. [26] in a recessed LO_X/H_2 based injector element, as well as in LO_X/kerosene investigations [27].

In this work combustion and heat transfer characteristics of rocket subscale model combustion chambers in supercritical conditions are experimentally and numerically investigated for different combustion chamber pressures, mixture ratios and oxidizer post recess lengths, with a special focus on injector-wall behaviour. A rectangular inner cross-section combustion chamber with optical access is set up and tested at the Institute of Flight Propulsion’s test facility at the Technische Universität München (TUM); a round inner cross-section combustion chamber was previously analysed. A single-element shear coaxial injector is considered for both arrangements, allowing for variation of the inner tube recess length. Optical diagnostic methods are used to characterize the flame behaviour and hot wall temperature profile in the rectangular combustion chamber near-injector region. Results for combustion chamber pressure levels between 10 and 20 bar at variable mixture ratios are presented and discussed.

Chapter 2

Experimental configuration

All experimental test campaigns presented in the following were performed at the Institute of Flight Propulsion's test facility at the Technische Universität München (TUM). The movable test rig (Mobile Rocket Combustion Chamber Test Bench, MoRaP) is operated with gaseous oxygen-gaseous methane (GO_X/GCH_4), designed for nominal interface pressures up to 25 bar, allowing variations in combustion chamber inner cross section, length and injector configuration. A description of the combustion chambers, injector system, measurement equipment and optical diagnostic setup used is given in the following.

2.1 Hardware setup

Two modular capacitive cooled combustion chambers are operated, having rectangular and round inner cross section, respectively. They are designed for a nominal testing time up to 4 seconds, at a pressure level of 20 bar and mixture ratio of 3.4. All combustion chamber segments and nozzle are made of oxygen-free copper (Cu-HCP) and held together by four spiral springs equipped tie rods to ensure constant contact during the hot gas run expansion of the wall material. An overview of the test bed and combustion chamber assemblies is given in *Appendix A*.

The rectangular combustion chamber has an inner square cross section of 12 mm width, featuring a truncated trapezoidal nozzle with a rectangular inner cross section of 4.8 x 12 mm^2. A 50 x 33 x 15.2 mm^3 rectangular cross section quartz glass pane provides optical access to the near injector region. The round combustion chamber features an inner diameter of 12 mm and a conical nozzle with a throat diameter of 7.6 mm. An identical injector centre plane height is guaranteed to allow the same injector/wall distance of 3 mm, while a contraction ratio of 2.5 sets a throat Mach number of 0.24 in both configurations. Ignition is achieved by means of a spark plug initiated GO_X/GCH_4 torch igniter placed in the middle of the combustion chambers to minimize ignition influence. *Tab. 1* resumes main thrust chambers geometrical dimensions. A schematic of the rectangular and round inner cross section combustion chambers is shown in *Fig. 1.a* and *Fig. 1.b*, respectively. More details on the test rig assemblies and run-in test procedures can be found in Bauer et al. [28].

Gaseous nitrogen (GN_2) is used as film coolant during the rectangular combustion chamber run-in operations. A film applicator, placed in the upper part of the injector face-plate, allows film coolant to lap upon the upper surface of the combustor, granting a coolant surface over almost the totality of the width of the combustor and the integrity of the quartz glass optical access during hot firing tests. A film coolant slot length-to-height ratio of 10 ensures two-dimensional flow behaviour assumption. A type *K* thermocouple is installed inside the film manifold, allowing the monitoring of the coolant before the injection inside the combustion chamber. A schematic of the film applicator arrangement and the optical access is shown in *Fig. 2* while a resume of main dimensions of the film applicator is given in *Tab. 1*. An overview of the film injection assembly and of the film applicator is shown in *Appendix A*. More details on the film applicator setup and main parameters can be found in Celano et al. [29]

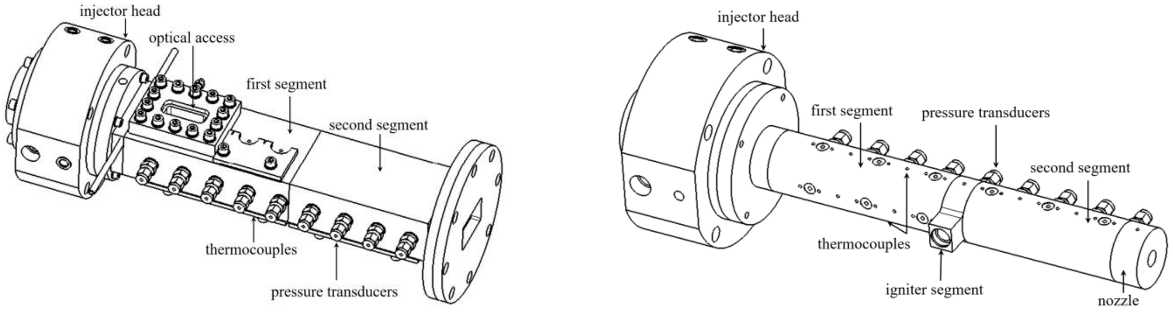

(a) Rectangular combustion chamber **(b)** Round combustion chamber

Fig. 1. Combustion chamber schematic

Table 1. Combustion chamber and film applicator dimensions

		Rectangular	Round
Combustion chamber length	[m]	$290\cdot10^{-3}$	$285\cdot10^{-3}$
Combustion chamber width	[m]	$12\cdot10^{-3}$	-
Combustion chamber height	[m]	$12\cdot10^{-3}$	-
Combustion chamber diameter	[m]	-	$12\cdot10^{-3}$
Throat width	[m]	$7.6\cdot10^{-3}$	-
Throat height	[m]	$4.8\cdot10^{-3}$	-
Throat diameter	[m]	-	$12\cdot10^{-3}$
Throat area	[m²]	$57.6\cdot10^{-6}$	$45.4\cdot10^{-6}$
Contraction ratio	[-]	2.5	2.5
Characteristic length	[m]	$725\cdot10^{-3}$	$710\cdot10^{-3}$
Maximum chamber wall thickness	[m]	$36.5\cdot10^{-3}$	$19\cdot10^{-3}$
Film applicator slot height	[m]	$0.25\cdot10^{-3}$	-
Film applicator slot width	[m]	$8\cdot10^{-3}$	-

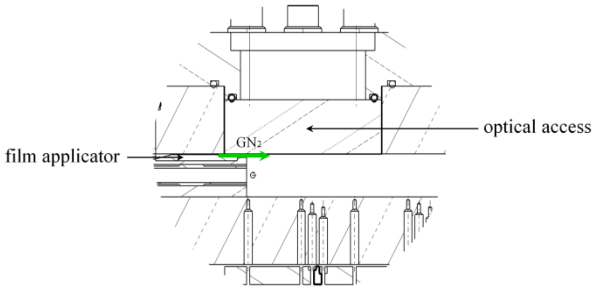

Fig. 2. Rectangular combustion chamber optical access and film applicator schematic

2.2 Injector setup

The injector used is of a shear coaxial type, centred in the face-plate by means of four equally-spaced fins inclined at an angle of 45° with regard to the combustion chamber centre plane.

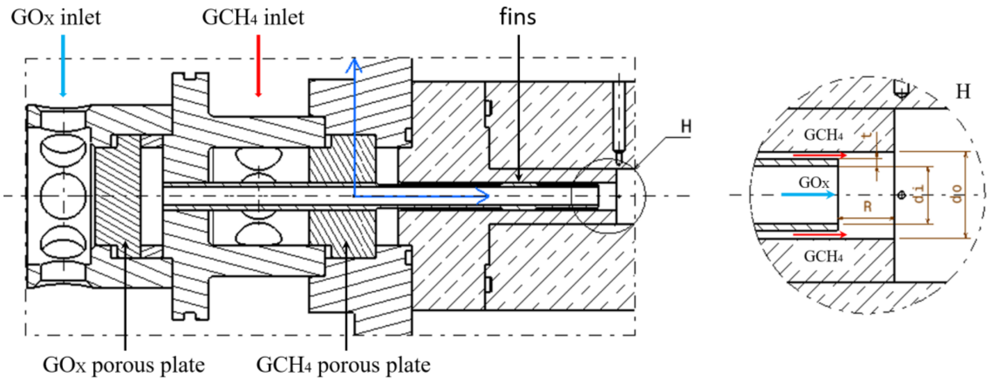

Fig. 3. Injector head schematic

The injector head allows for variations in oxidizer post recess length – *R* – by means of variable thickness spacing rings housed inside the injector dome. For both combustion chamber configurations a flush mounted (*R0*) and three recessed injector arrangements are tested: 6 mm (*R6*), 9 mm (*R9*) and 12 mm (*R12*) inner tube recess lengths for the round inner cross section combustion chamber, corresponding to 1.5x, 2.25x and 3x d_i, respectively; 9 mm, 12 mm and 15 mm (*R15*) for the rectangular one, corresponding to 2.25x, 3x and 3.75x d_i, respectively. An overview of the injector head annular spacing rings is given in *Appendix A*. Two porous plates in the oxidizer and fuel manifolds guarantee uniform injection inside the combustion chamber and acoustic decoupling between the combustor and the propellants feed lines by means of

Table 2. Injector element dimensions

GOx inner diameter	d_i	[m]	$4 \cdot 10^{-3}$
GCH$_4$ outer diameter	d_o	[m]	$6 \cdot 10^{-3}$
GOx post wall thickness	t	[m]	$0.5 \cdot 10^{-3}$
GOx post length	l	[m]	$96 \cdot 10^{-3}$
GOx post recess	*R0*	[m]	0
GOx post recess	*R6*	[m]	$6 \cdot 10^{-3}$
GOx post recess	*R9*	[m]	$9 \cdot 10^{-3}$
GOx post recess	*R12*	[m]	$12 \cdot 10^{-3}$
GOx post recess	*R15*	[m]	$15 \cdot 10^{-3}$
Taper angle	-	[°]	0
Injector area ratio	A_{GCH4}/A_{GOx}	[-]	0.7

a monitored pressure drop. Pressure transducers *WIKA A10* allow the monitoring of manifold pressure values upstream the injector for both oxidizer and fuel before they enter the combustion chamber. A resume of the main geometrical dimensions of the injector element is given in *Tab. 2*. A schematic of the injector head, with a zoom on the recessed oxidizer post, is depicted in *Fig. 3*.

2.3 Measurement equipment setup

Both the hardware are provided with standard measurement equipment to characterize combustion chamber operative conditions. In addition, the rectangular inner cross section combustion chamber is equipped with optical diagnostic equipment to investigate the behaviour of the flame in the near injection region.

Nine equally spaced – each 34 mm – pressure transducers *WIKA A10* placed on the side of the combustion chamber (*PC0,…,PC8*) allow for evaluation of the pressure distribution along the combustor axis. The first pressure transducer (*PC0*) is positioned 0.5 mm away from the injector face-plate. All the pressure transducers are individually calibrated and operated at a data acquisition rate of 100 Hz.

Temperature distribution is investigated by means of type *T* thermocouples of 0.5 mm diameter, with a spacing of 17 mm along the combustion chamber longitudinal axis, 1 mm distance from the inner hot gas wall, the first thermocouple being positioned 0.5 mm away from the injector face-plate. In the round combustion chamber, the type *T* thermocouples are installed on the upper surface of the first and second segments, in the rectangular one on the bottom of both the combustion chamber segments, to minimize the influence of the quartz glass optical access on temperature evaluation. Additionally, type *T* thermocouples are mounted in the first segment of the round combustion chamber 3 mm distance from the inner hot gas wall with an angle of 90°, at the same measurement axial locations. Thermocouples at 2 mm and 3 mm distance from the inner wall are placed in the first segment of the rectangular combustion chamber, with a spacing of 3.5 mm along the longitudinal axis, thus forming four equally spaced clusters of three thermocouples at 1, 2 and 3 mm from the hot-wall. Two *Medtherm* coaxial type *T* thermocouples are positioned on the top of the rectangular combustion chamber first segment, flush mounted with the wall, while five type *K* surface thermocouples are place to its external surface. A spring loaded system ensures contact between type *T* thermocouple tips and the base

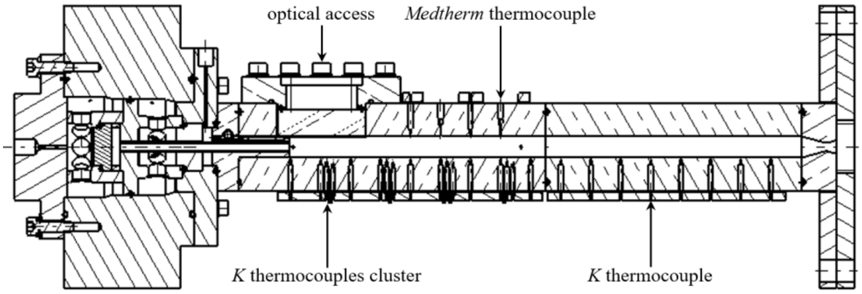

(a) Rectangular combustion chamber

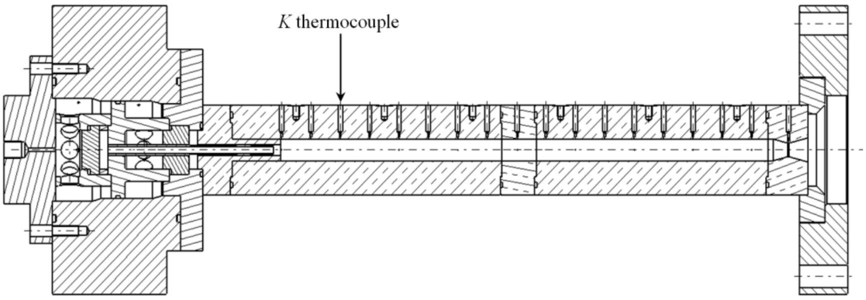

(b) Round combustion chamber

Fig. 4 Combustion chamber measurement equipment schematic

of the housing holes, providing a constant force of about 2 N, thus minimising the chance of potential loss of contact because of vibrations or material expansion/contraction during hot firing tests [30]. *Medtherm* thermocouples are press-fitted into the chamber wall. Injector conditions are monitored by means of type *K* thermocouples with 0.5 mm diameter positioned in both oxidizer and fuel manifolds, prior the porous plates. An overview of the measurement equipment arrangement for the two combustion chambers is depicted in *Fig. 4.a* and *Fig. 4.b*.

2.4 Optical diagnostic setup

A *BU205M* monochromatic camera, CMOS image sensor provided, is used to visual investigate the flame behaviour in the near injector element region of the rectangular cross section combustion chamber through a quartz glass optical access providing a 40 mm x 13 mm flat view. A *Schott UG11/Schott WG305* double spectral filter arrangement is operated allowing investigation of hydroxyl (*OH*) radical emissions. A frame of 168 Hz with an optical resolution of 2048 x 1088 pixels is guaranteed. 5000 *μs* exposure is set while the filter is operated, 50 *μs* otherwise. More details on the optical diagnostic setup can be found in Winter et al. [31]. A scheme of the optical access is shown in *Fig. 4.a.* An overview of the optical measurement equipment assembly and optical access is given in *Appendix A.*

Chapter 3

Operative conditions

All experimental run-in tests were performed at least twice to ensure repeatability of the results, for both the rectangular and the round combustion chamber. Sonic orifices in oxidizer and fuel feed lines and corresponding upstream pressure values set mass flow rates inside the combustion chamber. Orifices were individually calibrated before each test campaign by means of a Coriolis flow meter featuring gaseous nitrogen to ensure measurement accuracy. To this end, discharge coefficient – C_d – is introduced as a function of upstream temperature and pressure values in the mass flow rate evaluation routine [32].

A burning time of 3 seconds, limited because of the capacitive nature of the combustors, is set for both combustion chamber hot firing test campaigns, as well as the same sequence routine is granted, except for film coolant injection. An ignition interval of *300 ms* at minimum igniter power to achieve the initiation of the flame is set to minimize the influence on the evaluation procedure. To ensure comparability between the hardware and due to the transient characteristic of heat sink arrangements an evaluation time (t_{eval}) at 2/3 of the hot run is chosen, right before the end of the firing. A start up (t_{start}) and a shut down time (t_{end}) are also considered. To minimize the transient nature of ignition, physical and performance parameters are evaluated as a mean value over 0.5 seconds at the evaluation time. A piecewise linear fit is applied on pressure distribution to reduce non-uniformity due to signal noise. An overview of the characteristic time intervals over standard hot run pressure and temperature distributions is depicted in *Fig. 5*.

Film cooling has been set when the rectangular combustion chamber was tested in order to prevent crack enucleation and propagation inside the optical access quartz glass window; the influence of the film coolant injection on the combustion characteristic parameters is discussed in *Chapter3, Paragraph 3*. An approach granting combustion chamber pressure and mixture ratio similarity is adopted to compare the two hardware, mass flow rate being set consequently, according to the throat cross section area.

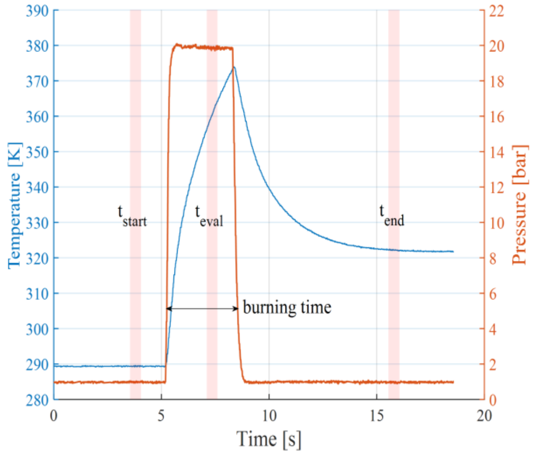

Fig.5. Characteristic time intervals over pressure and temperature time distributions

3.1 Round combustion chamber

Run-in tests at nominal combustion chamber pressure (P_C) of 10 bar and 20 bar, at mixture ratio (*O/F*) of 2.2, 2.6, 3.0 and 3.4 were previously performed on the round combustor hardware, fuel and oxidizer mass flow rates being scaled with pressure level as regard as oxidizer-to-fuel ratio variation. A resume of the test matrix is outlined in *Fig. 6.a*. The corresponding actual combustion chamber pressure values are depicted in *Fig. 6.b.* It is clear how, for the 20 bar nominal pressure load points, the oxidizer post recess length *R12* experiences a higher mean combustion chamber pressure under the same total mass flow rate conditions, if compared with lower recesses. Therefore, an improvement in combustion related performance is expected.

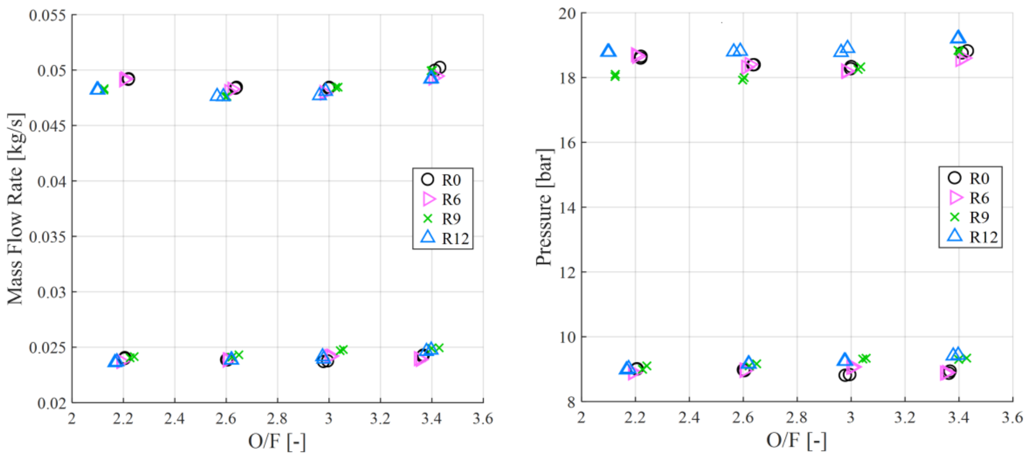

(a) Combustion chamber mass flow rate **(b)** Mean combustion chamber pressure

Fig. 6. Round combustion chamber operative load points

3.2 Rectangular combustion chamber

According to the round combustion chamber operating conditions, run-in tests at nominal combustion chamber pressure of 20 bar and mixture ratio of 2.2, 2.6, 3.0 and 3.4 are performed on the rectangular combustor. Fuel and oxidizer mass flow-rates were consequently scaled with pressure level as regard as the oxidizer-to-fuel ratio variation. A 10% film coolant mass flow rate with respect to the fuel mass flow rate is set for all the run-in tests conditions. In addition, no film cooling routines are performed for mixture ratios 2.2 and 3.4 and oxidizer post recess reference case (*R0*) and *R12* to validate the comparison between the two hardware geometries. Load point results for both with- and without-film cooling repetitions are reported in the following chapters. A resume of the test matrix is outlined in *Fig. 7.a.* and *Tab.3*. The corresponding actual combustion chamber pressure is depicted in *Fig. 7.b.* It is herein recalled how the oxidizer-to-fuel ratio values depicted for the film cooling operation results are referred to the injection, rather than throat conditions. It is clear, as underlined for the round combustion chamber arrangement, how a recessed oxidizer post grants a higher combustion chamber pressure threshold if compared to the relative flush-mounted configuration, the same total actual mass flow rate being experienced. An increase in combustion performance is expected, then, as previously pointed out.

Table 3. Rectangular combustion chamber load points

	OF = 2.2	OF = 2.6	OF = 3.0	OF = 3.4
R0	■ □	■	■	■ □
R9	■	■	■	■
R12	■ □	■	■	■ □
R15	■	■	■	■

■ 10% film

□ 0% film

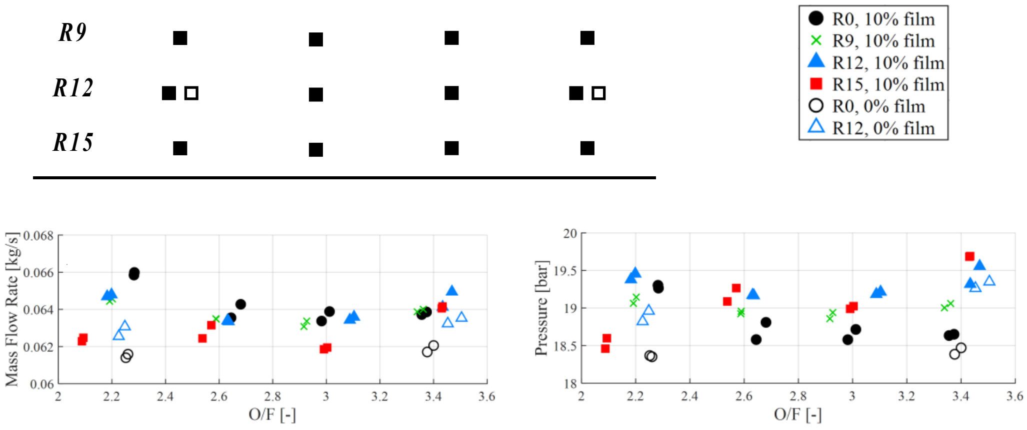

(a) Combustion chamber mass flow rate **(b)** Mean combustion chamber pressure

Fig. 7. Rectangular combustion chamber operative load points

3.3 Film cooling influence

An insight on film cooling effects on combustion characteristics is outlined for the rectangular inner cross section combustion chamber, to corroborate comparisons between round and square hardware. To this end, main combustion parameters are laid out and discussed in the following, taking into account film coolant injection. Results for mean combustion chamber pressure of 20 bar and mixture ratio 2.2, on the left, and 3.4, on the right, are analysed.

Averaged normalized wall pressure distribution along combustion chamber axis – *z* – is depicted in *Fig. 8*. Standard error of the mean – *SE, Appendix B* – between the *n* test repetitions is also shown in the form of bar graphs for each axial position and injector configuration. Last pressure sensor reading, placed closely upstream the nozzle – *z = 272 mm* –, is chosen as normalization factor, in order to investigate the recirculation zone near the face-plate. Film coolant injection slightly affects pressure distribution over combustion chamber axis in the flush-mounted injector configuration, mostly in the near injection area, where the coolant is injected. A higher static pressure to the wall is thus encountered for film cooling procedures, as already found for the mean combustion chamber values. A maximum discrepancy less than 0.5% is calculated for both O/F when film cooling is set. Film effect is negligible proceeding along the axial length, then. No significant influence on the recessed case is experienced for both oxidizer-to-fuel ratios, the two pressure trends overlapping along the whole chamber axis.

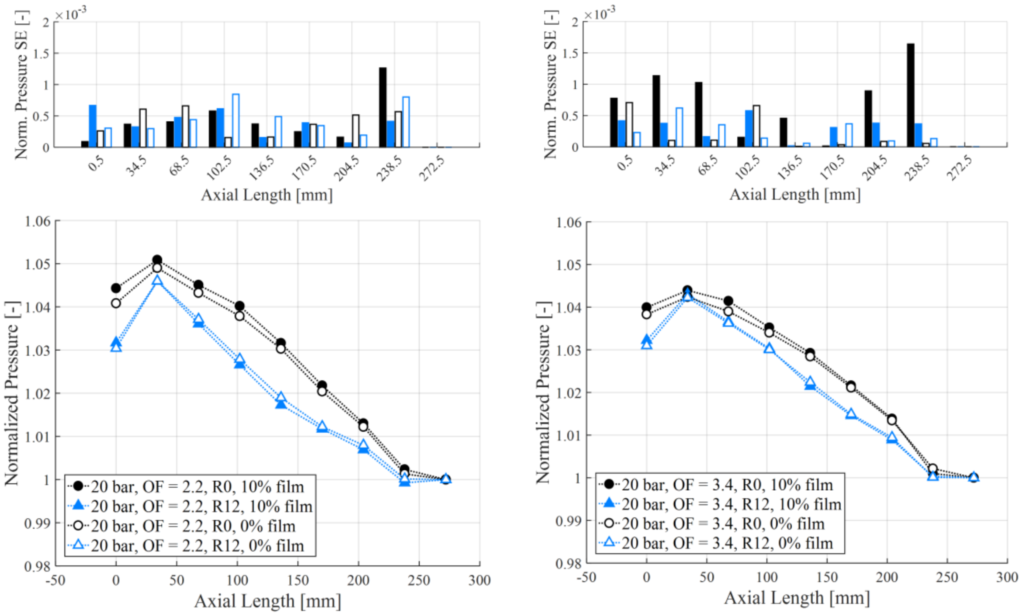

(a) O/F = 2.2 **(b)** O/F = 3.4

Fig. 8. Rectangular combustion chamber normalized pressure distribution – Film comparison

Film cooling injection is reported to affect the axial temperature distribution inside the measurement error range, as depicted in *Fig. 9*. Thermocouples at 1 mm distance from the hot gas wall are considered. Axial temperature distribution at evaluation time for mixture ratio equals to 2.2 *(a)* and 3.4 *(b)* and both repetitions is shown.

While for the flush-mounted injector configuration a significant similarity of the data is achieved between with- and without-film run-in tests, a slight difference is visible for the recessed injector arrangement and O/F = 2.2, particularly in the face-plate surroundings where the flame attaches the chamber wall and film coolant injection is reported to decrease the wall temperature. A maximum relative decrement of around 2% is here evaluated. However, for a heat sink combustion chamber the higher the initial temperature of the hardware, the higher the hot run combustion temperature,

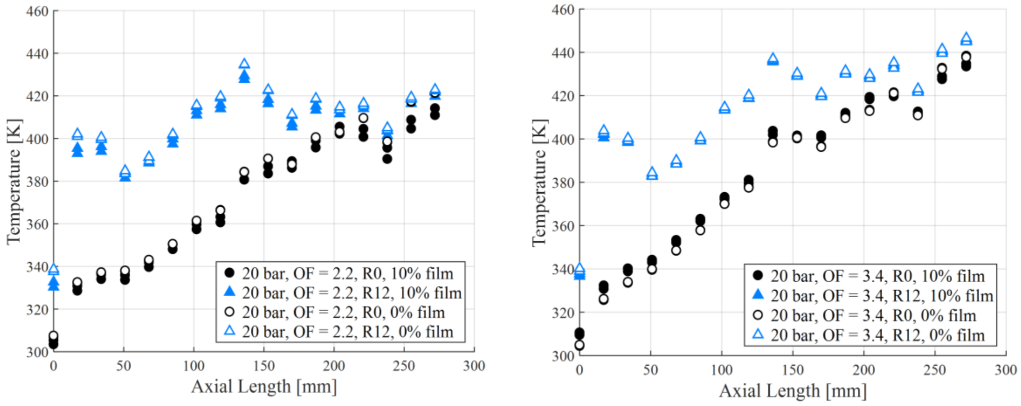

(a) O/F = 2.2 **(b)** O/F = 3.4

Fig. 9. Rectangular combustion chamber temperature at evaluation time – Film comparison

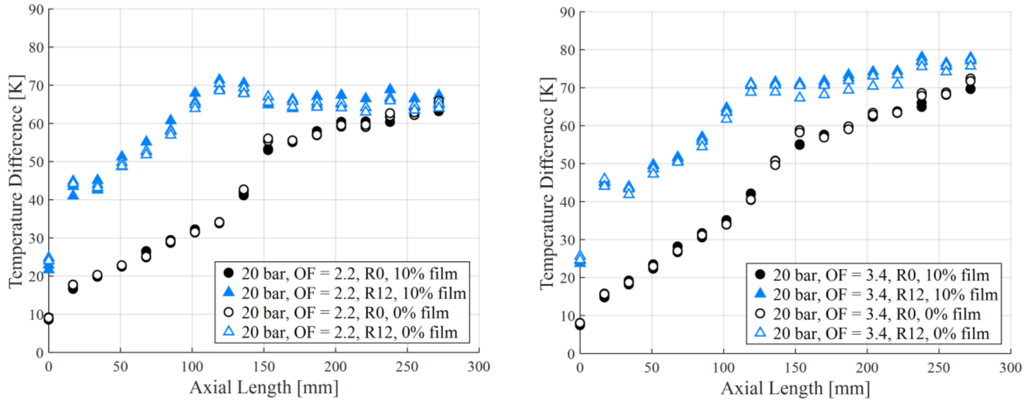

(a) O/F = 2.2 **(b)** O/F = 3.4

Fig. 10. Rectangular combustion chamber temperature difference at evaluation time – Film comparison

same combustion runtime being experienced. The difference in temperature profiles between evaluation time and *0.5* seconds after ignition is considered and outlined in *Fig. 10*. Temperature difference distribution exhibits a lower deviation if compared with the aforementioned absolute temperature profile, lying inside the experimental confidence interval. To better characterize film cooling influence over temperature distribution, temperature profile over burning time is outlined in *Fig. 11*, for O/F 3.4 and *R0* and *R12* injector configurations. The O/F 2.2 was experiencing the same qualitative behaviour. The first four thermocouples at 1 mm distance from the hot-wall are considered at z = *0.5 mm*, *17.5 mm*, *34.5 mm* and *51.5 mm* apart from the injector face-plate, respectively. The initial temperature (t_{start}) is chosen as reference for normalization. Repetition test mean values are reported. An overall maximum standard error of the mean between the two repetition tests for each thermocouple axial position is outlined, showing good repeatability agreement. Maximum differences between corresponding temperature distributions with (T^F) and without (T^{HOT}) film cooling are also shown for each axial position. A significant overlapping of the temperature signals with and without film coolant injection is herein obtained, differences between the two operational conditions lying inside the experimental uncertainty of measurement, on average. This confirms that the film coolant injection amount is reported not to influence in a substantial manner temperature profiles over time and space. This could be due to the placement of the thermocouples on the lower part of the rectangular hardware, thus measurements not being highly affected by the film coolant injection on the upper part of the combustion chamber wall. Moreover, the presence of the cold nitrogen film solely on the upper wall of the combustor is supposed to possibly induce a downward displacement of the hot gas flow, as already indicated by Celano et al. [29], thus higher temperature readings in the lower part of the hardware could arise.

$SE_{max} = 2.1\ K$ $SE_{max} = 5\ K$ $SE_{max} = 4.8\ K$ $SE_{max} = 3.8\ K$

$(T^{HOT} - T^F)_{max} = 1.9\ K$ $(T^{HOT} - T^F)_{max} = 1.4\ K$ $(T^{HOT} - T^F)_{max} = 0.8\ K$ $(T^{HOT} - T^F)_{max} = 2.9\ K$

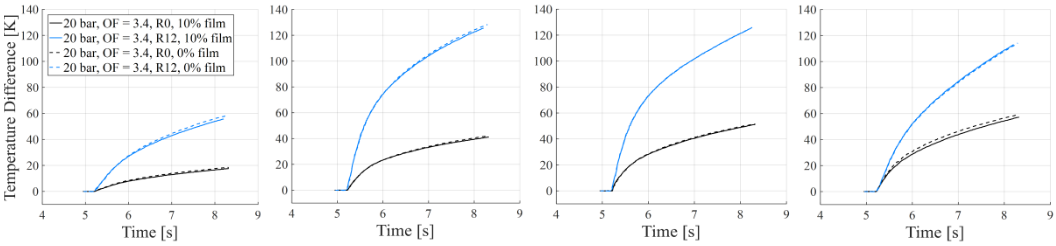

(a) z = 0.5 mm **(b)** z = 17.5 mm **(c)** z = 34.5 mm **(d)** z = 51.5 mm

Fig. 11. Rectangular combustion chamber temperature difference over burning time – Film comparison

Heat flux axial distribution is also reported for comparison on film coolant injection influence. To this end, an inverse computational method for heat flux evaluation has been developed [33-34] based on thermocouple measurements (*Chapter 4. Paragraph 3*). Bartz [35] reported how the heat transfer coefficient is proportional to the mean pressure value to the power 0.8. Since hot gas temperatures are significantly higher than the combustion wall material axial gradient, the same scaling approach can be extended to the wall heat flux, this being proportional to the heat transfer coefficient and the temperature difference between the material wall and the gas flow. A correction of the heat flux is introduced, taking into consideration the variation in mass flow rate for different tests. A correlation taking into account for partial and total mass flow rates has been applied, as in *Eq. 3.1* to decouple the contribution on the combustion chamber pressure due to different mixing efficiencies [23].

$$\dot{q}_{ref} = \dot{q}_{test}\left[\frac{(\dot{m}c^*_{th})_{nom}}{(\dot{m}c^*_{th})_{test}}\right]^{0.8} \tag{3.1}$$

Wall heat flux axial distribution for both mixture ratios and injector configurations tested is depicted in *Fig. 12*, film cooling injection being considered. An overview of maximum errors between with and without film cooling routines is also discussed.

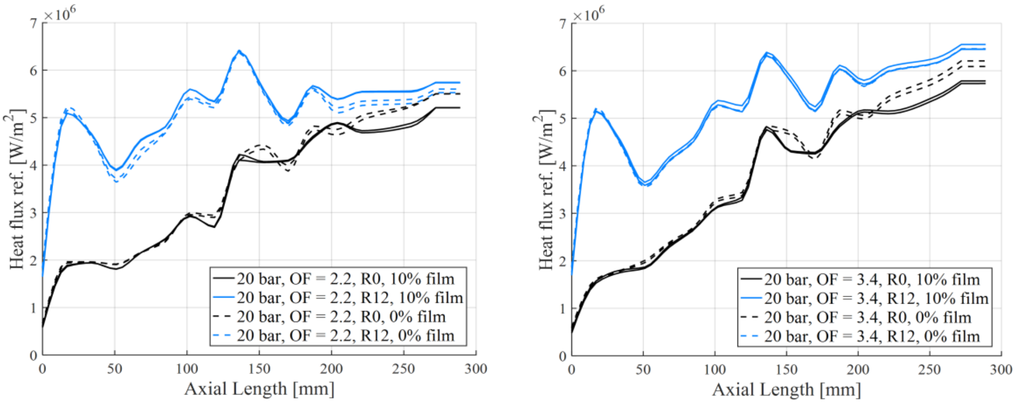

(a) O/F = 2.2 **(b)** O/F = 3.4

Fig. 12. Rectangular combustion chamber heat flux axial distribution – Film comparison

Same distribution patterns are obtained for both oxidizer-to-fuel ratio 2.2 and 3.4. A continuous increase of the heat flux along the combustion axis, typical of a steady combustion process in a capacitive hardware, can be observed. Good agreement on data patterns between with and without film cooling hot runs is achieved for the recessed injector configuration, a maximum difference on mean value distributions being about *0.2 MW/m²* for O/F equals to 2.2. A substantial overlap is visible for O/F 3.4. A slightly different behaviour is detected for the flush-mounted injector configuration. While heat flux distribution experiences a similar trend in the first part of the combustion chamber, film coolant injection routine being or not being considered, a more evident discrepancy is observed in the second segment. This behaviour could be due to two concurrent aspects, the one physical the other numerical. The onset of the divergence between the profiles is reported to arise corresponding to the junction of the first and second segments of the combustion chamber, where the torch igniter is placed, so film cooling routine possibly affecting ignition footprint on the capacitive hardware, as can be seen in the temperature profile in *Fig. 10* for the non-recessed case. In fact, energy released during the ignition process is absorbed by the capacitive combustor wall producing heterogeneities in the wall material temperature distribution that require a certain time to dissipate [36]. In this respect, numerical heat flux computing from temperature readings and conduction characteristic of the combustor wall can concur in error propagation, high conductivity of copper being reported to flatten temperature profiles. A maximum difference of about $0.3\ MW/m^2$ is found for the flush-mounted injector configuration in the second part of the combustion chamber, for both mixture ratios analysed, where a lower heat flux to the wall is calculated for the film cooled test cases.

Methane and oxygen discharge coefficients with and without film cooling injection for both injector configurations and mixture ratios are displayed in *Fig. 13*. Injection conditions are evaluated by means of the first pressure sensor inside the combustion chamber and the relative propellant manifold characteristics. An overall agreement on data is evidenced, recessed injector configuration experiencing a maximum discrepancy of around 5% for methane side at O/F 2.2. To this end, an oxidizer post recess length may be addressed to play a role, as can be inferred from the methane side results, primarily. Indeed, the presence of a recessed inner oxidizer tube is reported to accelerate the propellants inside the recessed region due to the blockage of the triggered flame and the consequent reduction of the available cross section area. A variation of the velocity of the injected propellants could influence the relative mixing between the core and the film coolant flows, highly dominated by the film flow impulse to the hot gas stream. Consequently, a larger influence should be expected for the methane side and low oxidizer-to-fuel ratios where the predominant methane flow experiences higher injection velocities.

Influence of film coolant injection on combustion efficiency is investigated, lastly. Combustion efficiency (*Eq. 3.2*) for a liquid rocket engine can be defined [37] as the ratio of the measured experimental characteristic velocity to the theoretical ideal (complete combustion) characteristic velocity of the combusted exhaust products. To

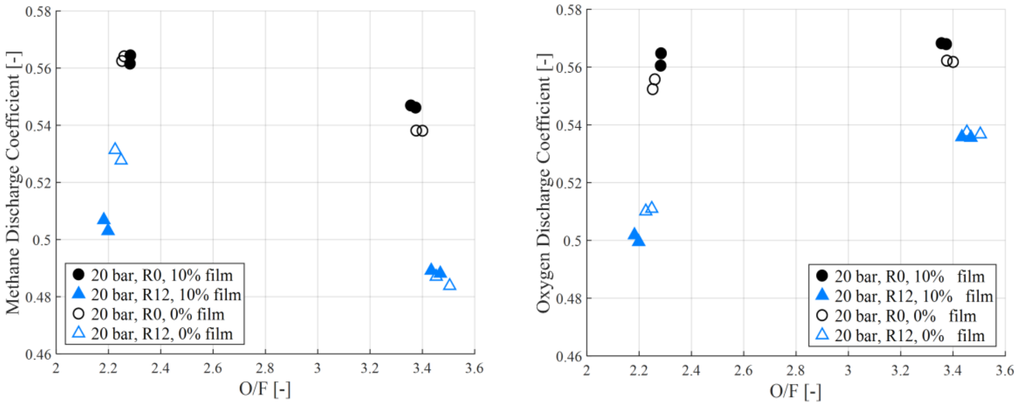

(a) Methane **(b)** Oxygen

Fig. 13. Rectangular combustion chamber discharge coefficients – Film comparison

$$\eta_{c^*} = \frac{c^*_{test}}{c^*_{theo}} \tag{3.2}$$

this end, Gordon-McBride [38] *CEA* code is adopted to give an estimate of the theoretical characteristic velocity. Two approaches are considered: a *thrust chamber* ($\eta^{TR}_{c^*}$) combustion efficiency and an injector related *energy release* ($\eta^{ER}_{c^*}$) combustion efficiency are evaluated, the former considering adiabatic wall conditions – consistently with CEA assumptions – the latter taking into account energy losses towards the combustor walls for inlet enthalpies correction. In addition, frozen as well as equilibrium approaches are considered in chemical kinetics analysis, the two not inducing remarkable differences – lower than 0.1% – on performance evaluation. equilibrium approach results are presented in this work, unless otherwise stated. Potential boundary layer displacement in the nozzle throat due to the film is neglected, finally. Thrust chamber and energy release combustion efficiencies are presented in *Fig. 14*, on the left and on the right, respectively. A certain scatter on data is visible, combustion efficiency being clearly dependent on film coolant mass flow rate and mixture ratio, as reported by Kirchberger et al. [39] for gaseous oxygen / liquid kerosene mixture and reagent film coolant injection. Even if nitrogen film coolant is not reported to taking part in the combustion process, due to its inert nature, a noticeable dispersion is herein evaluated, too. Indeed, coolant injection affects injected total mass flow rate and mean combustion chamber pressure levels, as shown in *Fig. 7*, so influencing total pressure to the wall at the nozzle throat. Differences are

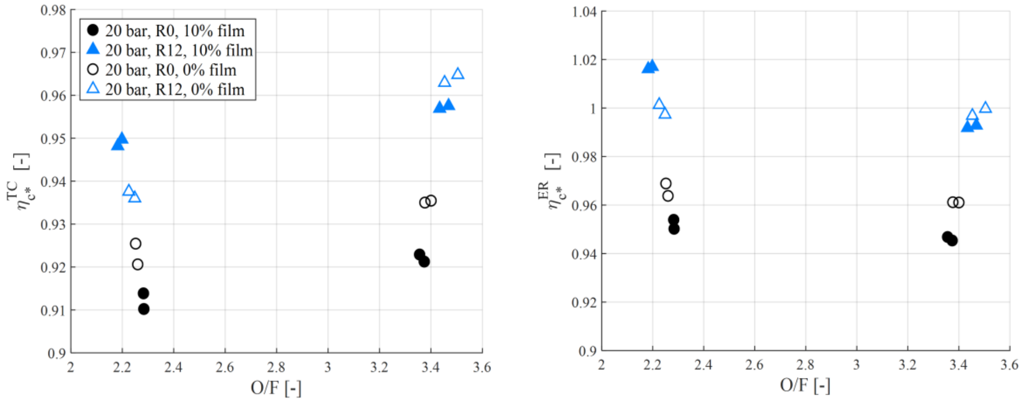

(a) Thrust Chamber combustion efficiency **(b)** Energy Release combustion efficiency

Fig. 14. Rectangular combustion chamber combustion efficiency – Film comparison

evaluated to settle less than 2%, for both calculation approaches, without regards of post recess length, diminishing with mixture ratio increase. A lower combustion efficiency is calculated for film cooled test conditions for all the test cases except for the lower mixture ratio and *R12* recess length where an increase in combustion efficiency arises for the 10% film run. A similar inverse trend behaviour than the other tested load points was noticed in the discharge coefficient evaluation, for both methane and oxygen sides, for the 12 mm recess length and oxidizer-to-fuel ratio equals to 2.2. This also applies to heat flux evaluation, where a higher heat release is found for the film-cooled test case within the last third of the combustion chamber lenght for O/F 2.2 and *R12* recess length. This said, the decrease in combustion efficiency for the film cooled test conditions should be further investigated.

A comparison between with and without film cooling operations on the rectangular hardware reveals a significant agreement on data for the wall pressure distribution along the combustion chamber axis as well as a certain match is encountered in the temperature profile over axial coordinate and burning time for both mixture ratios and injector configurations analysed. This may be assigned to the positioning of the thermocouples on the bottom part of the square hardware, thus measurements being only partially affected by the film injection on the upper wall material to ensure the integrity of the quartz glass window. A good comparability is reached in heat flux trends too, even though the presence of the film coolant solely in the upper wall of the combustion chamber could influence the hot gas jet dynamics in a non-symmetric manner as well as the capacitive nature of the hardware could promote transverse heat transfer from the uncooled walls [29]. Film cooling injection is reported to lightly influence orifice discharge coefficients, whereas a higher scatter on data is found on combustion efficiency assessment. For the purpose of the present work, differences are evaluated to fall in an acceptable range for both the load points and the tested injector arrangements, even if further investigations are promoted. A comparison between the rectangular and round combustion chambers, the one experiencing film coolant injection the other not being film-cooled, is validated.

Chapter 4

Experimental results

Experimental run-in test results for both the round and the rectangular combustion chambers are investigated and discussed in Chapter 4, Paragraphs 1 to 4. Significant agreement between repeatability tests are achieved for both combustor arrangements, mixture ratios and injector configurations, mean value distributions and performance parameters being shown, unless otherwise stated. Standard error of the mean is used as confidence interval for repeatability and illustrated in the form of bar graphs. Results for oxidizer-to-fuel ratio 2.2 and 3.4 and *R0*, *R6*, *R9*, *R12* post recess lengths for the round combustion chamber and *R0*, *R9*, *R12*, *R15* post recess lengths for the rectangular combustion chamber are presented. Film coolant injection is considered for the rectangular hardware tests.

Since mixing efficiency of a shear coaxial injector is mainly due to the shear forces between oxidizer and fuel flows, non-dimensional parameters are employed and preliminary evaluated: velocity ratio (*VR*) and momentum flux ratio (*J*), defined as in *Eq. 4.1* and Eq. *4.2,* are calculated and depicted in *Fig. 15* and *Fig. 16* for both the combustion chamber arrangements, different mixture ratios and 20 bar test cases. Both the parameters are based on the propellants characteristics in the manifolds. No significant differences, except for mixture ratio 2.2 where a higher scattering depending on recess is visible, are encountered for the two combustor configurations, same mixture ratio and injector geometry being analysed. A similar injector behaviour is expected, then, an increasing in fuel-to-oxidizer velocity ratio and momentum flux ratio enhancing mixing process.

$$VR = \frac{u_{GCH4}}{u_{GOX}} \tag{4.1}$$

$$J = \frac{(\rho u^2)_{GCH4}}{(\rho u^2)_{GOX}} \tag{4.2}$$

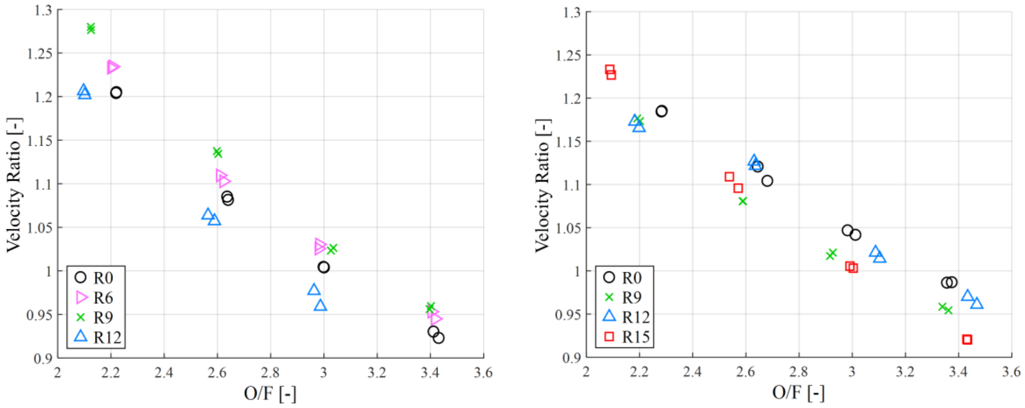

(a) Round combustion chamber, P_C = 20 bar **(b)** Rectangular combustion chamber, P_C = 20 bar

Fig. 15. Velocity ratio

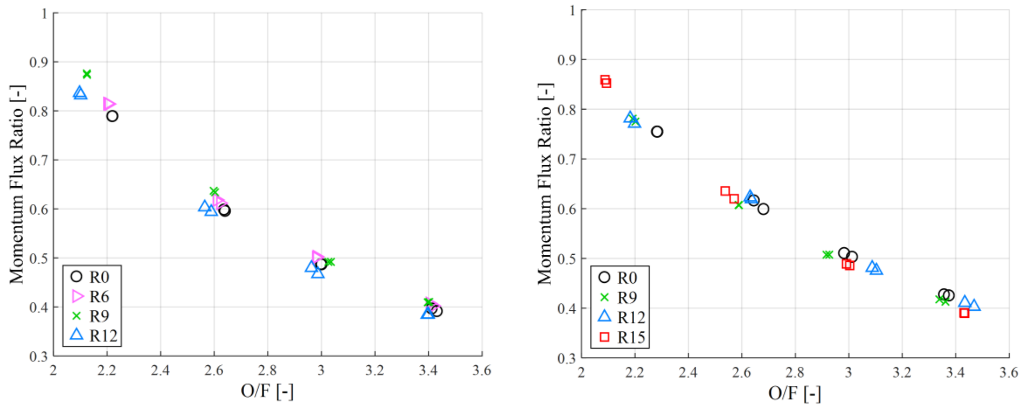

(a) Round combustion chamber, P_C = 20 bar **(b)** Rectangular combustion chamber, P_C = 20 bar

Fig. 16. Momentum flux ratio

4.1 Pressure distribution

4.1.1 Pressure distribution along combustion chamber axis

Normalized pressure distribution along the combustion chamber axis for the round combustion chamber (on the left) and the rectangular combustion chamber (on the right) is evaluated and depicted in *Fig. 17* and *Fig. 18*, for nominal combustion chamber pressure of 20 bar and mixture ratio 2.2 and 3.4, respectively. The influence of the recess length is presented and discussed. An overview of the related standard error of the mean for all the axial positions over the combustion chamber length and injector configurations is also shown.

The injected gases are accelerated from the injection velocity to the hot gas velocity, because of the combustion process. A decrease in the wall pressure distribution along the combustion chamber axis is then expected. A flattening of the wall pressure gradient is representative of the accomplishment of the combustion process along the hardware axial position. A relatively strong drop in wall pressure in the near-injection zone is visible for all run-in tests, sign of the presence of a

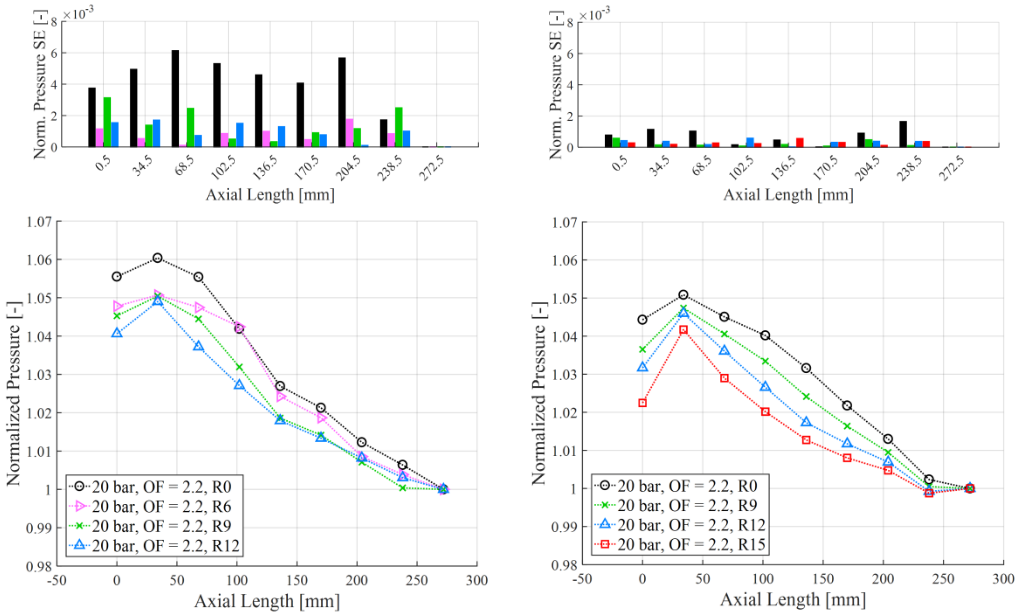

(a) Round combustion chamber **(b)** Rectangular combustion chamber

Fig. 17. Normalized pressure distribution along combustion chamber axis – O/F = 2.2

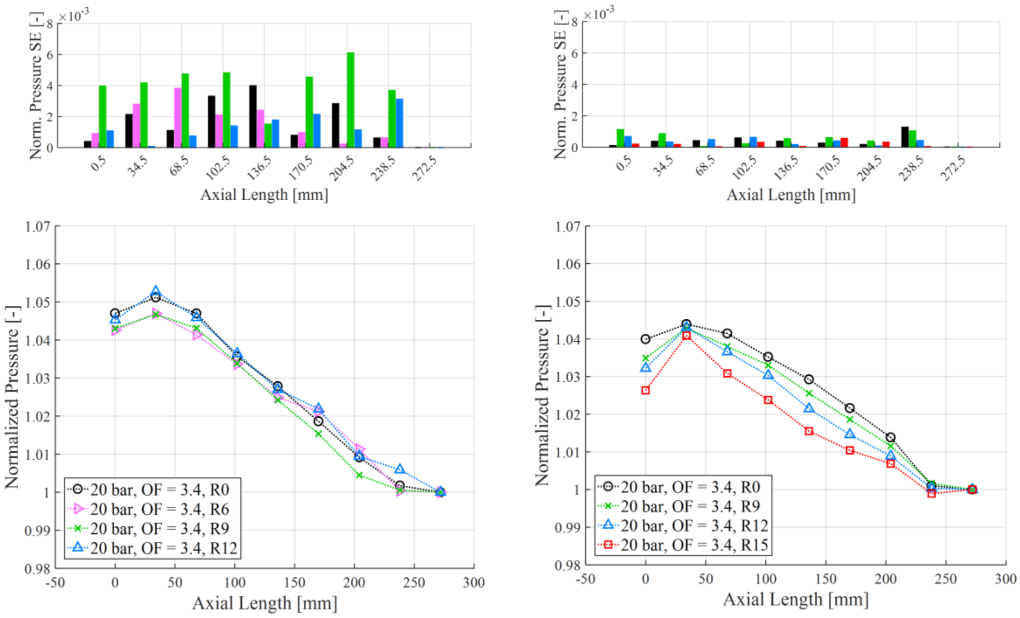

(a) Round combustion chamber **(b)** Rectangular combustion chamber

Fig. 18. Normalized pressure distribution along combustion chamber axis – O/F = 3.4

recirculation zone due to the heat release and consequent expansion of the gas after the injection inside the combustion chamber. The higher the mixture ratio the lower the drop in the wall pressure at the face-plate for both the hardware and injector configurations, lower mixture ratios featuring higher methane velocity and momentum flux. Since the two combustion chambers experience almost the same characteristic length, defined as the ratio of the combustion chamber volume to the nozzle throat area, the residence time of the propellants inside the combustors is almost the same, so combustion processes, heat release as well as pressure distribution along the combustion chamber axis being similar for a same inner post recess, as stated in Silvestri et al. [40], where a detailed study on scaling approaches between the two hardware being investigated can be found. Stagnation point occurs simultaneously in space for the two configurations, independently from the oxidizer post recess length and mixture ratio. A higher pressure increase is found for both mixture ratios in the rectangular combustion chamber if compared to the round one, same recess length being considered. This could be due to the larger combustion volume available because of the presence of the corners, enhancing flow recirculation, and so more intense initial mixing of the shear layer. Moreover, the presence of a round flame in a rectangular combustion chamber could influence combustion process in the near-injector zone, where the flame is not yet adapted to the square shape [40]. A lower pressure decay along the combustion chamber axis is found for the rectangular hardware arrangement increasing oxidizer inner post recess, as already seen in Silvestri et al. [23] for the round combustion chamber. This can be associated to a better mixing of the propellants. Indeed, fuel and oxidizer, already mixed and accelerated inside the recessed region, are injected inside the combustion chamber experiencing higher velocity, so requiring less acceleration to reach full combusted gas velocity. When the flame develops inside the recessed region, a certain fraction of the available area is occupied, the methane flow being accelerated. A stronger influence on pressure decay reduction along the chamber axis by increasing recess length is exerted for mixture ratio 2.2, rather than 3.4. Indeed, a recessed injector configuration does not alter significantly the pressure decay along the combustion chamber axis for mixture ratio equals to 3.4, a pressure gradient of about 4% and 5% being experienced for the rectangular and round hardware, respectively, regardless of inner post recess length. Conversely, a different behaviour has been detected for the lower oxidizer-to-fuel ratio. Indeed, a reduction of about 1% in the pressure decay over the combustion axis is reached for all the recessed injector geometries and O/F 2.2 in the round combustion chamber, if compared to the flush-mounted injector assembly. The same behaviour is evident for the rectangular arrangement, where a further increase of the recessed region to 15 mm (*R15*) reduces pressure decay of about 1% compared to the reference case.

An influence on axial pressure trend shape is exerted by the combustion chamber inner cross-section geometry, too. Round geometry being considered, the normalized pressure distribution along the combustion chamber axis is only slightly affected by the introduction of a recess length for the higher mixture ratio tested. On the contrary, the presence of an oxidizer post recess modifies the pressure distribution shape for the lower oxidizer-to-fuel ratio condition, a flattening of the pressure trend being more evident in the second segment of the combustor increasing recess length. This can be related to an earlier achievement of the combustion end for the recessed case, if compared to the flush-mounted injector configuration, as shown in Silvestri et al. [23]. The same behaviour is evident for the rectangular assembly even though both mixture ratios are now affected by the presence of a recessed injector geometry in this latter case. The influence of the combustion chamber geometry on the normalized pressure distribution is evident if the effect of the mixture ratio is considered in more detail. The normalized pressure trend along the combustion chamber axis is reported in *Fig. 19*, the round hardware on the top, the rectangular one on the bottom. The oxidizer post recess length increases from the left to the right. A higher effect of the oxidizer-to-fuel ratio modification is evident for the circular combustor where a larger dispersion is noticeable, notably for the *R0* and *R12* injector configurations. It is recalled that a higher uncertainty of measurement around the mean is also found for the round shape. A clear influence of the mixture ratio variation on the pressure decay along the combustion axis is confirmed, as previously stated. A lower scattering of the normalized pressure to the wall distribution is noticeable for the rectangular combustion chamber, where a more evident increase on the pressure drop in the near-injector region can be detected by increasing the recess length. In addition, a significant variation of the normalized pressure trend gradient along the axis is reported to arise. Indeed, while a downward concavity appears for the reference injector configuration, a gradual tendency toward upward concavities is reported to affect the pressure distribution over the combustion axis as the recess length is increased.

Round combustion chamber

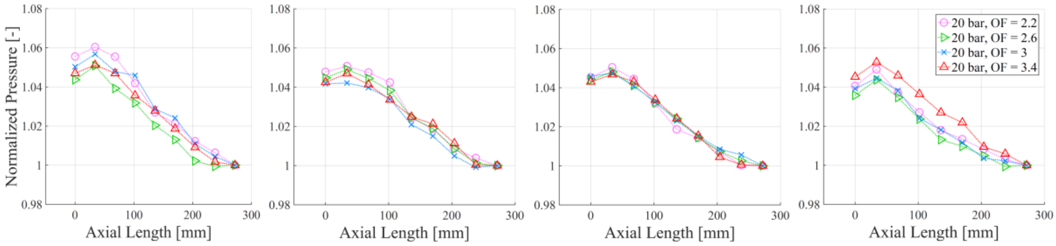

(a) *R0* **(b)** *R6* **(c)** *R9* **(d)** *R12*

Rectangular combustion chamber

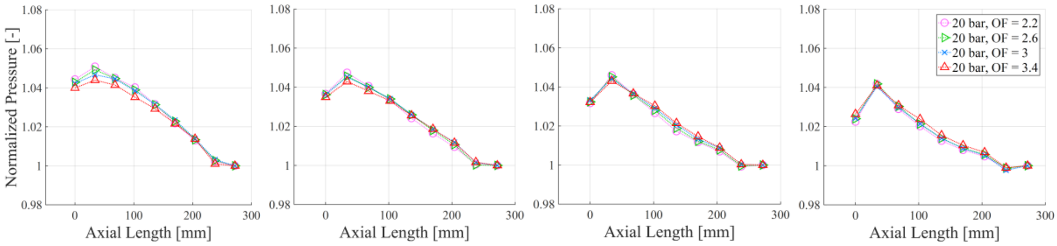

(a) *R0* **(b)** *R9* **(c)** *R12* **(d)** *R15*

Fig. 19. Normalized pressure distribution along combustion chamber axis – O/F comparison

The use of recess is reported to improve the initial mixing of propellants for both the combustion chamber arrangements. The longer the recess the higher the enhancement of mixing even though the effect is mostly confined in the near injection region for the lower recess lengths while engages the whole combustion process for the higher recessed configurations. Mixture ratio is also reported to affect the mixing process, mostly for the round hardware, where the impact of recess length is saturated for O/F equals to 3.4. Indeed, a lower mixture ratio can be related to a higher momentum flux ratio, as shown in *Fig. 15.a*, so enhancing mixing and combustion process, even though J is not significantly affected by recess for the round combustion assembly. An influence on pressure distribution due to the introduction of a recessed region is also visible in the rectangular combustion chamber. As previously mentioned, pressure decay along the combustion chamber axis is not significantly affected by the oxidizer post recess for the higher mixture ratio case while a relevant effect is noticed for the lower one, where an increase in velocity ratio and momentum flux ratio is evaluated for the *R15* configuration, if compared to the other injector assemblies. Because the flame develops inside the recessed region, combustion products occupy a certain fraction of the available duct area, so fuel flow being accelerated and consequently velocity ratio and momentum flow ratio being augmented, as reported by Kendrick et al. [18] for LO_X/GH_2 combination. This behaviour is herein mostly encountered for O/F 2.2 and *R15* recess length. Moreover, for higher momentum flux ratios methane mixing layer becomes more dynamic, downstream vortices being strengthened and mixing being enhanced. A more evident flattening of the pressure trend along the chamber axis is found for the rectangular other than the round shape. Indeed, a variation on the pressure decay shape is visible for both the oxidizer-to-fuel ratios in the former case, only for O/F 2.2 in the latter.

4.1.2 Injector pressure drop

An injector pressure drop increment is expected when a flame is anchored to a recessed oxidizer post, because of the blockage due to the combustion products inside the recessed region. The said increase is reported to highly affect methane side, because of the less capability in contrasting flame growing inside the recessed area due to the lower methane density, if compared to oxygen. A larger injector pressure drop increment is expected for higher mixture ratios than for lower O/F values because of the reduction of methane across the injector. Two non-dimensional coefficients, K_O and K_M, have been defined to investigate the increase in pressure drop at the injector due to a recessed oxidizer tube [23]. Different injection conditions are taken into account by means of normalization to the actual mass flow rate, as defined in *Eq. 4.3* and *Eq. 4.4* for oxygen and methane side, respectively. $\Delta P \doteq P_{dome} - P_C$ is defined as the pressure loss across the injector. Pressure drop coefficients for all the recessed injector configurations are outlined in *Fig. 20* and *Fig. 21,* for the round combustor chamber, on the left, and rectangular one, on the right. A significant repeatability for both the round and the rectangular hardware operative conditions and injector geometries is achieved. The higher the oxygen mass flow rate the higher the

$$K_O = \frac{\left(\frac{\Delta P_{GOX}}{\dot{m}_{GOX}^2}\right)_{Recess} - \left(\frac{\Delta P_{GOX}}{\dot{m}_{GOX}^2}\right)_{R0}}{\left(\frac{\Delta P_{GOX}}{\dot{m}_{GOX}^2}\right)_{R0}} \tag{4.3}$$

$$K_M = \frac{\left(\frac{\Delta P_{GCH4}}{\dot{m}_{GCH4}^2}\right)_{Recess} - \left(\frac{\Delta P_{GCH4}}{\dot{m}_{GCH4}^2}\right)_{R0}}{\left(\frac{\Delta P_{CH4}}{\dot{m}_{GCH4}^2}\right)_{R0}} \tag{4.4}$$

suction effect in methane side, Silvestri et al. [23] reported for the circular combustor chamber arrangement. A certain compensation is granted because of the expansion tendency of the flame inside the recessed region, so a certain length being necessary to the flow to interact. Therefore, a substantial plateau in both oxygen and methane injector pressure drop coefficients has been observed for the *R6* configuration, because of the compensation of the mentioned phenomena. The higher the recess the larger the expansion capability of the flame, a significant increase in K_O and K_M being visible, then. A maximum increase in the pressure drop coefficient of about 60% is seen for the *R12* configuration along the methane side, if compared to the *R0* assembly. An overall increment of about 10% and 30% is found for oxygen and methane coefficients, respectively, comparing the 12 mm and 9 mm recess lengths.

A similar behaviour is noticeable for the rectangular chamber for both oxygen and methane sides. While the *R9* configuration experiences a substantial superposition of the data if compared to the round hardware, the injector pressure drop for the *R12* injector case shows a slight reduction, same mixture ratio being considered. A 30% rise on the oxygen side pressure drop coefficient is found for the *R15* configuration if compared to the *R12* assembly in the rectangular hardware, approximately. A general plateau at the higher mixture ratios is observed for the methane case for the *R12* and *R15* injector assemblies in the rectangular combustor, possibly due to the achieving of the maximum flame expansion inside the recessed area for the considered recess

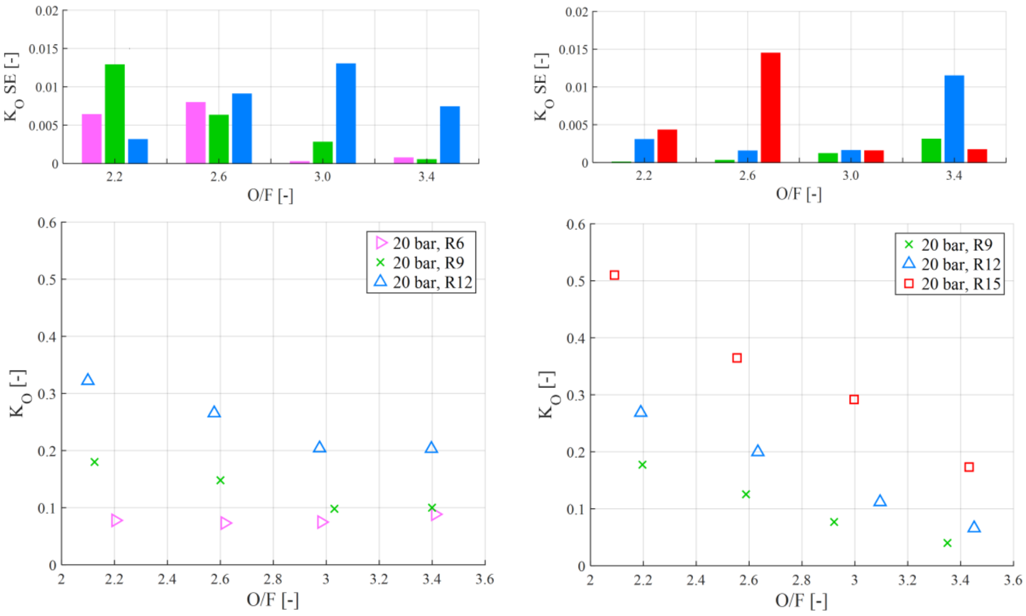

(a) Round combustion chamber **(b)** Rectangular combustion chamber

Fig. 20. Oxygen injector pressure drop coefficient over mixture ratio

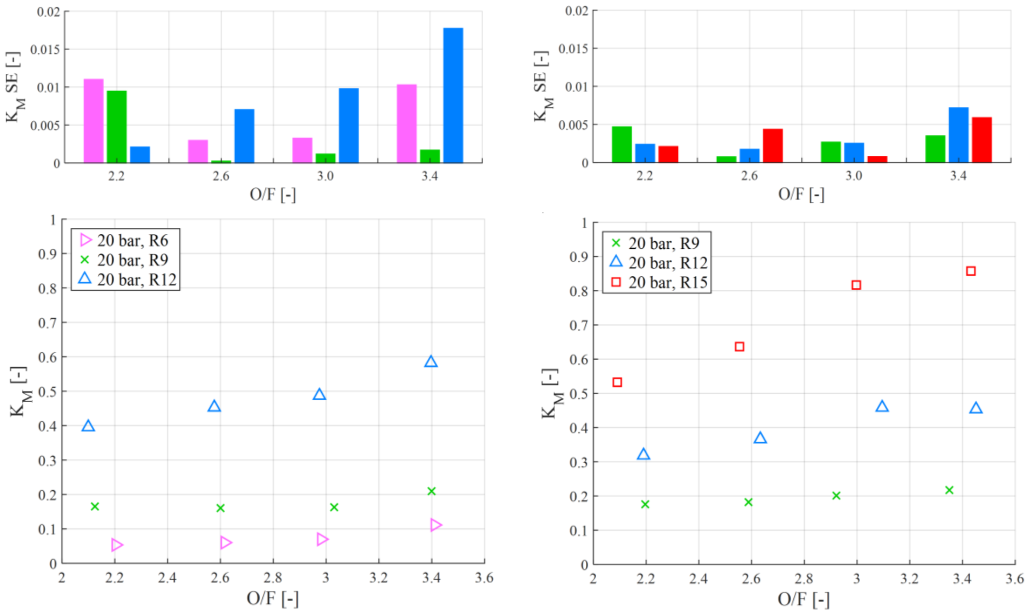

(a) Round combustion chamber **(b)** Rectangular combustion chamber

Fig. 21. Methane injector pressure drop coefficient over mixture ratio

length, K_M showing a flattening tendency for mixture ratios 3.0 and 3.4. Nevertheless, methane side injector pressure drop for higher mixture ratio values, which means lower momentum flux ratios, is reported to being slightly more affected by a recessed injector region than for the lower mixture ratios. This behaviour has been encountered by Lux et al. [21] in a liquid oxygen/liquid methane-based combustor where a recessed LO_X tube led to a much larger pressure loss on the methane side for the low momentum flux ratio values. On the contrary, an increase in momentum flux ratio above a critical threshold has been detected to possibly turn around the injector pressure drop trend, so that the pressure loss is found to be smaller with a recessed LO_X post than with a non-recessed one. Indeed, the momentum flux ratio is reported to influence the oxidizer and fuel discharge coefficients of a recessed coaxial injector element, as can be appreciated further in *Chapter 4, Paragraph 4.1*. It is worthwhile to underline, however, how the variation of the momentum flux ratio evaluated in the present study is way lower than the one obtained in the mentioned study case.

A lightly higher dependency on oxidizer-to-fuel ratio variation is observed for the rectangular combustion chamber setup other than the round one for all the recess lengths investigated, as reported in *Fig. 22* and *Fig. 23*. This tendency is particularly evident for the oxygen side, where the variation of the O/F is reported to affect the injector pressure drop at the higher recess lengths. In this case, the longer the recess the stronger the influence of the oxidizer-to-fuel ratio variation on the injector pressure drop coefficient. In fact, the lower amount of oxygen in the recessed region implies less capability to contrast the spreading of the triggered flame inside the recessed zone. Consequently, a stronger injector pressure drop coefficient arises.

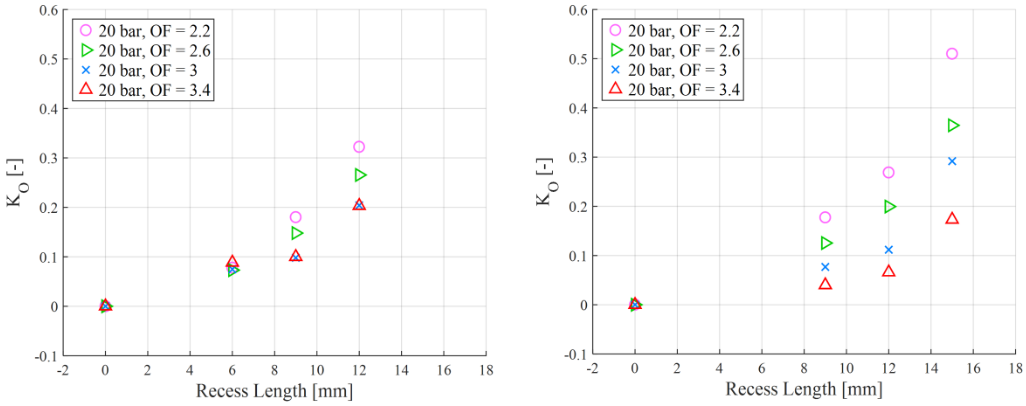

(a) Round combustion chamber **(b)** Rectangular combustion chamber

Fig. 22. Oxygen injector pressure drop coefficient over recess length

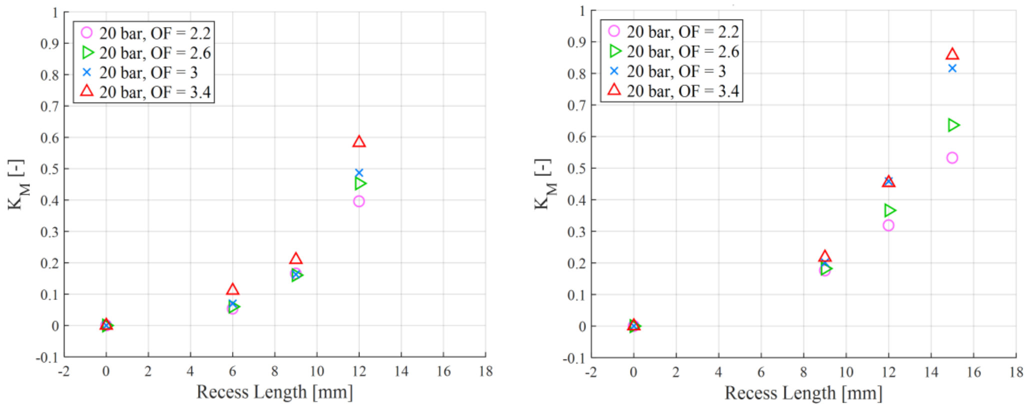

(a) Round combustion chamber

(b) Rectangular combustion chamber

Fig. 23. Methane injector pressure drop coefficient over recess length

4.2 Temperature distribution

4.2.1 Temperature distribution along combustion chamber axis

Temperature distribution over combustion chamber axis for the round and the rectangular hardware is discussed. Type *K* thermocouples at 1 mm from the hot gas wall are considered for the evaluation. Due to the steady combustion process, temperature profile is expected to increase along the combustor axis. A flatten of the temperature trend might be associated to the accomplishment of the combustion process, as already seen for the pressure distribution along the combustion chamber axis. Temperature distribution at different time steps for all the recess lengths investigated is depicted in *Fig. 24,* for mixture ratio 3.4 and nominal combustion chamber pressure of 20 bar, circular combustion chamber case on the top, rectangular combustion chamber case on the bottom. In particular, 1/6, 1/3 and 1/2 of the burning time are chosen, approximately corresponding to 0.5s, 1s and 1.5s after ignition. In addition, temperature profile at the evaluation time is presented, about 2s after the initiation of the flame. Good agreement between repetition tests for repeatability is found, so results for both runs at same operative and setup conditions are reported for legibility purposes. An overall increment in temperature is found for both the round and rectangular hardware. The higher the recess the larger the temperature experiences on the material wall, each time step being considered. Silvestri et al. [23] showed for the round assembly how the initial footprint due to the energy release produced by the

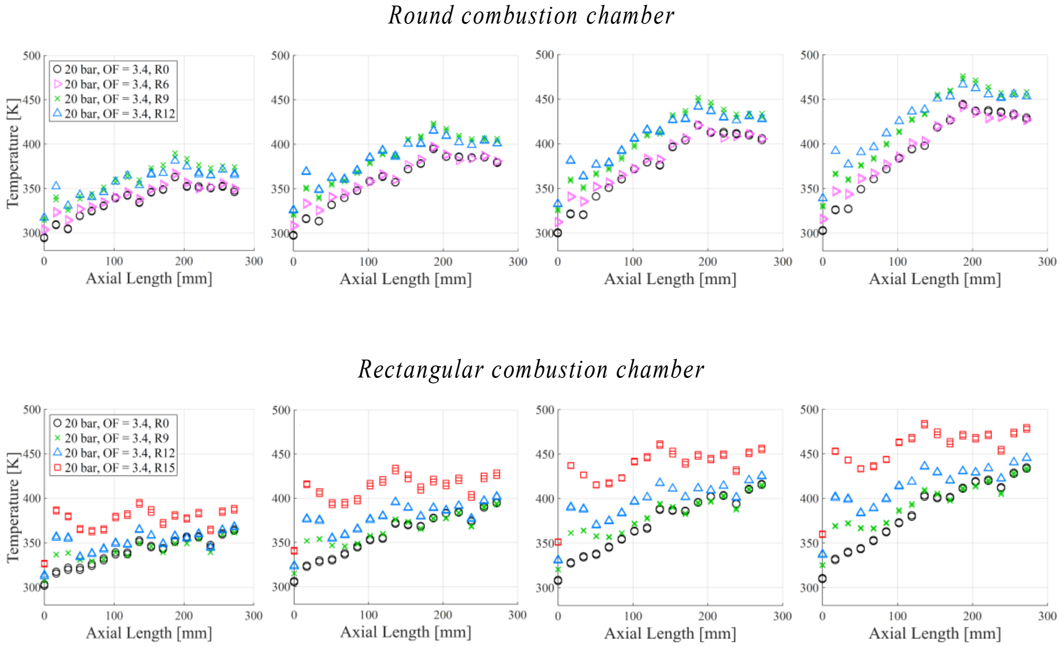

(a) t = 0.5s **(b)** t = 1s **(c)** t = 1.5s **(d)** t = 2s

Fig. 24. Temperature distribution along combustor chamber axis each 0.5s

ignition process and the interference of the igniter stream with the main flow tend to influence the temperature profile for the duration of the whole combustion process. To dissipate the initial heterogeneity it is necessary a time that exceeds the combustion time. A non-homogeneous temperature distribution is seen, due to the absorption of the initial energy released in the ignition process by the copper wall of the combustor. The same behaviour is found for the rectangular combustion chamber geometry. A peak in the temperature trend is clearly visible in the near-injector region for all the analysed discrete time instants, not being dissipated over the combustion time. Higher temperature peaks are produced increasing post recess lengths. A substantial superposition of the temperature profiles for the two combustors is noticeable in the first segment of the hardware, same recesses being considered. A slightly increase of temperature readings is found in the circular assembly, in the second segment. Temperature difference between the time instants analysed is evaluated for all the recesses tested in order to isolate the ignition influence on temperature measurements due to the capacitive nature of the combustors. *Fig. 25* depicts temperature difference profiles for each time interval, the round assembly being presented in the top, the rectangular in the bottom. A clear impact of the ignition process is herein observed for the first time interval, while temperature gradient is flattened after 1/6 of the burning time. This behaviour is observed for both the round and rectangular geometries, even though the ignition footprint tends to lightly persist in the latter for the *R15* configuration where a maximum temperature peak in the near-injector region is reached, more than 70% higher than the flush-mounted configuration. A slightly higher recess influence for the square combustion geometry is also found.

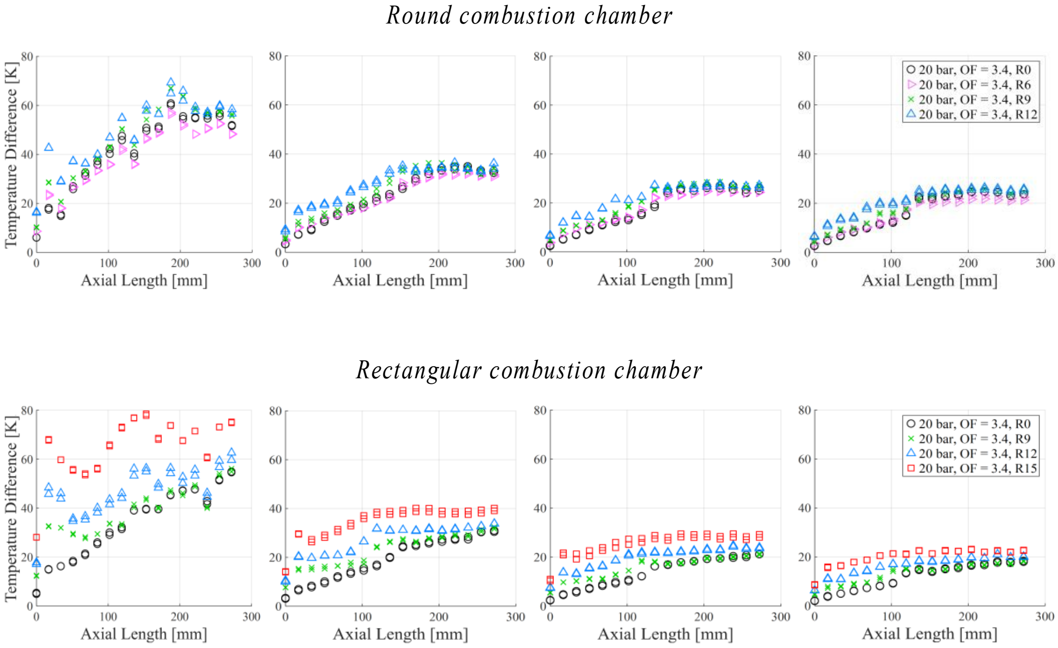
Round combustion chamber

Rectangular combustion chamber

(a) Δt = [0.5-0]s **(b)** Δt = [1-0.5]s **(c)** Δt = [1.5-1]s **(d)** Δt = [2-1.5]s

Fig. 25. Temperature difference distribution along combustor chamber axis each 0.5s

Hence, temperature difference between the evaluation time and an initial time of 1/6 of the hot run after the ignition (~ *0.5s*) is considered and shown in *Fig. 26*. Indeed, a certain smoothing of the initial igniter footprint has been detected below these conditions. Results for mixture ratio 3.4 are illustrated, round hardware on the left, rectangular one on the right. An overall flattening in the temperature profiles is found in the second segment for both the hardware. A continuous increase is seen in the first segment, each recess length being considered. An almost constant slope is encountered for the circular geometry varying inner tube recess and proceeding along the combustor axis, a different behaviour being noticeable for the rectangular geometry. Indeed, while the reference injector case experiences a continuous increment in temperature difference, a steeper slope in temperature profile is clear increasing recess. The higher the recess length the more rapid the flattening of the temperature trend, combustion end being achieved closer to the injector face-plate. A plateau of the temperature readings is achieved about 75 mm away from the injector plane for the *R15* injector configuration. This could be due to a better initial mixing of the propellants inside the recessed region, as already mentioned for the normalized pressure analysis. Moreover, slightly higher temperature values are reached right next to the injector plane for the rectangular combustor, possibly due to the presence of corner vortices affecting the recirculation region.

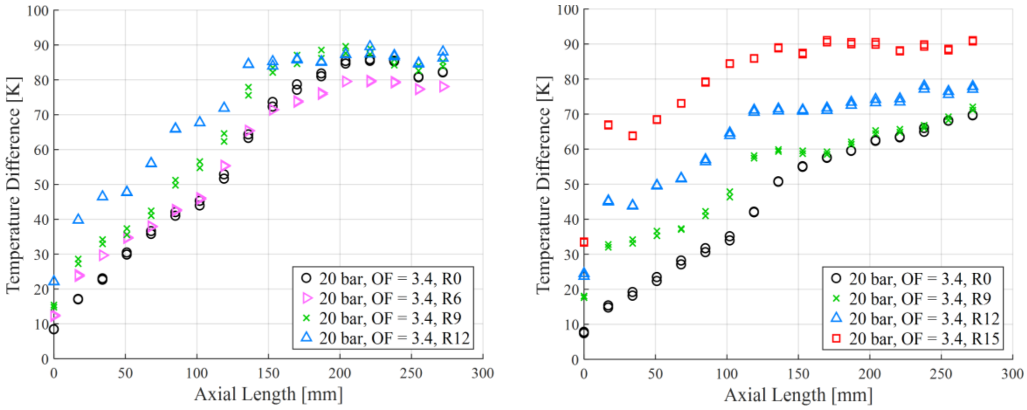

(a) Round combustion chamber **(b)** Rectangular combustion chamber

Fig. 26. Temperature difference distribution along combustor chamber axis at evaluation time – Recess comparison

An influence on temperature distribution is found due the oxidizer-to-fuel ratio and depending on injector configuration, as depicted in *Fig. 27*. Round combustion chamber case is reported on the top, rectangular one on the bottom, oxidizer post recess length increasing from left to the right. O/F equals to 2.2, 2.6, 3.0 and 3.4 are considered. A substantial independency of the temperature profile to the mixture ratio is clearly visible in the first segment of both combustor configurations. Otherwise, a variation of the oxidizer-to-fuel ratio is reported to affect the aforementioned distribution in the second segment, both hardware assembly being considered. As expected, the higher the mixture ratio the more significant the temperature difference due to the larger equilibrium temperature. A 20 K gap is noticeable for the *R15* recess length in the rectangular setup between the highest and the lowest O/F values. If same recess lengths are considered, a slightly larger influence of mixture ratio modification is evident for the round geometry, except for the *R9* injector assembly where an O/F variation is reported not to alter the temperature profile throughout the round combustion chamber.

Round combustion chamber

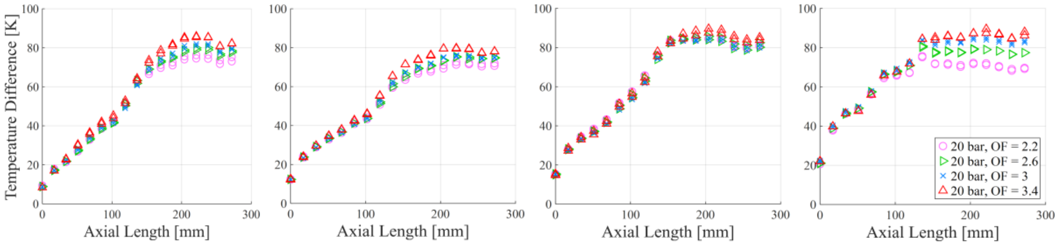

(a) *R0* **(b)** *R6* **(c)** *R9* **(d)** *R12*

Rectangular combustion chamber

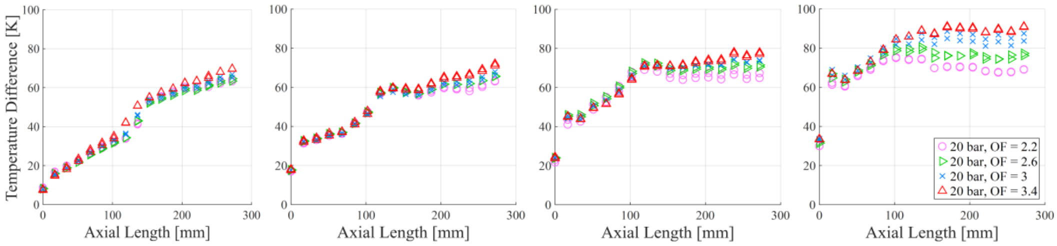

(a) *R0* **(b)** *R9* **(c)** *R12* **(d)** *R15*

Fig. 27. Temperature difference distribution along combustor chamber axis at evaluation time – O/F comparison

4.2.2 Temperature distribution over time

Temperature distribution over time for the circular and the rectangular hardware is investigated. Type *K* thermocouples at 1 mm from the hot gas wall are considered for the evaluation. Temperature difference between evaluation time and start-up conditions is outlined for both burning time and overall run time. The first four thermocouples from the injector plate are analysed, at *z = 0.5 mm*, z = *17.5 mm*, *z = 34.5 mm* and *z = 51.5 mm* along the combustor axis, to have an insight on the near-injector region. Temperature difference profile over burning time for mixture ratio equals to 3.4 and nominal combustion chamber pressure of 20 bar is depicted in *Fig. 28*, the round geometry on the top, the square one on the bottom. An increment of the slope of the temperature profile is found in the rectangular combustion chamber increasing the recess length, has already seen in the round combustor by Silvestri et al. [23]. This has been related to a better initial mixing in the near-injector area. The higher the heat release, the higher the temperature gradient in the wall material. A significant consistency to what previously stated is found for the rectangular hardware. A further increase of the recess length to 15 mm shows an additional increment of the slope in the temperature profile in the near-injector area. An influence of the impact of the flame to the wall material was also assumed for the circular combustor chamber configuration, boundary layer being destabilised and a more intense flame producing larger temperature values. The same behaviour is detectable for the rectangular assembly where a maximum variation of the temperature gradient is encountered for the thermocouples at *z = 17.5 mm*, where the stagnation point occurs [36]. Similar trends are measured for all the mixture ratios tested.

Round combustion chamber

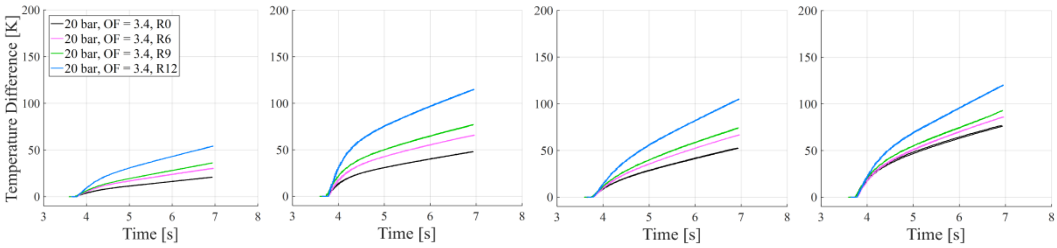

Rectangular combustion chamber

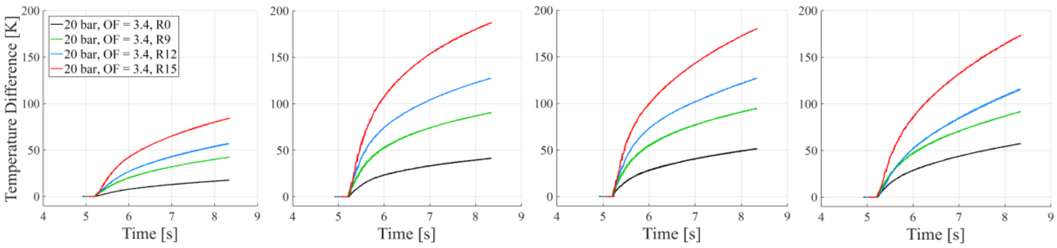

(a) z = 0.5 mm **(b)** z = 17.5 mm **(c)** z = 34.5 mm **(d)** z = 51.5 mm

Fig. 28. Temperature difference distribution over burning time – O/F = 3.4

While a considerable agreement on data is found for the temperature distribution over burning time, a distinct trend arises if overall run time on the two hardware geometry is considered. Temperature difference between evaluation time and start-up time is reported in *Fig. 29* for the first four thermocouples from the injection plane. In addition, to allow better comparability between the hardware shapes, *Fig. 30* depicts a comparison of the temperature trends for the first two thermocouples along the combustor axis for two of the three common recess lengths tested, *R0* and *R12*, the solid line representing the square assembly, the dashed line the circular assembly.

Round combustion chamber

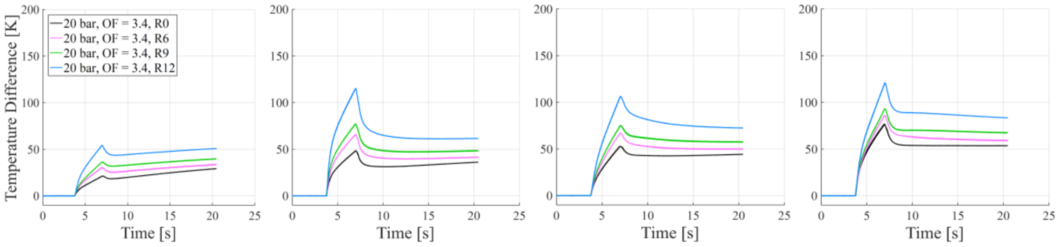

Rectangular combustion chamber

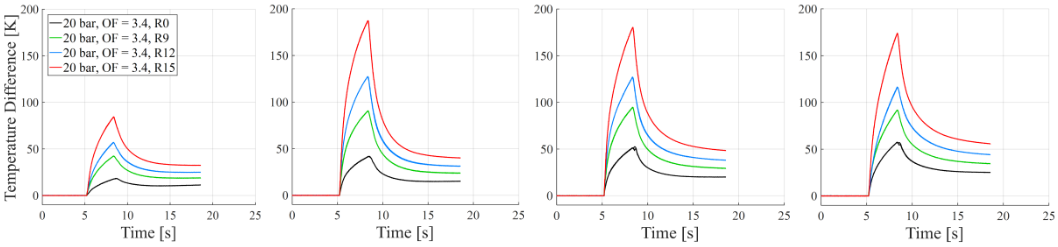

(a) z = 0.5 mm **(b)** z = 17.5 mm **(c)** z = 34.5 mm **(d)** z = 51.5 mm

Fig. 29. Temperature difference distribution over overall run time – Recess comparison

At the start-up, the temperature distribution is dependent solely on the internal combustion chamber surface available. After a certain time, the heat wave having reached the external wall material, different slopes in the temperature profiles are experienced. If the *R0* post recess length is considered, a decrease in the temperature gradient for the rectangular hardware, is found for both the temperature signals analysed, as already shown in Silvestri et al. [40]. This has been associated to the different mass of the two combustors, due to the different thickness of the hardware walls. Indeed, the square combustion chamber is almost two times heavier than the circular one, same material being considered, so the temperature slope is faster diminished after the temperature signal reaches the external walls. A similar behaviour influences the shut-down trend, where a faster decrease is found for the rectangular geometry after the combustion process. A slightly increase of the

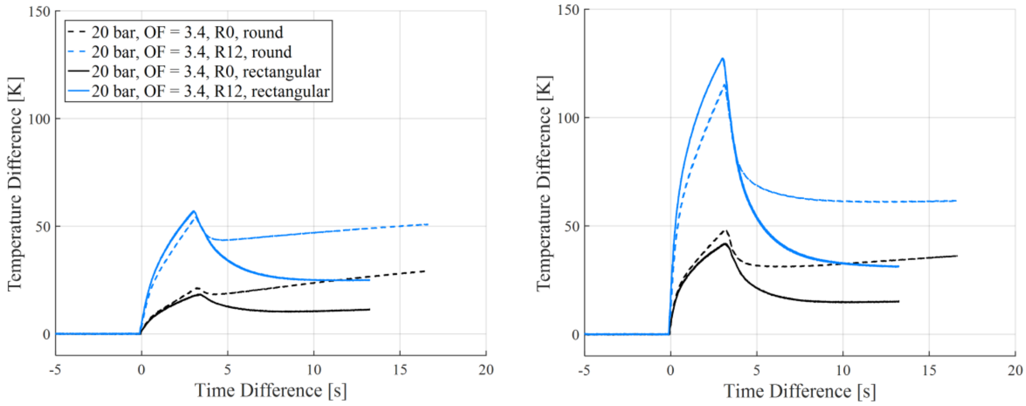

(a) z = 0.5 mm **(b)** z = 17.5 mm

Fig. 30. Temperature difference distribution over overall run time – Combustor comparison

temperature readings at the injector plate (*z = 0.5 mm*) is found for the round combustor even after the end of the combustion reaction. When the oxidizer post is recessed a different distribution over time is noticeable. While for the shut-down phase a steeper decrement is visible for the temperature profile in the rectangular case, as previously reported, an overall increment of the temperature gradient is now seen during the hot run, if compared to the circular geometry. A higher gap is found if the second thermocouple signal is considered. This could be due to a different modification of the recirculation zone induced by a recessed injector configuration for the two inner cross-section geometries. Indeed, while a similar recirculation is encountered in the two combustor shapes for the reference injector case, a relative strengthening is visible for the *R12* configuration in the square arrangement, as pointed out in Fig. *18* for the normalized pressure distribution along the combustion chamber axis. Corner effects on boundary layer dynamics and heat flux profile should be also taken into account.

4.3 Heat flux distribution

An overview of the heat flux distribution on the inner combustion chamber walls along the combustor axis is outlined. The capacitive nature of the hardware only allows to reconstruct heat flux profile by means of the experimental temperature readings. An inverse computational method [33-34] is adopted to reconstruct heat flux characteristics from temperature measurements by means of an iterative inverse regularization method to minimize the residual between calculated and measured temperature values. Heat diffusion PDEs are solved by referring to the solution of a direct problem, i.e. computing temperature for each discrete spatial coordinate of the 3D control domain and time step. In this respect, a Finite Difference method is adopted, boundary conditions being represented by the unknown heat flux in the wall material. Thermocouple readings are used as initialization values for the temperature domain. A default initial guess is taken for heat flux. The direct problem is solved at each time step updating the time-dependent boundary heat flux conditions computed in the previous iteration. A 3D control volume, cylindrical for the round combustor, cave square prismatic for the rectangular one, is modelled taking into account only the combustor chamber itself, from the injector face-plate to the axial coordinate where the nozzle begins, since no information can be inferred due to the lack of sensors in the nozzle segment. The heterogeneity in the material due to the presence of the quartz glass window in the rectangular hardware is neglected. To this end, an adiabatic assumption for the optical access material is adopted, leading to an acceptable evaluation of the integrated heat flux due to the small dimension of the quartz glass window and the distance from the thermocouple housings. A correction of the heat flux is introduced, taking into consideration the variation in mass flow rate

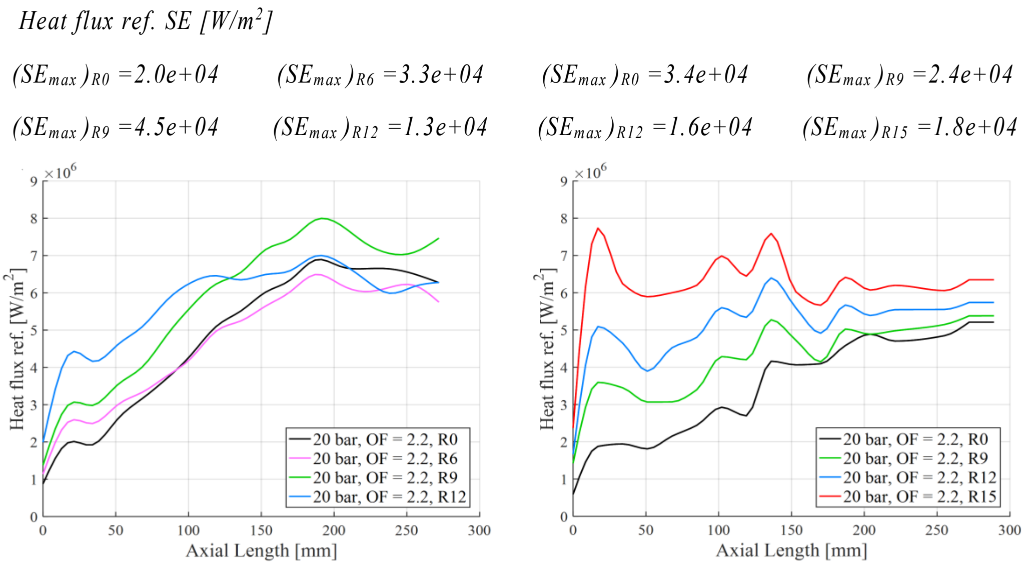

(a) Round combustion chamber **(b)** Rectangular combustion chamber

Fig. 31. Heat flux distribution along combustion chamber axis – O/F = 2.2

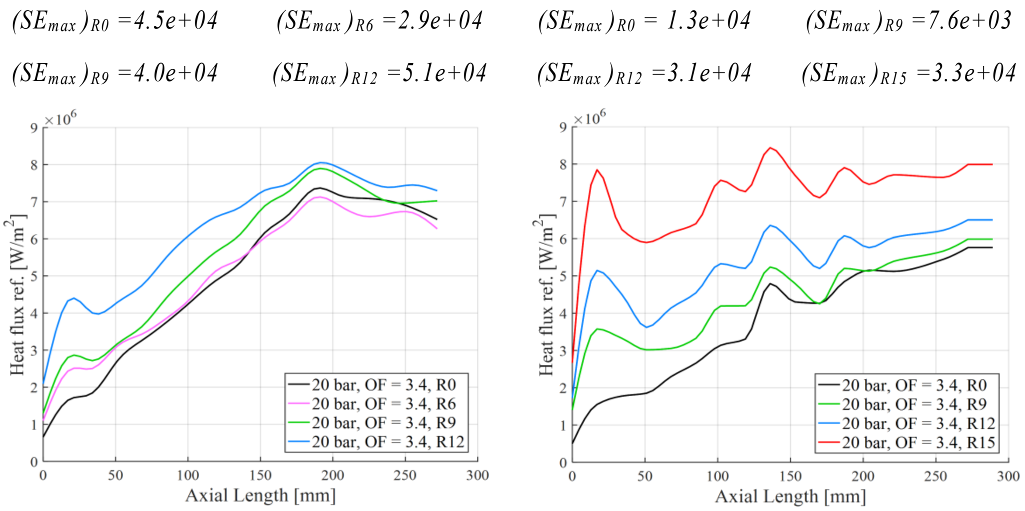

(a) Round combustion chamber **(b)** Rectangular combustion chamber

Fig. 32. Heat flux distribution along combustion chamber axis – O/F = 3.4

for different tests. Bartz reported [35] how the heat transfer coefficient is proportional to the mean combustion pressure to the power of 0.8. A correlation accounting for partial and total mass flow rates is applied, as described in *Eq. 3.1*, to decouple the contribution on the combustion pressure due to different mixing efficiency [23].
Wall heat flux axial distribution for mixture ratios 2.2 and 3.4 and all injector configurations tested is depicted in *Fig. 31* and *Fig. 32*, respectively, circular combustion chamber on the left, rectangular one on the right. Repetition tests averaged values are depicted. A significant agreement is obtained, maximum standard error of the mean being reported for each injector configuration.

Heat flux profile increases continuously along the combustor chamber axis due to the steady combustion process, as already seen for the temperature distribution. A plateau of the trend can be associated to the end of the reaction process. An increment of the heat flux in the near injector region of the circular combustor has been shown increasing the recess length by Silvestri et al. [23]. The 12 mm recess is found to exhibit a higher heat flux value as well a different profile shape. Moreover, a substantial independency to the mixture ratio has been detected in the first segment of the hardware. Indeed, the initial mixing of the propellants is the dominating factor in the near-injector zone, so heat loads being determined by the growth rate of the boundary layer and the amount of propellant burnt. Thus, a variation of the mixture ratio, hence a variation of the amount of oxygen injected, is not affecting the global heat flux distribution. A similar mechanism affects heat flux profiles in the first part of the rectangular hardware, even though a different trend shape can be seen. While oxidizer-to-fuel ratio seems not to influence heat flux values, a high peak is visible right downstream the injector plate. The higher the recess length, the larger the heat flux level. A similar behaviour is noticeable comparing the *R9* and *R12* injector configuration, heat flux trend increasing after the initial peak and achieving a plateau in the second part of the combustor, where the combustion process ends. A further increase in recess length to 15 mm produces an increment of the heat flux, moving upstream the end of the reaction process, as can be inferred by the flattening of the evaluated profile in the first segment of the combustion process. An influence of the mixture ratio is found in the second part of the combustor for both the hardware geometries, as shown in *Fig. 33*. As already reported in the circular assembly analysis, the combustion process represents the dominating mechanism influencing heat flux

Round combustion chamber

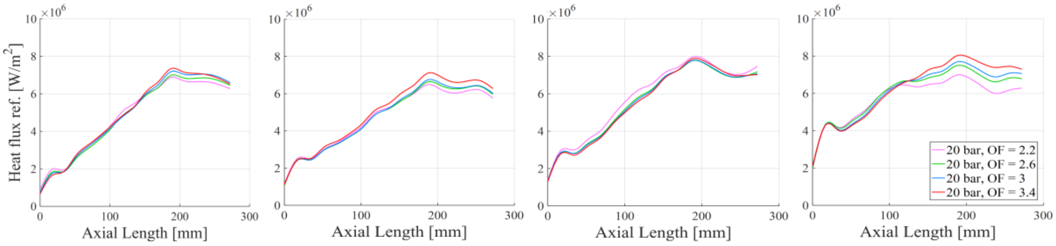

(a) *R0* **(b)** *R6* **(c)** *R9* **(d)** *R12*

Rectangular combustion chamber

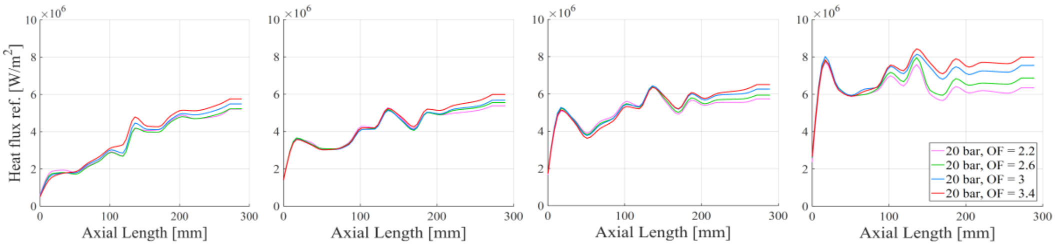

(a) *R0* **(b)** *R9* **(c)** *R12* **(d)** *R15*

Fig. 33. Heat flux distribution along combustion chamber axis – O/F comparison

transfer in the second part of the combustor, so a higher amount of oxidizer affecting temperature. An identical behaviour has been already pointed out for the temperature distribution along the combustion chamber axis, as depicted in *Fig. 27*, so being noticeable for the heat flux profile, too. A bumping tendency, typical of a capacitive hardware, can be found in both temperature and heat flux trends because of the heat flux evaluation from the experimental temperature readings. Higher mixture ratios are reported to generate larger heat fluxes at the end of the combustion chamber for both round and rectangular geometries. Rectangular hardware being considered, a different profile evolution is also noticeable for the different mixture ratios. A global levelling out of the heat flux can be seen for the lower oxidizer-to-fuel ratios at the end of the combustion chamber for all the injector configurations, while a growth tendency is still present for the higher mixture ratios. As concerns the circular chamber assembly, an overall agreement of heat flux trends is visible for all the recess lengths and O/F 3.4 while a different tendency is experienced by the *R12* configuration than the other recess lengths for mixture ratio equals to 2.2. Indeed, a lower heat flux than the 9 mm recess lengths is reached for the *R12* assembly in the second segment of the chamber, the major part of the combustion process being achieved in the first half. A faster development of the thermal boundary layer is promoted, so diminishing the maximum level of heat flux, also due to a shifting of the global heat release in the upstream region [23].

A direct comparison between the higher and the lower common injector configurations for the two hardware is depicted in *Fig. 34*, O/F 2.2 on the left, 3.4 on the right. The solid line is representative of the rectangular combustor, the dashed line of the circular one. A slightly lower heat flux value is calculated for the square

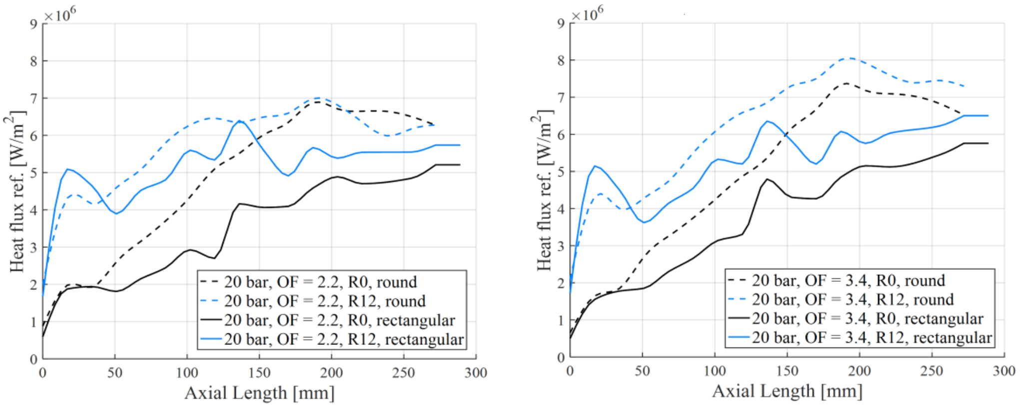

(a) O/F = 2.2

(b) O/F = 3.4

Fig. 34. Heat flux distribution along combustion chamber axis – Combustion chamber comparison

combustion chamber other than the round one except for the near-injector region, same mixture ratio and injector configuration being compared. In the second half of the chamber, the recessed injector assembly for the rectangular hardware is found to experience heat flux levels lower than the non-recessed case for the round hardware. As already assumed in a previous combustion chamber geometry comparison [40] for a flush-mounted injector configuration, the lower heat flux values encountered for the square shape could be due to a lower mixing efficiency because of the presence of the corners that can induce different recirculation dynamics and grant a higher volume triggering the strengthening of vortices close to the injector plate. This assumption is reflected in the recessed injector analysis. Heterogeneity of the heat flux distribution in the circumferential direction could also affect the computation and should be taken into account for the square arrangement.

Heat rate values, obtained by integrating the heat flux distribution over the combustion chamber surface are depicted in *Fig. 35*. Adiabatic quartz glass window assumption has been considered. Averaged values between repetition tests are reported, results being statistically overlapping, a maximum standard error of the mean about *600 W* being found for the rectangular combustion chamber, O/F 3.4 and *R12* assembly, about *500 W* for the circular one, O/F 2.2 and *R6* injector assembly.

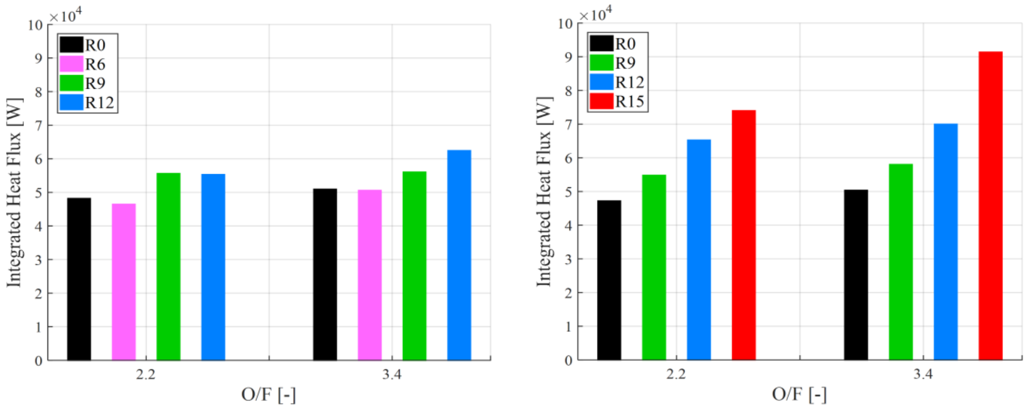

(a) Round combustion chamber **(b)** Rectangular combustion chamber

Fig. 35. Integrated heat flux

A continuous increment of the integrated heat flux is found for the rectangular chamber geometry as the recess length is increased, slightly larger values being found for mixture ratio equals to 3.4. A significant rise is noticeable for the *R15* injector configuration for the higher oxidizer-to-fuel ratio where a heat rate of about *90 kW* is computed, 25% higher than the 12 mm recess length, approximately. As already pointed out, a lower influence due to recess and mixture ratio is found for the circular combustion chamber. No significant differences are reported comparing same recess lengths for the two chamber geometries except for the *R12* injector assembly where a 10-15% increment is visible in the rectangular hardware for both oxidizer-to-fuel ratios.

To summarize, a recessed injector configuration is found to enhance the mixing in the near-injector region, so promoting the rise of heat flux to the wall right downstream the injector plane. A certain recess length is required to influence heat loads in the second part of the combustion chamber, so affecting the whole combustion process. A stronger influence due to recess and mixture ratio variation is evaluated for the rectangular combustor. To this end the influence of the corners on the near-injector recirculation zone as well as non-homogeneity on the heat flux distribution in the circumferential direction should be taken into account for the rectangular configuration assembly.

4.4 Performance coefficients

An overview of the main performance parameters describing the injector behaviour and characteristics is given in the following. In particular, injector orifices discharge coefficients and combustion efficiency are presented and discussed for different oxidizer-to-fuel ratios and oxidizer post recess lengths for the two hardware arrangements.

4.4.1 Injector orifices discharge coefficient

The discharge coefficient – C_d – for both oxidizer and fuel injector orifices is calculated and depicted in *Fig. 36* and *Fig. 37*, respectively, for all the geometrical injector assemblies and oxidizer-to-fuel ratios tested. The circular combustion chamber is reported on the left, the rectangular combustion chamber on the right. The injection conditions are evaluated by means of the first pressure sensor inside the combustion chamber and the relative propellant manifold characteristics. The inner cross section area of the oxygen tube is used for the oxidizer side calculation, the outer annular gap cross section area for the methane side.

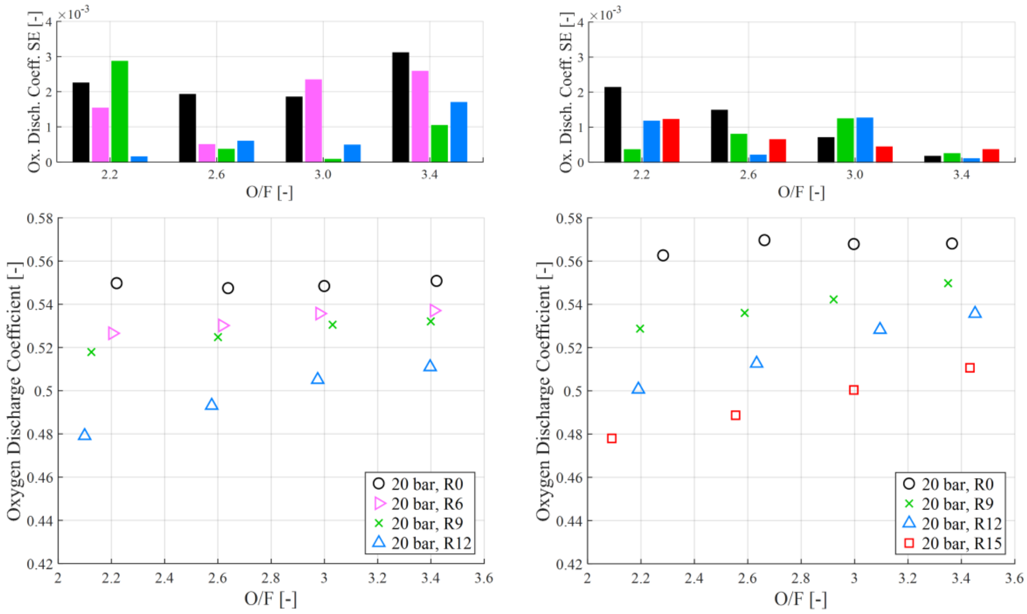

(a) Round combustion chamber **(b)** Rectangular combustion chamber

Fig. 36. Injector oxygen orifice discharge coefficient

Oxidizer post recess length is found to decrease oxygen discharge coefficient for both the circular and the square combustion chambers. The higher the recessed region, the larger the decrement in C_d. This is related to the injector pressure drop rise when a recess is adopted, as seen in *Fig. 20* and *Fig. 21*. Higher mixture ratios, then larger oxygen amount in the system, are found to cause smaller pressure drops on oxygen injector side because of the higher capability to contrast flame expansion, so an increase in the discharge coefficient is visible in both hardware if O/F is augmented. As already pointed out, a certain recess length is necessary for the flow inside the duct to interact, so the smallest recess injector configurations and the reference case are only slightly affected by oxidizer-to-fuel ratio variation. A dual behaviour is found for the methane-side discharge coefficient, where an increase of mixture ratio, then lower amount of methane in the system, is reported to cause a rise in the injector pressure drop. Same considerations can be inferred by the analysis of the velocity ratio for each operating point, VR decreasing for O/F increasing. A lightly higher discharge coefficient is calculated for the square combustion chamber other than the round one for both propellant lines. This could be due to different concurrent aspects. On the one hand, the scaling approach adopted for the comparison should be taken into account.

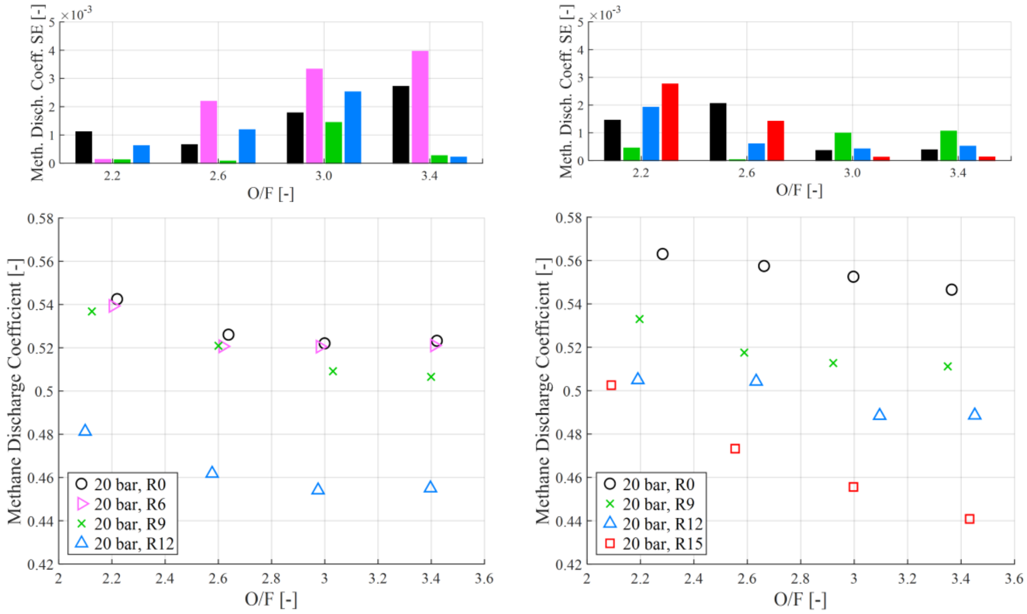

(a) Round combustion chamber **(b)** Rectangular combustion chamber

Fig. 37. Injector methane orifice discharge coefficient

Since mean combustion chamber pressure and oxidizer-to-fuel ratio values are kept constant when the same operating points are tested and compared, a certain variation in the mass flow rate injected is experienced for the two hardware arrangements, as can be inferred in *Fig. 6.a.* and *Fig.7.a.* Thus, a higher total mass flow rate is obtained for the rectangular combustion chamber shape. On the other hand, the different inner cross section of the two hardware could affect differently the recirculation zone in the near-injector region, because of the presence of the corners in the square combustion chamber, as already pointed out. Since the injector pressure drops across the injector orifices are calculated by means of the pressure reading of the first pressure transducer in the combustor, *0.5 mm* far from the injector plane, a different influence might be exerted. Indeed, when a square geometry is considered, large recirculation regions are established and occupy the corners area in the proximity of the injector inlet and the face-plate. Non-premixed flames and un-burnt fuel are captured and brought to the reaction zone behind the oxidizer post. Hence, a high-temperature recirculation zone might be established and affects the corners dynamics in the near injector region, flow instability possibly arising, then, and the downstream flame splitting [41].

In order to investigate the recess length influence on the decrease of the discharge coefficient compared to the flush-mounted injector configuration, a discharge coefficient factor is defined in *Eq. 4.5* and *Eq. 4.6* for oxygen and methane sides, respectively. Since a reduction in the discharge coefficient is expected when an oxidizer post recess length is considered, a negative value of the relative discharge coefficient is expected. The closer to zero the discharge coefficient factor, the lower the influence of the recess on the discharge coefficient compared to the reference injector configuration (*R0*).

$$K_O^{C_d} = \frac{\left(C_{d\,GOX}\right)_{Recess} - \left(C_{d\,GOX}\right)_{R0}}{\left(C_{d\,GOX}\right)_{R0}} \tag{4.5}$$

$$K_M^{Cd} = \frac{\left(C_{d\,GCH4}\right)_{Recess} - \left(C_{d\,GCH4}\right)_{R0}}{\left(C_{d\,GCH4}\right)_{R0}} \tag{4.6}$$

Discharge coefficient factors for oxygen and methane sides are shown in *Fig. 38* and *Fig. 39*, respectively, the circular combustion chamber on the left, the rectangular combustion chamber on the right. A stronger influence of the recess variation on the discharge coefficient is found for the rectangular hardware, generally. A substantial independency to the recess on C_d is found for the methane side in the circular combustion chamber for the 6 mm and 9 mm recess lengths. A comparable influence for the two hardware arrangements is reported for the *R12* configuration, for both oxidizer and fuel orifices, instead. As concerns the rectangular combustion chamber assembly, a recessed injector configuration affects the discharge coefficient for all the tested lengths. The higher the recess the larger the influence of the mixture ratio variation, especially for the methane side. Indeed, the effect of the highest recess length (*R15*) on the decrease of the methane discharge coefficient compared to the reference configuration is, for mixture ratio 3.4, about 40% higher than for mixture ratio 2.2.

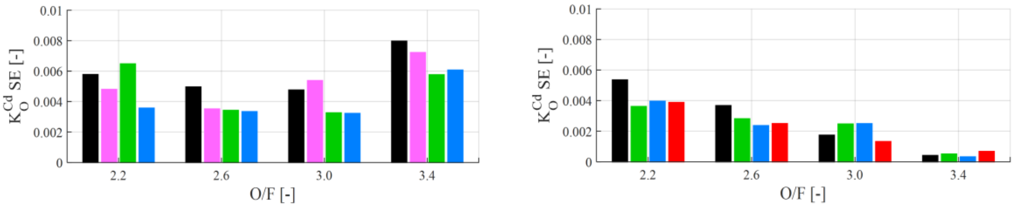

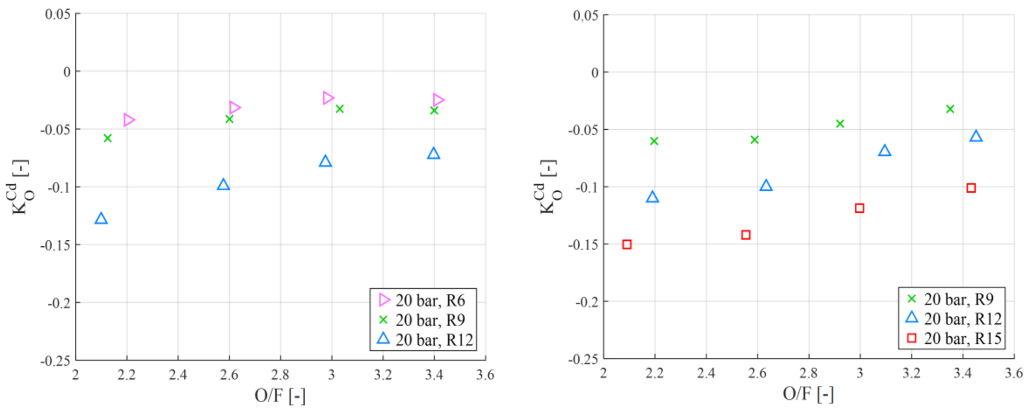

(a) Round combustion chamber **(b)** Rectangular combustion chamber

Fig. 38. Injector oxygen orifice discharge coefficient factor

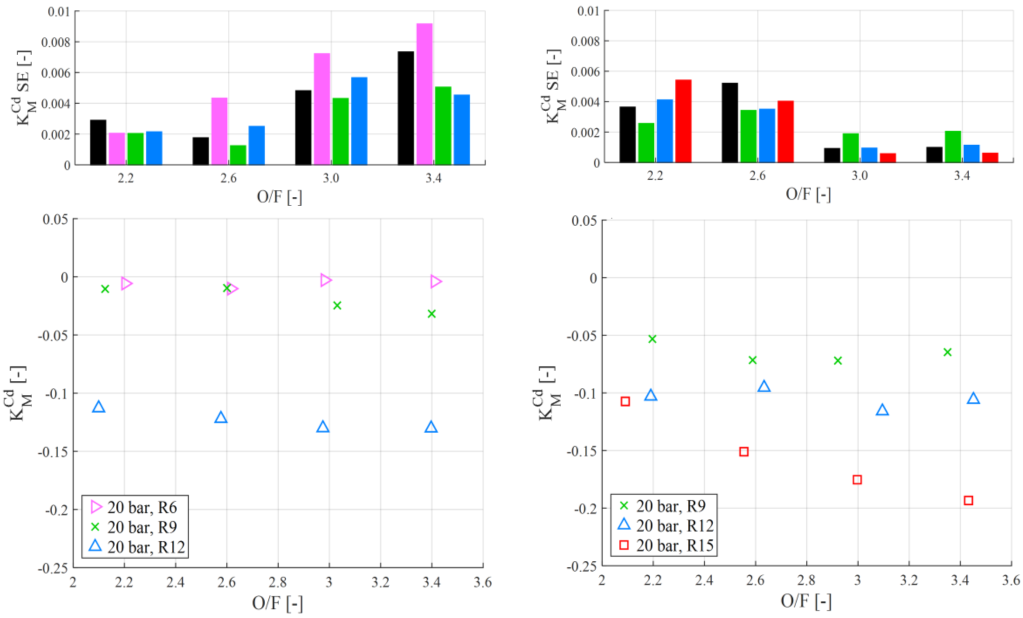

(a) Round combustion chamber **(b)** Rectangular combustion chamber

Fig. 39. Injector methane orifice discharge coefficient factor

To sum up, a recessed injector configuration promotes the decrease of the discharge coefficient, for both oxidizer and methane sides, because of the raise of the injector pressure drop due to the expansion of the flame inside the recessed region. The higher the recess, the lower the discharge coefficient for both round and rectangular configurations, even though a certain recess length is necessary for the flow to interact. A larger influence of recess length on discharge coefficient, if compared to the reference injector configuration, is found for the square combustion chamber, especially for the highest recess length analysed on methane side.

4.4.2 Combustion efficiency

Combustion efficiency for both round and rectangular combustion chambers for all the injector configuration assemblies and mixture ratios tested, is evaluated and discussed in the following. Combustion efficiency, defined as in *Eq. 3.2*, represents the effectiveness of the conversion of the chemical energy contained inside the fuel into heat thermal energy used in the combustion process and can be computed as the ratio of the experimental measured characteristic velocity to the theoretical ideal (complete combustion) characteristic velocity, where the latter has been computed with Gordon-McBride [38] *CEA* code. Two approaches are considered: a *thrust chamber* ($\eta_{c^*}^{TR}$) combustion efficiency and an injector related *energy release* ($\eta_{c^*}^{ER}$) combustion efficiency are evaluated. The former considers adiabatic wall conditions – consistently with CEA assumptions – the latter takes into account energy losses towards the combustor walls for inlet enthalpies correction. Vaporization and mixing efficiency are taken into account into the given definition, the one accounting for the presence of un-combusted propellant drops (in the case of liquid propellants), the other for incomplete mixing [42]. Losses due to two-dimensional and chemical kinetics effects as well as boundary layer displacement affecting the throat potential flow area are not included. In addition, frozen as well as shifting equilibrium approaches are considered, the two not inducing remarkable differences – lower than 0.1%, on average – on performance evaluation. Shifting equilibrium approach results are presented. Thrust chamber combustion efficiency and energy release combustion efficiency are reported in *Fig. 40* and *Fig. 41*, respectively. Averaged repetition test results are presented. An overview of the standard error of the mean between the same operating points is given for all the mixture ratios and injector recess lengths analysed. A significant agreement between repetition tests is found.

A substantial independency of the thrust chamber combustion efficiency from the 6 mm and 9 mm recess lengths was found in a previous study [23] for the round combustion chamber, regardless of mixture ratio. A notable increment has been reported for the *R12* configuration, instead, a rise of about 4% being visible for all oxidizer-to-fuel ratios. A different behaviour is encountered for the rectangular hardware where a gradual increase of the thrust chamber combustion efficiency is noticeable extending the oxidizer post recess length. A gain about 2%, 4% and 6% is experienced by the 9 mm, 12 mm and 15 mm recess length configuration, respectively, if compared to the flush-mounted injector arrangement. This can be correlated to a better initial mixing of the propellants inside the recessed and near-injector region.

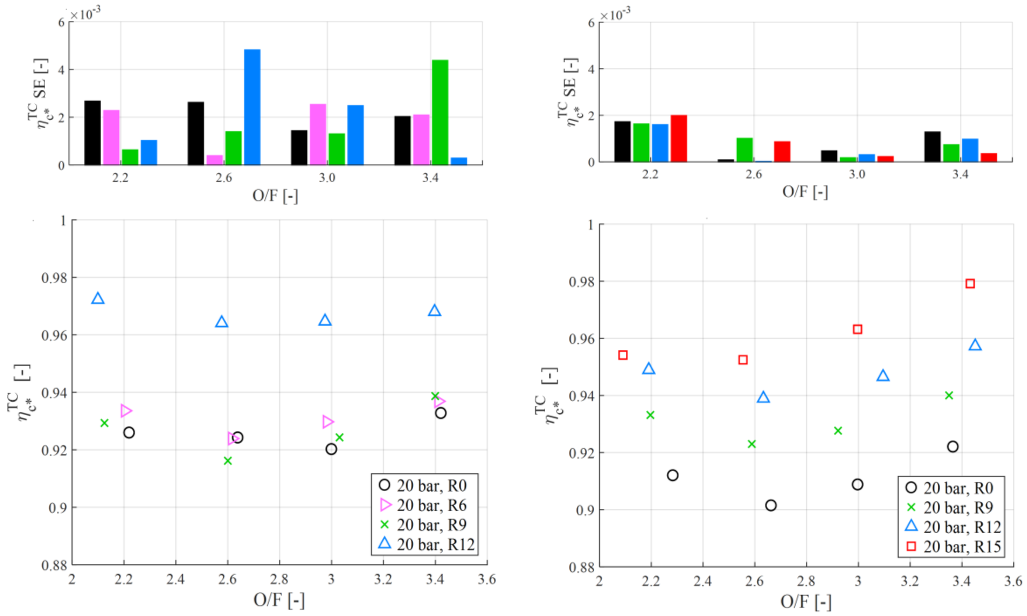

(a) Round combustion chamber **(b)** Rectangular combustion chamber

Fig. 40. Thrust chamber combustion efficiency

Higher values of the thrust chamber combustion efficiency are calculated for the circular hardware, *R0* recess length being considered already, if compared to the square geometry. The same trend found for the thrust chamber combustion efficiency is calculated for the injector related energy release combustion efficiency. Values for the combustion efficiency higher than the unit are visible for both the circular and the square combustion chamber. This could be due [23] to the neglection of some of the aforementioned combustion efficiency contributions, such as two-dimensional, chemical kinetics and throat boundary layer effects, possibly leading to an underestimation of the theoretically achievable characteristic velocity. A minimum in combustion efficiency is found for both hardware between O/F 2.6 and 3.0 where a velocity ratio equals to the unit is found. Indeed, the mixing between the central oxygen core and the surrounding methane flow, arising through the relative shear interaction of the streams, is strongly promoted by a gradient in fuel to oxidizer flow velocities. Hence, the velocity ratio is a key factor in determining the onset and the position of the shear layer where the reagents mix and interact.

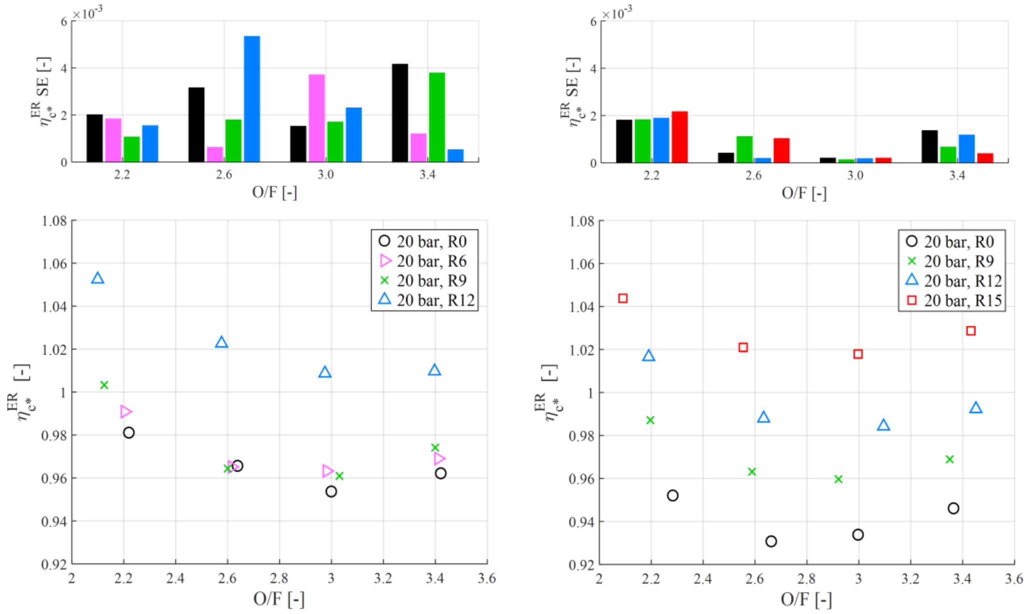

(a) Round combustion chamber **(b)** Rectangular combustion chamber

Fig. 41. Energy release combustion efficiency

In conclusion, when a recessed oxidizer tube is adopted an increase in the combustion efficiency is achieved, due to a better initial mixing in the recessed region, regardless of mixture ratio, each oxidizer-to-fuel ratio experiencing the same rise in combustion performance, approximately. A different behaviour is encountered for the two combustor geometries, though. While a substantial gain in combustion efficiency is visible in the circular arrangement only for a recess length of $3x\ d_i$, a gradual increment is obvious for the rectangular hardware, that being consistent with the previous statements.

An efficiency factor – K_η – was defined [23] to correlate the gain in combustion efficiency when an oxidizer post recess is introduced compared to the flush-mounted injector configuration, to the rise of the injector pressure drop due to the presence of a recessed region, as seen in *Fig. 20* and *Fig 21*. To this end, a relative combustion chamber pressure coefficient gain – *G* – was introduced, taking into account the change in mean combustion chamber pressure due to a recessed inner tube to the said increment in the injector pressure drop, for both oxygen and methane sides. The basic definitions of the aforementioned parameters are given in *Eq. 4.7*, *Eq. 4.8* and *Eq. 4.9*.

$$K_\eta = \frac{(\eta_{c^*})_{Recess} - (\eta_{c^*})_{R0}}{(\eta_{c^*})_{R0}} \tag{4.7}$$

$$G_O = \frac{(P_C)_{Recess} - (P_C)_{R0}}{\Delta P_{inj,GO_X}} \tag{4.8}$$

$$G_M = \frac{(P_C)_{Recess} - (P_C)_{R0}}{\Delta P_{inj,GCH_4}} \tag{4.9}$$

Thrust chamber efficiency factor over G_O and G_M is shown in *Fig. 42* and *Fig. 43*, respectively. Standard error of the mean is depicted for all the operating points and injector configurations. As one can infer from the given definitions, two regions are identified as concerns G parameter: the locus of the points for $G > 0$ is representative of run tests experiencing no losses in combustion chamber pressure compared to the *R0* injector assembly. The opposite for $G < 0$. Similarly, $K_\eta > 0$ detects an improvement in combustion efficiency compared to the reference case. The higher the efficiency factor, the larger the combustion efficiency gain. The higher the relative combustion chamber pressure coefficient gain, the lower the injector pressure drop. A substantial combustion efficiency improvement was only found for the 12 mm recess length in the round hardware, as already stated. In addition, one can notice as a highest combustion efficiency at mixture ratio 2.2 is achieved in the face of a more significant rise of the injector pressure drop than the other oxidizer-to-fuel ratios, for both oxygen and methane sides, even though an increment of the mean combustion pressure level than the reference case is still granted ($G > 0$). A more linear increment of the efficiency factor is achieved in the square geometry, as already seen for the combustion efficiency assessment. A maximum rise is experienced for the *R15* recess length, where a loss in the mean chamber pressure than the reference case is now noticeable ($G < 0$) for O/F 2.2. The same behaviour is reported to affect oxidizer and fuel lines. The higher mixture ratio analysed is found to produce the larger increase in mean combustion chamber pressure and minimum injector pressure drop, at once.

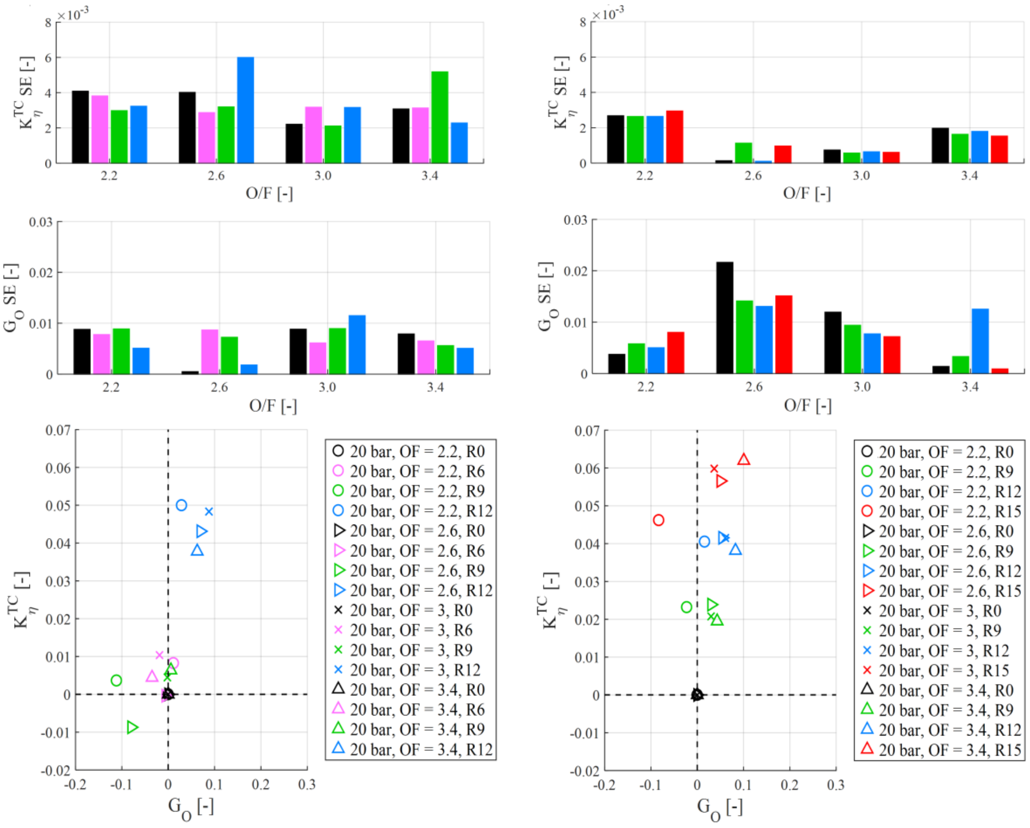

(a) Round combustion chamber **(b)** Rectangular combustion chamber

Fig. 42. Efficiency factor over G_O

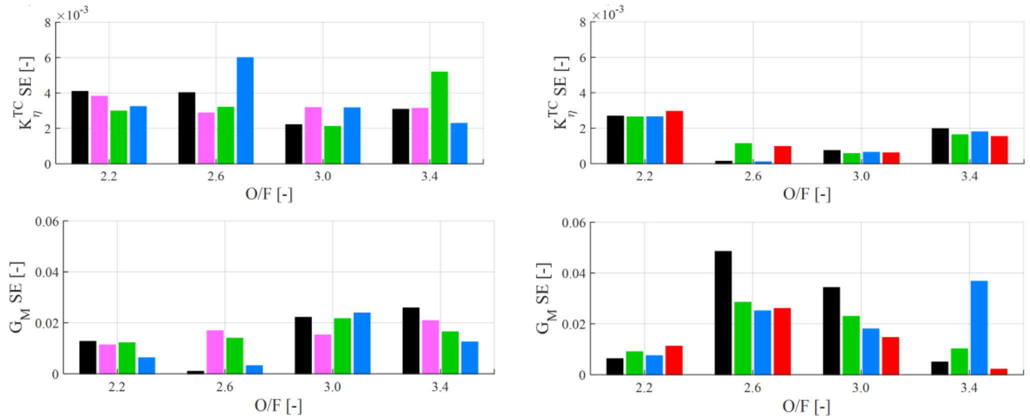

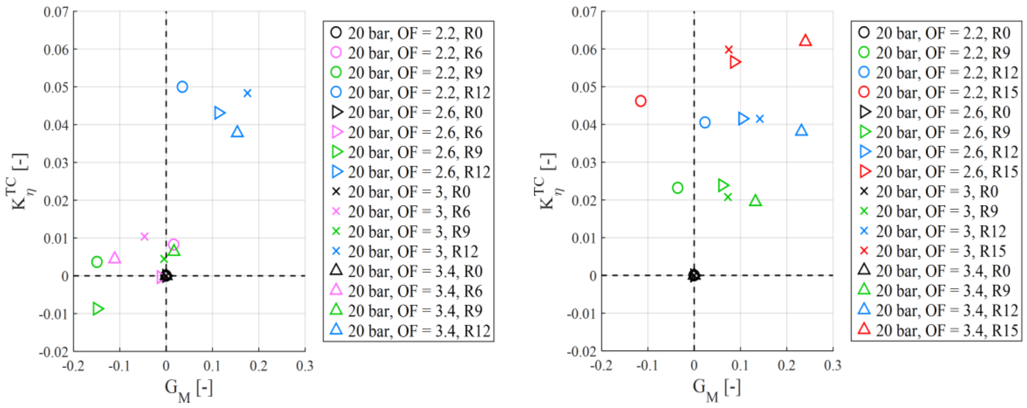

(a) Round combustion chamber **(b)** Rectangular combustion chamber

Fig. 43. Efficiency factor over G_M

4.5 Mean combustion chamber pressure influence

An overview of the mean combustion pressure effects on the main parameters describing combustion chamber operations and characteristics is investigated and discussed below. Round combustor run-in tests at nominal pressure levels of 10 bar and 20 bar are outlined and discussed.

A certain similarity is observed in the normalized pressure distribution along the combustion chamber axis for the two pressure values, 20 bar and 10 bar test results being depicted in *Fig. 44* and *Fig. 45*. Oxidizer-to-fuel ratio equals to 2.2 and 3.4, respectively. The same stagnation point over the combustion chamber length is experienced for the lower as well as for the higher mixture ratios analysed, as well as the recess length is found not to affect the stagnation point location for the two combustion chamber pressure levels. While the pressure drop in the near-injection region is only lightly affected by the mean chamber pressure for the *R6* and *R9* injector configurations, a stronger recirculation zone can be inferred for the 12 mm recess length, where a larger pressure drop is encountered for the 20 bar pressure case. Indeed, it is recalled as a non-equilibrium combustion process is established close to the injection plane, thus the reaction rate of individual species being pressure dependent in a non-linear manner. A compensation between the fluid dynamics and chemical kinetic processes may induce a non-linear behaviour in the near-injector area where low temperature levels, steep velocities and concentration gradients are predominant [44]. The pressure decay along the combustion chamber axis is not significantly affected by the variation of the mean combustion chamber pressure even if a more convex trend shape is reported to arise for the 20 bar condition. A steeper flattening of the wall pressure close to the nozzle is also promoted in this case. The higher the oxidizer-to-fuel ratio the lower the wall pressure drop in the near-injector region, as already pointed out. No substantial pressure drop is found for the oxidizer-to-fuel ratio 3.4 and P_C = 10 bar for the *R6* and *R9* recessed injector configurations. An influence of the 12 mm recess length configuration is detected, instead. A bumping wall pressure profile tendency can be inferred for the non-recessed injector configuration and 10 bar combustion chamber pressure. This behaviour can be appreciated for both oxidizer-to-fuel ratios 2.2 and 3.4 even if a higher standard error of the mean is herein calculated. Nevertheless, a good agreement between the samples is obtained by means of the repeatability analysis on the repetition test values. To summarize, higher combustion chamber pressure values are reported to induce sharper wall pressure gradients along the combustion chamber axis length. This can be related to a clear indication of an overall improvement and fastening of the mixing between the propellants, especially in the near injector region, and of the combustion efficiency.

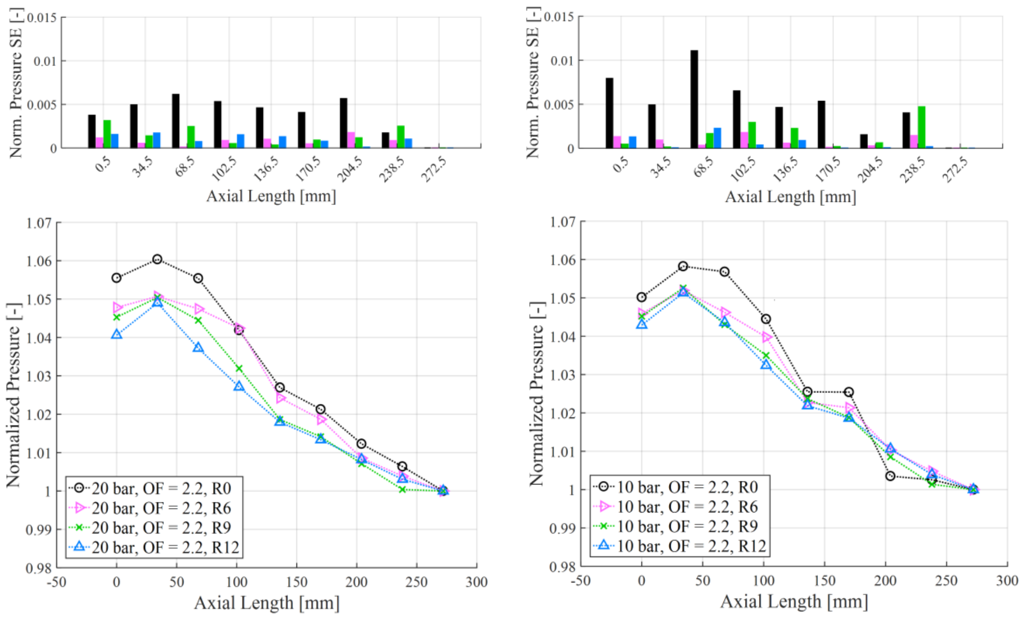

(a) P_C = 20 bar **(b)** P_C = 10 bar

Fig. 44. Round combustion chamber normalized pressure distribution along axis – O/F = 2.2

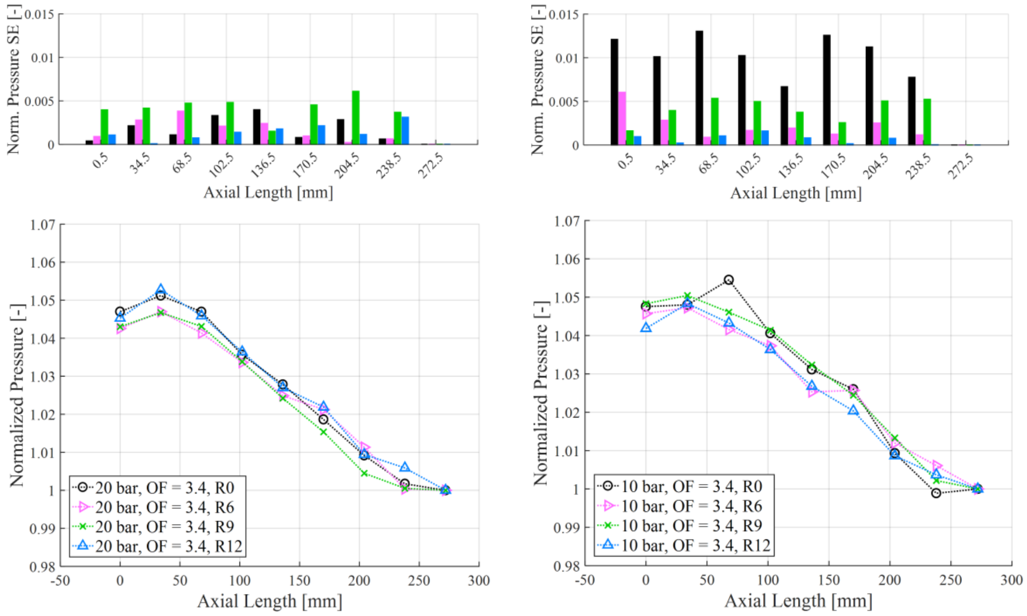

(a) P_C = 20 bar **(b)** P_C = 10 bar

Fig. 45. Round combustion chamber normalized pressure distribution along axis – O/F = 3.4

Oxygen and methane side injector pressure drop coefficients, defined in *Eq. 4.3* and *Eq. 4.4*, are depicted in *Fig. 46* and *Fig 47*, respectively, P_C = 20 bar on the left, P_C = 10 bar on the right. A lower influence of a recessed oxidizer post when compared with the reference injector configuration can be inferred for the 10 bar tests. A certain recess length is still required for the flow to interact inside the recessed region and a mild variation of the pressure drop coefficients due to the mixture ratio is reported to occur, for the 20 bar as well as the 10 bar operating conditions for the *R6* and *R9* recess lengths. In addition, a certain saturation on mixture ratio variation is encountered for the 12 mm recess and 10 bar chamber pressure as concerns the methane side pressure loss. Smaller pressure drops across the injector orifices are found for the lower pressure level other than the higher one, same injector configuration being considered. This may be addressed to the slower expansion rate of the flame inside the injector recessed region in the former case, thus resulting in a less significant blocking of the propellants and lowering the pressure loss across the orifices, if compared to higher combustion pressures. A bigger disparity between the two pressure levels is experienced for the methane side, where the less dense methane may benefit from the reduction of the spreading capability of the flame inside the recessed area. Nevertheless, an increase of the pressure drop due to the presence of a

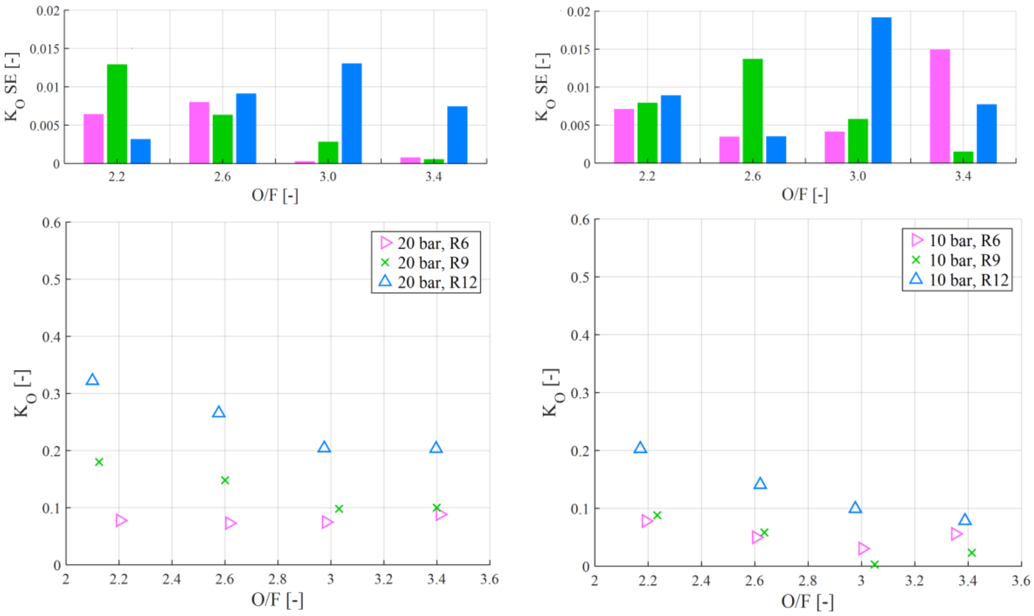

(a) P_C = 20 bar **(b)** P_C = 10 bar

Fig. 46. Round combustion chamber oxygen injector pressure drop coefficient

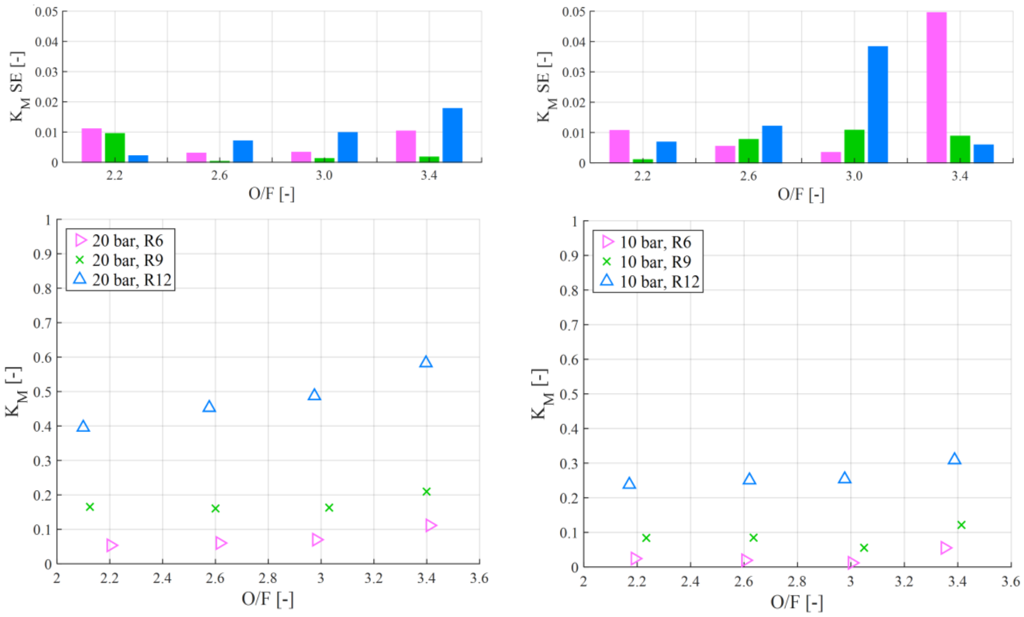

(a) P_C = 20 bar **(b)** P_C = 10 bar

Fig. 47. Round combustion chamber methane injector pressure drop coefficient

recessed oxidizer tube can be generally inferred for the lower combustion chamber pressure level, too.

Temperature difference profile between the evaluation time and an initial time of 1/6 of the hot run after the ignition (~ *0.5s*) is evaluated and shown in *Fig. 48*, for mixture ratio 3.4, combustion chamber pressure equals to 20 bar on the left, 10 bar on the right. An increase of the temperature readings along the combustor axis is expected for the higher combustion pressure level, a maximum difference being predicted at the end of the combustion chamber. While the mean combustion chamber pressure slightly affects the temperature difference reading at the first measurement point after the injector plane ($z = 0.5\ mm$), a different behaviour is detected in the near-injector region where a larger gradient increasing recess length is found for the higher combustor pressure value. A limited peak in the temperature distribution at $P_C = 10$ bar arises for the *R12* injector assembly right after injection, no influence on the temperature profile is reported for the *6 mm* recess length while an increment in the aforementioned trend is only noticeable in the second segment of the hardware for the *9 mm* recess. To sum up, an increase of the mean combustion pressure level is reported to straighten the effect on the temperature distribution rise due to a recessed oxidizer post. A negligible influence of the oxidizer-to-fuel ratio modification on the temperature trend is observed on the reference as well as on the lowest recess lengths (*R6* and *R9* configurations) for the 10 bar tests, differently than the 20 bar condition. Only the 12 mm post recess length is reported to be slightly affected in the second

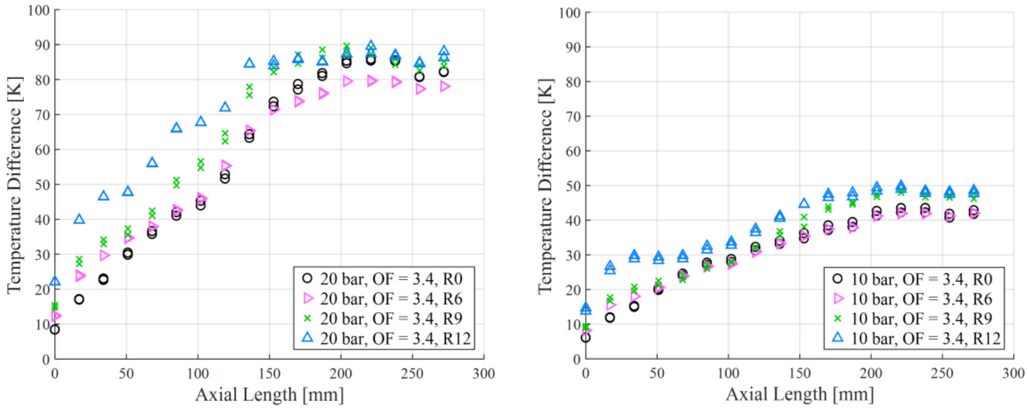

(a) $P_C = 20$ bar **(b)** $P_C = 10$ bar

Fig. 48. Round combustion chamber temperature difference distribution along axis at evaluation time – Recess comparison

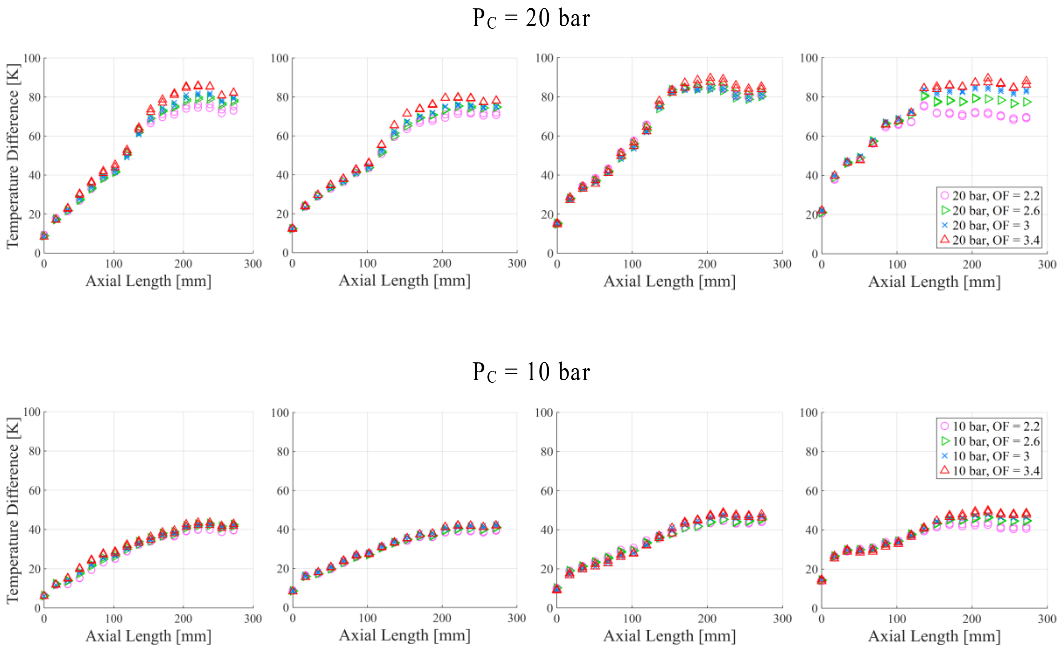

(a) *R0* **(b)** *R6* **(c)** *R9* **(d)** *R12*

Fig. 49. Round combustion chamber temperature difference distribution along axis at evaluation time – O/F comparison

segment of the combustion chamber for P_C = 10 bar. Nevertheless, a faster, not strongly significant, combustion end is noticeable increasing the recess length also for the lower pressure level, a more rapid flattening of the temperature distribution being promoted.

Temperature trends over time at a chamber pressure of 10 bar confirm the influence of a recessed oxidizer inner tube on the combustion process. Indeed, a similar temperature profile over burning time is found for the two pressure values, as can be seen for the first four thermocouples from the injection plane in *Fig. 50*, top to bottom mean chamber pressure rising. An increment of the temperature slope is found increasing the recess length, due to a better initial mixing of the propellants. The impact of the flame to the wall is reported to possibly enhance flame intensity and wall temperature spreading. This could explain the maximum rise of the temperature gradient experienced by the thermocouples at *z = 17.5 mm* from the face-plate [23] for both the chamber pressures outlined. A saturation of the influence induced on the temperature readings by the recess length can be found proceeding along the hardware axial coordinate (e.g. *z = 51.5 mm*), especially at lower pressure levels. This is more

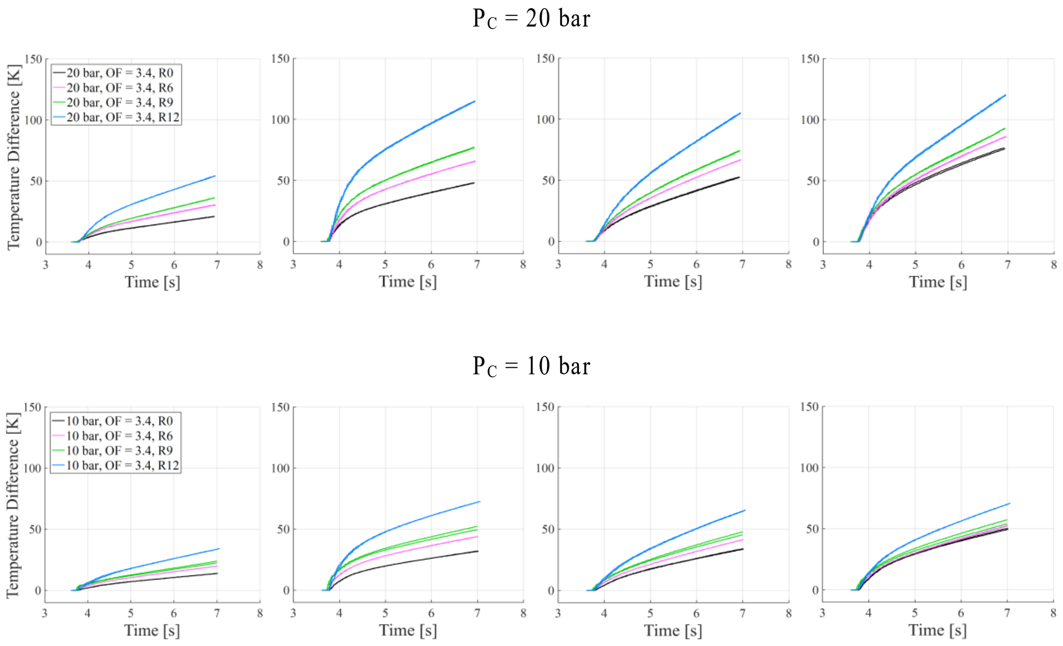

(a) z = 0.5 mm **(b)** z = 17.5 mm **(c)** z = 34.5 mm **(d)** z = 51.5 mm

Fig. 50. Round combustion chamber temperature difference distribution over burning time O/F = 3.4

clear for the *R6* and *R9* injector configurations, the 12 mm recess case still noticeably being affected compared to the reference case.

Wall heat flux for mixture ratios 2.2 and 3.4 is depicted in *Fig. 51* and *Fig. 52*, respectively, P_C = 20 bar on the left, P_C = 10 bar on the right. A correlation taking into account for heat flux dependency on mean combustion chamber pressure is adopted, as in *Eq. 3.1*. A rise of the wall heat flux in the near-injection region increasing the recess length is visible for the 10 bar pressure value, as already pointed out for the higher pressure level, as well as a flattening of the said trend is reported to exhibit further upstream for the *R12* configuration other than the lower recess lengths. A slightly lower influence due to mixture ratio variations is inferred for the 10 bar tests, even if the influence of the combustion process on heat loads in the second part of the hardware rather than the initial mixing of the propellants in the near-injector zone is affecting the heat flux distribution for both the 10 bar and the 20 bar chamber pressure investigations. Since the heat transfer coefficient is reported to scale to the mean chamber pressure to the power 0.8, a normalization of the heat flux to the actual combustion pressure level to the said power is taken into account, as suggested in

Heat flux ref. SE $[W/m^2]$

$(SE_{max})_{R0} = 2.0e{+}04$ $(SE_{max})_{R6} = 3.3e{+}04$ $(SE_{max})_{R0} = 3.1e{+}04$ $(SE_{max})_{R6} = 1.6e{+}04$

$(SE_{max})_{R9} = 4.5e{+}04$ $(SE_{max})_{R12} = 1.3e{+}04$ $(SE_{max})_{R9} = 2.1e{+}04$ $(SE_{max})_{R12} = 2.2e{+}04$

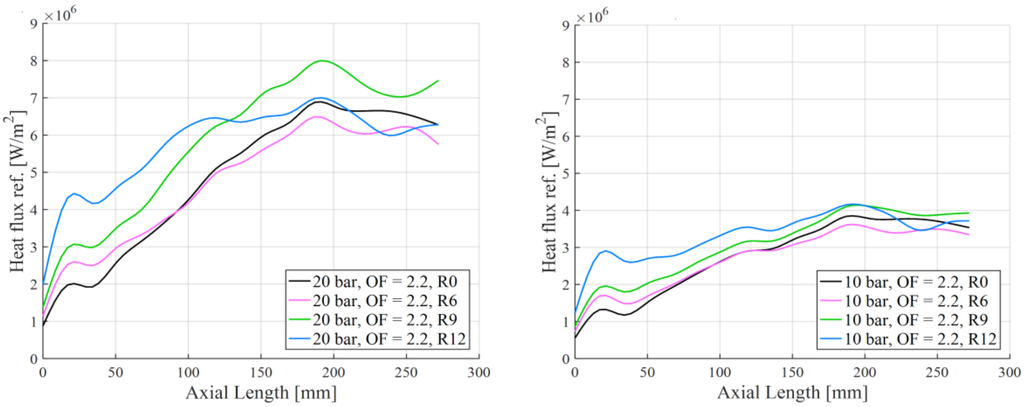

(a) P_C = 20 bar **(b)** P_C = 10 bar

Fig. 51. Round combustion chamber heat flux distribution along combustion chamber axis O/F = 2.2

$(SE_{max})_{R0} = 4.5e{+}04$ $(SE_{max})_{R6} = 2.9e{+}04$ $(SE_{max})_{R0} = 3.0e{+}04$ $(SE_{max})_{R6} = 1.7e{+}04$

$(SE_{max})_{R9} = 4.0e{+}04$ $(SE_{max})_{R12} = 5.1e{+}04$ $(SE_{max})_{R9} = 4.3e{+}04$ $(SE_{max})_{R12} = 9.6e{+}03$

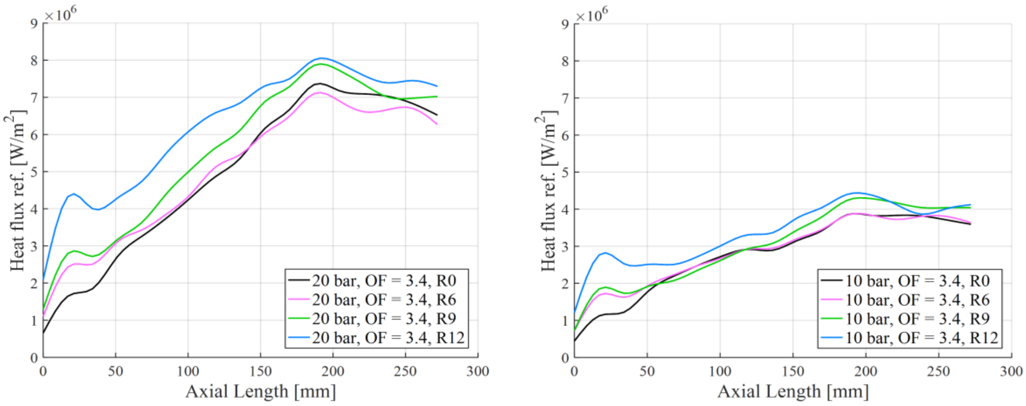

(a) P_C = 20 bar **(b)** P_C = 10 bar

Fig. 52. Round combustion chamber heat flux distribution along combustion chamber axis O/F = 3.4

Celano et al. [45]. The normalized wall heat flux distribution for both chamber pressures tested and O/F = 3.4 is depicted in *Fig. 53*. A comparable behaviour has been found for all the other oxidizer-to-fuel ratios analyzed. A good agreement on data is clearly visible, all normalized profiles collapsing to the same order of magnitude, same recess length being considered. A good scaling of the wall heat flux to the mean combustion chamber pressure for a gas-gas injector is thus confirmed.

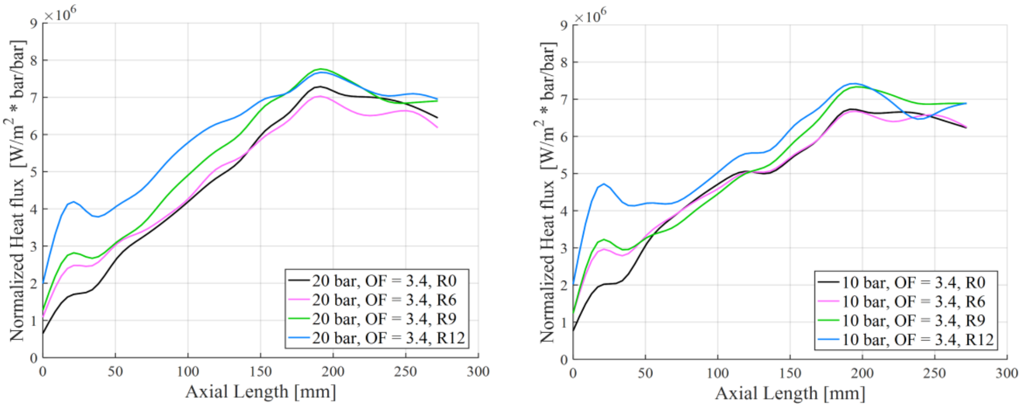

(a) P_C = 20 bar **(b)** P_C = 10 bar

Fig. 53. Round combustion chamber normalized heat flux distribution along combustion chamber axis – O/F = 3.4

Recess influence on combustion efficiency at different combustion chamber pressures is investigated, finally. Thrust chamber combustion efficiency, defined in *Eq. 3.2,* is calculated and outlined in *Fig. 54* for all the recess lengths and mixture ratios analysed, the 20 bar case on the left, the 10 bar case on the right. No significant different behaviour is encountered if an injector-based energy release approach is adopted. As expected, higher combustion efficiencies characterize the higher chamber pressure tests. This can be due both to a proportionality of the combustion energy to the combustion chamber pressure level and a non one-to-one scaling of the energy losses to the mean pressure of the system. An increase of the adiabatic wall efficiency for higher pressures is thus promoted [40]. As reported by Ueda et al. [46] on a LO_X/CH_4 investigation on rocket engines for upper stage systems at a pressure range between 10 and 30 bar, higher chamber pressures are found to decrease kinetic losses in the system, thus raising thrust performance, as well as a strong impact at lower pressure levels is exerted by the concentration of species. A reduction of the dissociation in smaller species was found increasing the mean combustion chamber pressure from 20 to 25 bar, so decreasing the possible loss in energy. A larger consumption of oxygen detected for increasing chamber pressures as well as the impact of lower energy molecules carrying energy may increase the combustion efficiency. A similar combustion efficiency behaviour is encountered increasing recess length for both pressure levels, even if the lower the pressure the higher the influence of the rising mixture ratio on combustion efficiency.

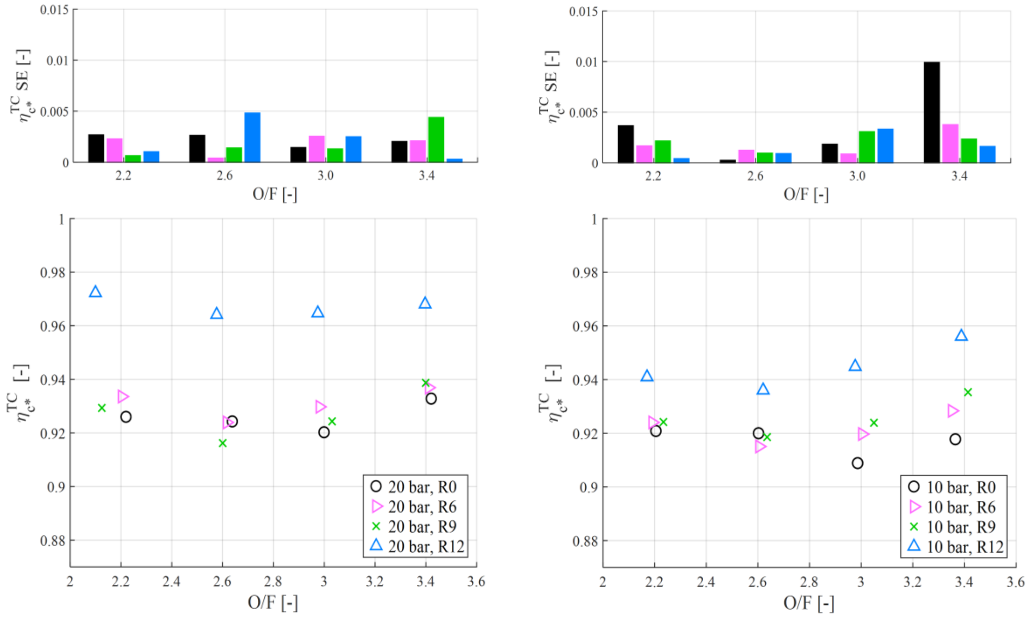

(a) $P_C = 20$ bar **(b)** $P_C = 10$ bar

Fig. 54. Round combustion chamber thrust chamber combustion efficiency

Indeed, an increase of combustion efficiency than the *R0* recess is visible for the *R6* and *R9* recess lengths for mixture ratios 3.0 and 3.4 at $P_C = 10$ bar, while no particular influence is found for the higher chamber pressure. A similar behaviour is noticeable for the 12 mm recess length. In fact, whereas a constant increment of about 4% is calculated at $P_C = 20$ bar for the *R12* injector assembly if compared to the reference case, the higher the mixture ratio the larger the combustion efficiency gain compared to the *R0* configuration at $P_C = 10$ bar. Indeed, in this case a 2 % increment than the reference case is found for O/F 2.2, an increase of 4% for O/F 3.4.

Ultimately, an increment of the mean combustion chamber pressure is reported to enhance combustion characteristics and performance, as well as heat flux and wall temperature increase as the chamber pressure is augmented. A higher effect due to mixture ratio modification is detected for the higher chamber pressure, especially in the second segment of the hardware. In addition, a larger influence of recess length variation is found to affect the combustion process for the higher pressure level, even though an improvement of mixing between the propellants is encountered for the lower chamber pressure too as the oxidizer post is recessed. On the other hand, an increment of the blocking of the flame inside the recessed region arises as the mean combustion pressure increases, due to the stronger spreading of the combustion products. Thus, higher injector pressure drops have to be expected for equal recess lengths.

Chapter 5

Optical diagnostic

An overview of the optical diagnostic analysis performed on the rectangular combustion chamber is given in the following. A qualitative investigation on the jet flame shape and dynamics in the near-injector region is performed by means of imaging techniques on hydroxyl (*OH*) radical emissions.

5.1 Near-injector flow field and flame dynamics

An averaging over 50 instantaneous *OH* radical emission images, each of them featuring an exposure time of 5000 μs, is carried out [36] and presented in *Fig. 55* for all the tested injector configurations and mixture ratios 2.2 and 3.4, on the left and on the right, respectively. An actual 40 x 12 mm^2 flat visual access area is granted by the optical access assembly. Flow direction from the left to the right. Cracks on the quartz glass window arose during experimental operations for the *R0* configuration tests, in the proximity of the end of the optical access, and for the *R12* configuration tests, in the near injection region. Soot deposition is visible for the *R9* and *R15* injector assembly run-in tests, instead.

A significant concentration of the reaction process is observed for the *R0* injector configuration in the second part of the optical access region, other than in the closest injector area. The cylindrical-like flame envelops the oxidizer jet in the first part of

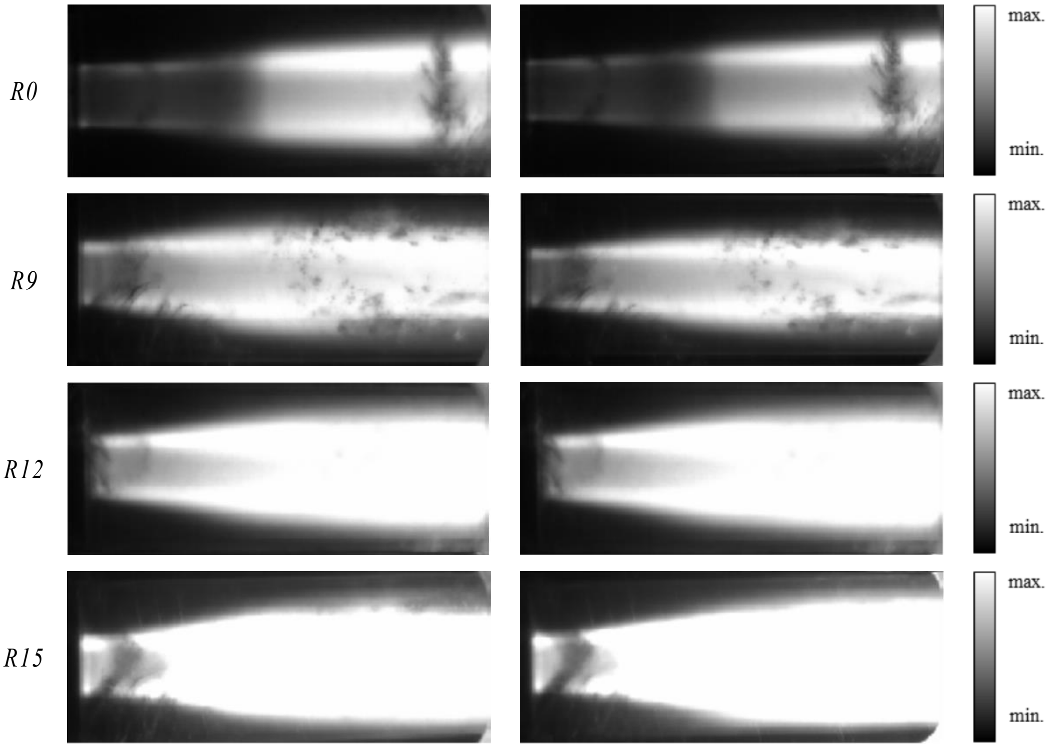

(a) O/F = 2.2 **(b)** O/F = 3.4

Fig. 55. Averaged hydroxyl (*OH*) radical emissions – Rectangular combustion chamber [36]

the visible access, gradually spreading and diverging from the combustion chamber axis to the combustor walls in the second part, where it assumes a cylindrical shape, again. A more intense flame is processed for the lower mixture ratio, where a higher momentum flux ratio is experienced, where a thicker flame shape is encountered. A thinner plume is visible increasing oxidizer-to-fuel ratio, the now predominant oxygen stream carrying the flame downstream along the combustor. A non- or low-emitting zone around the chamber axis is representative of the presence of the oxidizer jet where no combustion takes place. When an oxidizer post recess length is considered, the reaction region is moved upstream near the injector plate and the emitting volume is intensified. A conical shape is promoted right after injection, where a higher expansion rate and a thicker flame brush are noticeable. A higher spreading angle is observed if compared to the reference configuration, the jet appearing a quasi-cylindrical shell increasing distance from the injector plane. A similar behaviour was found in Lux et al. [21] for a LO_X/CH_4 combination and Kendrick et al. [18] in a LO_X/GH_2 investigation on shear coaxial injectors. The higher the recess length, the broader the volume occupied by the flame in the near injector region and the more intense the reaction zone, due to a better mixing inside the recessed area. The same behaviour is encountered for all the mixture ratios analysed. A maximum size of the emitting volume was approximately found [36] at about $4.9x\ d_i$ from the injector plane for all the injector configurations. A gradual reduction of the plume is visible. Additionally, a shortening of the central low-emitting oxidizer core length is visible increasing the recess length. This behaviour has been addressed [43] to the onset of two high turbulent viscosity regions near the face-plate position, the one between unburned CH_4 and the diffusion flame, the other between unburned O_2 and the diffusion flame. Larger turbulent viscosity regions are reported to arise strongly between the oxygen stream and the diffusion flame. Thus, the higher the oxidizer post recess length the more enhanced the turbulence in the region and therefore shorter O_2 cores appear.

Table 4. Averaged *OH* emission intensity over time and axial position [36]

		R0	***R9***	***R12***	***R15***
O/F	**2.2**	77.5	102.4	134.4	158.1
	3.4	69.0	97.1	139.5	161.5

An average light intensity over time and axial position has been calculated [36], providing a qualitative mean of comparison between the injector configurations analysed. In fact, it is worthwhile to remember that the camera was in saturation for the *R15* recess length. Results are shown in *Tab. 4*. A relative deviation on data of about ±2% has to be taken into account, the presence of the cracks and soot deposition on the quartz glass window possibly affecting the data processing. A rise of the light intensity is evaluated increasing the oxidizer post recess length for both the oxidizer-to-fuel ratios analysed. Indeed, an increase of about 50% is found for the *R15* injector configuration if compared to the reference case.

The variance of the flame contour is evaluated and shown in *Fig. 56*. From top to bottom the recess length increases, mixture ratio equals to 2.2 on the left, mixture ratio equals to 3.4 on the right. A sample of 50 images, each of them featuring an exposition time of $50\ \mu s$, is processed. Flow direction from the left to the right. A strong fluctuation of the emitting volume is observed in the second part of the optical access for the reference injector case, as already stated. A recessed oxidizer post is

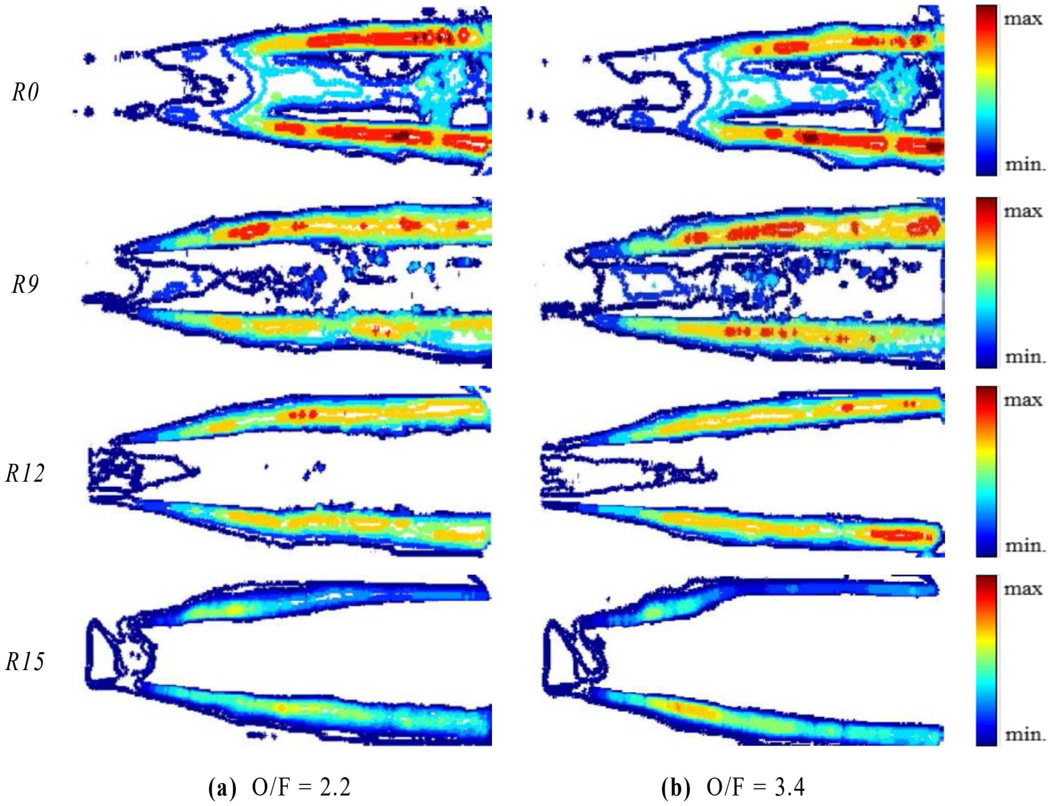

Fig. 56. Near-injector region flame variance – Rectangular combustion chamber [36]

reported to shift the reaction zone upstream to the injector plate. A thicker flame shape is noticeable for the lower mixture ratio analysed. In this case larger fluctuations arise on the external boundary layer, where the methane flow is faster than the oxygen core as can be seen in *Fig. 15.b*. On the contrary, a higher fluctuant behaviour is encountered in the shear layer between propellants for the higher oxidizer-to-fuel ratio [36].

Chapter 6

Conclusions

A rectangular inner cross section combustion chamber with optical access is set up and tested at a pressure level of 20 bar and mixture ratio from 2.2 to 3.4. A gaseous oxygen/gaseous methane fed single-element shear coaxial injector is used, allowing oxidizer post recess length variation. Recess lengths of 0 mm, 9 mm, 12 mm and 15 mm are tested, corresponding to 0x, 2.25x, 3x and 3.75x the internal oxygen tube inner diameter, respectively. The use of a recess length is reported to enhance the mixing of the propellants in the near-injection region, so shortening the combustion process and promoting the combustion effectiveness all over the combustion chamber length, even though higher injector pressure drops are encountered by increasing the recessed region due to the blockage of the developed flame in the pre-mixed recessed area. The higher the oxidizer inner tube recess, the larger the increment in temperature and heat loads to the wall. Mixture ratio variation is reported not to affect the combustion process in the first segment of the combustion chamber while a significant influence is found in the second segment; the larger the recessed area, the stronger the effect. A rise in combustion efficiency is calculated when a recess is introduced, the 15 mm recess length injector assembly experiencing a maximum increase of about 5-6%, depending on oxidizer-to-fuel ratio, if compared to the flush-mounted injector configuration. An imaging technique analysis on hydroxyl (*OH*) radical emissions in the near-injector region revealed how a more intense flame and a broader spreading angle are promoted by a recessed GO_X post, due to the enhanced mixing of the propellants inside the pre-mixed recessed zone, thus shifting the reaction area upstream to the injector plate. No remarkable influence is encountered because of oxidizer-to-fuel variations in the near-field behaviour.

The influence of the combustion chamber inner cross section geometry on injection and combustion properties is also investigated. A comparison with a previous recess variation experimental study on a round shape combustion chamber featuring similar geometric parameters and operating conditions is carried out. The presence of the corners in the rectangular combustion chamber is found to influence the flame dynamics in the near-injector area, primarily. A different near-field recirculation zone is triggered, so influencing combustion performance in terms of pressure, temperature and heat loads to the wall distributions, mainly close to the injector plate. A similar improvement in the combustion process due to the presence of an oxidizer post recess length is encountered for both the rectangular and round combustion chambers, though.

Finally, the effect of the mean combustion chamber pressure level on combustion characteristics and recess length variation is investigated. Combustion run-in tests at 10 bar and 20 bar on the round hardware are taken into account. An overall improvement on combustion performance and efficiency is reported increasing the chamber pressure level, due to the reduction in kinetic losses. A slightly minor influence of GO_X post recess variation is found for the lower pressure value, even though an improvement in combustion process than the flush-mounted injector configuration is still experienced. A scaling of wall heat flux distribution to the mean combustion chamber pressure for a gas/gas injector is also confirmed.

Appendix A

Experimental setup overview

An overview of the experimental setup is given below. The mobile test bed, the combustion chambers, the injector assembly and recess spacing rings, the rectangular combustor optical access and the optical diagnostic setup are shown.

Fig. 57. Mobile Rocket Combustion Chamber Test Bench (*MoRaP*)

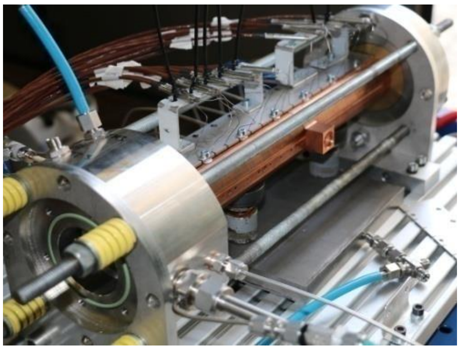

Fig. 58. Round combustion chamber assembly

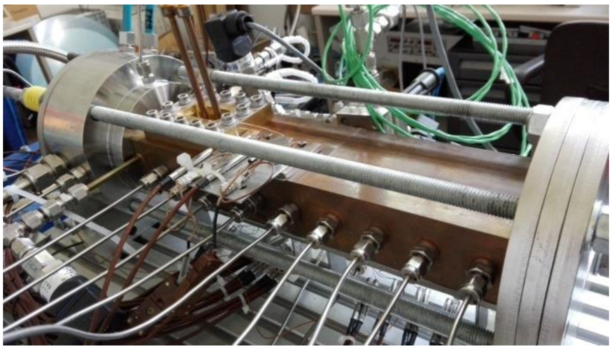

Fig. 59. Rectangular combustion chamber assembly

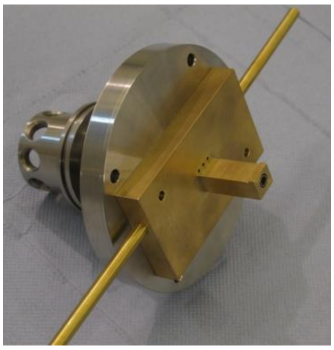

Fig. 60. Shear coaxial injector assembly

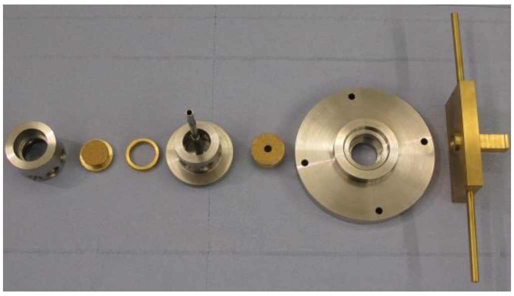

Fig. 61. Shear coaxial injector exploded assembly

Fig. 62. Injector head recess spacing rings (round combustion chamber)

Fig. 63. Injector head recess spacing rings (rectangular combustion chamber)

Fig. 64. Rectangular combustion chamber optical access

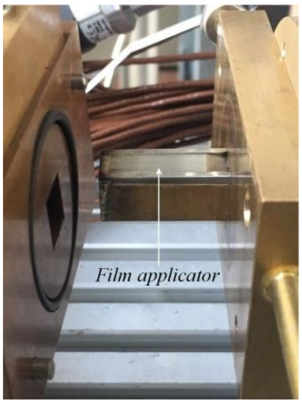

Fig. 65. Rectangular combustion chamber film applicator

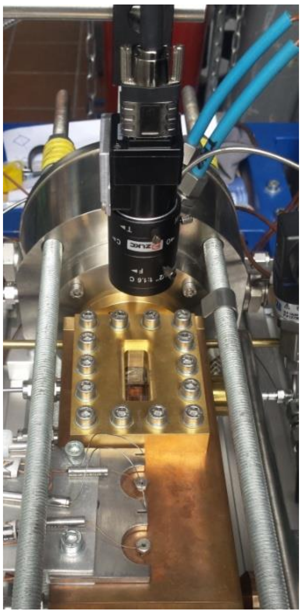

Fig. 66. Rectangular combustion chamber optical diagnostic setup

Appendix B

Uncertainty of measurement

A repeatability study between the experimental repetition tests has been conducted to analyze the goodness of the measurement acquisition procedures adopted. All experimental tests have been performed at least twice to ensure repeatability of the results, for both the rectangular and the round combustion chambers. Standard error of the mean, *SE*, is used as confidence interval between the repetition tests, thus giving an estimation of the random error of measurement in the form:

$$SE = \frac{S}{\sqrt{n}},$$

where *n* represents the number of test repetitions featuring same operative, hardware and environment conditions, and *S* the sample standard deviation, i.e. the estimator for the unknown population standard deviation. Bessel's correction have been adopted in the definition of the sample standard deviation, so referring to an unbiased estimator for the population standard deviation, as follows:

$$S = \sqrt{\frac{1}{n-1}\sum_{i=1}^{n}(x_i - \bar{x})^2},$$

where $\bar{x} = \frac{\sum_{i=1}^{n} x_i}{n}$ represents the arithmetic mean of the n observations (x_i) of the measured quantity. Following the dictates of the *International vocabulary of metrology* [47], the random measurement error estimation reported in this work is referred to repeatability conditions of measurement, that means that all the experimental results are obtained under '*condition of measurement, out of a set of conditions that includes the same measurement procedure, same operators, same measuring system, same operating conditions and same location, and replicate measurements on the same or similar objects over a short period of time*'. With reference to the measurement procedures in question, repeatability conditions of measurement were met under the following assumptions. Same operative conditions for the repetition tests were considered, i.e. measurement uncertainty is calculated for experimental tests featuring same nominal combustion chamber pressure, mixture ratio and overall burning time. Same hardware and measurement equipment setup were used, i.e. same recess length and combustor geometry is considered, as well as the same propellant/film coolant combination is taken into consideration. Identical measurement procedures were adopted from the same operator/s, too. Same environmental conditions were guaranteed. To this end, test repetitions were performed on the same time frame and in the same physical place, thus experiencing equal temperature and atmospheric pressure.

It is recalled that the confidence interval herein adopted only addresses to an estimation of the random measurement error affecting experimental procedures, i.e. to an estimate of the deviation of the measurand quantity from the mean of a finite number of the same measurand under repeatability conditions. The bias caused by the measuring instrument system, i.e. the systematic measurement error, is not included and assumed by definition as identically affecting results for a given experimental test campaign, where the same measurement equipment setup is used. To this end the bias evaluation takes into account the maximum value of the systematic error for the considered measurement system – *accuracy* – as well as all the possible sources of uncertainty of the measurement such as, amongst other, manufacturing, installation and calibration. A detailed study [48] on systematic measurement error uncertainties characterising the measured equipment setup described in the present work calculated an absolute bias affecting combustion chamber and manifolds pressure transducers less than 0.5 bar, that is less than 1% relative bias on measurements, for a 20 bar nominal chamber pressure. Similarly, the systematic error absolute uncertainty on thermocouples have been evaluated in less than 4 K, as well as less than 1% is the systematic error relative uncertainty on both operating (PC, O/F, $\dot{m}_{GOX}$, $\dot{m}_{GCH4}$) and performance (c^*, η_{c^*}, $C_{d,O}$, $C_{d,M}$) parameters.

References

[1] H. Burkhardt, M. Sippel, A. Herbertz and J.Kleanski, ‘Kerosene vs Methane: A Propellant Tradeoff for Reusable Liquid Booster Stages’, *Journal of Spacecraft and Rockets*, Vol. 41, No. 5, pp. 762-769, 2004.

[2] A. Götz, C. Mäding, L. Brummer, and D. Haeseler. ‘Application of Non-Toxic Propellants for Future Advanced Launcher Vehicles’, *AIAA Paper* No. 2001-3456, 2001.

[3] R.L. Ash, W.L. Dowler, G. Varsi, ‘Feasibility of Rocket Propellant Production on Mars’, *Acta Astronautica*, Volume 5, Issue 9, pp. 705-724, 1978

[4] K. Liang, B. Zang, Z. Zhang, ‘Investigation Of Heat Transfer And Coking Characteristics Of Hydrocarbon Fuel’, *Journal of Propulsion and Power*, Vol.14, No. 5, 1998.

[5] H.W. Valler, ‘Design, Fabrication and Delivery of a High Pressure LO_X – Methane Injector’, *Aerojet Liquid Company Report* 33205F, 1979.

[6] J.M. Locke, S. Pal, R.D. Woodward, ‘Chamber Wall Heat Flux Measurement for a LOX/CH_4Uni-element Rocket’, *AIAAPaper* No 2007-5547, 2007.

[7] A. Kootyev, L. Samoilov, ‘New Engines to Power Advanced Launch Vehicles’, 1998.

[8] J. Lux, D. Suslov, M. Bechle, M. Oschwald, O. Haidn, ‘Investigation of Sub- and Supercritical LOX/Methane Injection Using Optical Diagnostics’, *AIAA Paper* No 2006-5077, 2006.

[9] S. Zurbach, J.L. Thomas, P. Vuillermoz, L. Vingert, M. Habiballah, ‘Recent Advances on LOX/Methane Combustion for Liquid Rocket Engine Injector’, *AIAA Paper* No 2002-4321, 2002.

[10] R. Schuff, M. Maier, O. Sindiy, C. Ulrich, S, Fugger, ‘Integrated Modelling and Analysis for LOX/Methane Expander Cycle Engine: Focusing on Regenerative Cooling Jacket

Design', *AIAA Paper* No 2006-4534, 2006.

[11] D.K. Huzel, D.H. Huang, 'Modern Engineering for Design of Liquid-Propellant Rocket Engines. Progress in Astronautics and Aeronautics', *AIAA*, 1992

[12] A.H. Lefebvre, V.G. McDonell, 'Atomization and Sprays', *Hemispere*, 1989

[13] G.S. Gill, W.H. Nurick, 'Liquid Rocket Engine Injectors', *NASA*, SP-8089, 1976

[14] B. Chehroudi, D. Talley, and E. Coy, 'Visual Characteristics and Initial Growth Rate of Round Cryogenic Jets at Subcritical and Supercritical Pressures' *Physics of Fluids*, vol. 14, no. 2, pp. 850–861, 2002

[15] M. Oschwald, J. J. Smith, R. Branam, J. Hussong, A. Schik, B. Chehroudi, D. Talley, 'Injection of Fluids Into Supercritical Environments', *Combust. Sci. Tech.*, vol. 178, pp. 49-100, 2006

[16] J. Bellan, 'Supercritical (and Subcritical) Fluid Behaviour and Modelling: Drops, Streams, Shear and Mixing Layers, Jets and Sprays', *Progress in energy and combustion science*, 2000

[17] S. Candel, M. Juniper, G. Singla, P. Scouflaire, and C. Rolon, 'Structure and Dynamics of Cryogenic Flames at Supercritical Pressure', *Combustion Science and Technology*, vol. 178, no. 1, pp. 161-192, 2006

[18] D. Kendrick, G. Herding, P. Scouflaire, C. Rolon, S. Candel, 'Effects of a Recess on Cryogenic Flame Stabilization', *Combustion and Flame*, Vol. 118, No. 3, pp. 327-339, 1999

[19] A. Tripathi, M. Juniper, P. Scouaire, D. Durox, C. Rolon, S. Candel, 'LOX Tube Recess in Cryogenic Flames Investigated Using OH and H2O Emission', *AIAA Paper* No 1999-2490, 1999

[20] D. B. Wheeler, F.M. Kirby, 'High-Pressure LO_X/CH_4 Injector Program', *NASA CR-161342*, 1979

[21] J. Lux, O.J. Haidn, 'Effect of Recess in High-Pressure Liquid Oxygen/Methane Coaxial Injection and Combustion', *Journal of Propulsion and Power*, Vol. 25, No. 1, January-February 2009

[22] J.M. Locke, S. Pal, R.D. Woodward, 'Chamber Wall Heat Flux Measurements for a LOX/CH4 Uni-element Rocket', *AIAA Paper No* 2007-5547, 2007

[23] S. SIlvestri, M.P. Celano, G. Schlieben, O. Knab, O.J. Haidn, 'Experimental Investigation on Recess Variation of a Shear Coax Injector in a GOX-GCH4 Combustion Chamber', *Space Propulsion*, Rome, 2016

[24] S. Silvestri, M.P. Celano, G. Schlieben, O. Knab, O.J. Haidn, 'Investigation on Recess

Variation of a Shear Coax Injector for a Single Element GOX-GCH4 Combustion Chamber', *Trans. JSASS Aerospace Tech. Japan*, Bd. 14, pp. 13-20, 2016

[25] J P.Wanhainen, H.C.Parish, E.W. Conrad, 'Effect of Propellant Injection Velocity on Screech in 20,000-Pound Hydrogen-Oxygen Rocket Engine', *NASA* TN D-3373, 1966

[26] N.P. Hannum, L.M. Russell, D.W. Vincent, E.W. Conrad, 'Some Injector Element Detail Effects on Screech in Hydrogen-Oxygen Rockets', *NASA* TM X-2982, 1974

[27] V.R. Rubinsky, 'Combustion Instability in the RD-0110 Engine' *Liquid Rocket Engine Combustion Instability*, Vol. 169, Progress in Aeronautics and Astronautics, *AIAA*, Reston, VA, pp. 89-112, 1995

[28] C. Bauer, G. Schlieben, D. Eiringhaus, O.J. Haidn, 'Design and Commission of a Mobile GOX/GCH4 Rocket Combustion Test Bed for Education and Collegiate Research', *29th International Symposium Space Technology and Science*, 2013

[29] M.P. Celano, S. Silvestri, C. Kirchberg, G. Schlieben, D. Suslov, O.J. Haidn, 'Gaseous Film Cooling Investigation and Model Assessment in a Sub-scale Single Element GOX/GCH4 Combustion Chamber', , *30th International Symposium Space Technology and Science*, Japan, 2015

[30] D. Suslov, A. Woschnak, J. Sender, M. Oschwald, 'Test Specimen Design and Measurement Technique for Investigation of Heat Transfer Processes in Cooling Channels of Rocket Engines Under Real Thermal Conditions', *Joint Propulsion Conference & Exhibit*, *AIAA Paper* No 2003-4613, 2003

[31] F. Winter, S. Silvestri, M.P. Celano, O.J. Haidn, 'High Speed Imaging of a Coaxial Single Element GOX/GCH4 Rocket Combustion Chamber with Square Cross Section', *7th EUCASS Conference*, Milan, 2017

[32] S. Silvestri, M.P. Celano, G. Schlieben, C. Kirchberg, O.J. Haidn, 'Characterization of a GOX-GCH4 Single Element Combustion Chamber', *Space Propulsion*, Cologne, 2014

[33] M.P. Celano, S. Silvestri, J. Pauw, N. Perakis, F. Schily, D. Suslov, O.J. Haidn, 'Heat Flux Evaluation Methods for a Single Element Heat-Sink Chamber', *6th European Conference for Aerospace Sciences*, 2015

[34] N. Perakis, M.P. Celano, O.J. Haidn, 'Heat Flux and Temperature Evaluation in a Rectangular Multi-Element GOX/GCH4 Combustion Chamber', *7th EUCASS Conference*, Milan, 2017

[35] D. Bartz, 'A Simple Equation for Rapid Estimation of Rocket Nozzle Convective Heat Transfer Coefficients', *Journal of Jet Propulsion*, pp. 49-51, 1957

[36] S. Silvestri, F. Winter, M. Garulli, M.P. Celano, G. Schlieben, O.J. Haidn, O. Knab,

'Investigation on Recess Variation of a Shear Coaxial Injector in a GOX-GCH4 Rectangular Combustion Chamber with Optical Access', *7th EUCASS Conference*, Milan, 2017

[37] G. Sutton, W. Wagner, S.J. D. 'Advanced Cooling Techniques for Rocket Engines', *Astronautics and Aeronautics,* pp. 60-41, 1966

[38] S. Gordon, B. McBride, 'Computer Program for Calculation of Complex Chemical Equilibrium Compositions and Applications', *NASA Reference Publication 1311*, 1994

[39] C. Kirchberger, G. Schlieben, O.J. Haidn, 'Investigation on Film Cooling in a GOX/Kerosene Rocket Combustion Chamber', *29th International Symposium Space Technology and Science*, Japan, 2013

[40] S. Silvestri, M.P. Celano, O.J. Haidn, O. Knab, 'Comparison of Single Element Rocket Combustion Chambers with Round and Square Cross Sections' ,*6th EUCASS Conference*, Krakov, 2015

[41] H.Terashima, Y.Daimon, 'Generations of an Unstable Combustion Mode in a GCH4/GOX Coaxial Injector', *29th Computational Fluid Dynamics Symposium, E05-2*, 2015

[42] Johns Hopkins University, 'JANNAF Rocket Engine Performance Test Data Acquisition and Interpretation Manual', *NASA Technical Report CPIA-PUB-245*, 1975

[43] Y. Daimon, H. Terashima, H. Tani, 'Numerical Investigation for Recess Variation of a Shear Coax Injectorin a GCH4/GOX Combustion Chamber', *31th International Symposium Space Technology and Science*, Japan, 2017

[44] S. Silvestri, H. Riedmann, O. Knab, O.J. Haidn, 'Characterization of a Multi-Injector GOX-GCH4 Combustion Chamber', *Sonderforschungsbereich/Transregio 40 – Annual Report*, pp. 311-323, 2016

[45] M. P. Celano, S. Silvestri, G. Schlieben, C. Kirchberger, O. J. Haidn, S. Menon, 'Numerical and Experimental Investigation for a GOX/GCH4 Shear-Coaxial Injector Element', *Space Propulsion*, Cologne, 2014

[46] S. Ueda, T. Tomita, T. Onodera, Y. Kano, I. Kubota, T. Munenaga, 'Hot-Firing Test of Methane-Fueled Rocket Engine Under High Altitude Condition', *Joint Propulsion Conference & Exhibit*, *AIAA Paper* No 2002-4321, 2002

[47] Bureau International des Poids et Mesures, 'International Vocabulary of Metrology – Basic and General Concepts and Associated Terms', JCGM 200, pp. 23, 2012

[48] A. Cimino, 'Error Measurement Analysis & Performance Numerical Investigation on a Single Element GOX/GCH4 Combustion Chamber', 2016